University of São Paulo

Institut of Astronomy, Geophysics and Atmospheric Sciences

Department of Atmospheric Sciences

Thomas Christian Marcel Martin

Atmospheric variability in a complex terrain mesoscale basin and statistical regionalization in southeast Brazil.

Variabilidade atmosférica em uma bacia de mesoescala com terreno complexo e regionalização estatística no sudeste do Brasil.

São Paulo

2017

Thomas Christian Marcel Martin

Atmospheric variability in a complex terrain mesoscale basin and statistical regionalization in southeast Brazil.

Variabilidade atmosférica em uma bacia de mesoescala com terreno complexo e regionalização estatística no sudeste do Brasil.

Thesis submitted in partial fulfilment of the requirements for the degree of Doctor of Sciences in the Institute of Astronomy, Geophysics and Atmospheric Sciences.

Major field: Atmospheric Sciences
Advisor: Prof. Humberto Ribeiro da Rocha

São Paulo

2017

To my family.

Acknowledgements

various existing projects, going to field trip expeditions and last but not least, teaching me my first Portuguese words ("Eu *vai* almoçar").

Everything would have been much more difficult without my "mãe brasileira", Emilia. I am deeply grateful for her emotional support and for transmitting me her hunger to learn more everyday.

I also would like to thanks the IAG staff for their efficient technical support and friendliness, and especially Djalma, Samuel and Sebastião who demonstrated more than once that it is indeed possible to retrieve data from a hard-drive in fire.

A big thank you to Pr. Marcelo for sharing with me a glance of his impressive programming skills, following me in crazy ideas and showing me useful scientific tools. When we first met, I thought I knew how to code, I asked him if he knew Python and he answered "Python?, I know just a little.", for this he will remain my model of modesty.

I am grateful to all the professors at IAG, in particular to Dr. Ricardo Hallak, Dr. Carlos Mendonça, Dr. Pedro da Silva, Dr. Maria Assunçao and Dr. Edmilson Freitas for their insightful comments on this research.

This thesis was writen in LaTeX with the class IAGTESE, for IAG thesis and dissertation.

"La science n'a pas de patrie, parce que le savoir est le patrimoine de l'humanité, le flambeau qui éclaire le monde.

"Science knows no country, because knowledge belongs to humanity, and is the torch which illuminates the world. "

Louis Pasteur

Resumo

Em disciplinas como climatologia, hidrologia, ecologia, agricultura e estudos urbanos, são críticas as informações de alta acurácia e resolução espacial, em especial nas áreas de montanhas onde os fatores topográficos tem grande influência, como o clima de superfície do sudeste do Brasil, que é influenciado pelo oceano Atlântico e pelas cadeias de montanhas. Nós investigamos a variabilidade atmosférica de superfície e a formação de circulações secundárias desta região em meso-β com medidas em uma rede de estações meteorológicas e análise de Componentes Principais. Construímos um método de regionalização estatístico para estimar a informação climática em alta resolução também sobre uma região em meso-γ escala. Fizemos um experimento de campo em um vale entre montanhas de uma pequena bacia na Serra da Mantiqueira, para estudar a variabilidade atmosférica nas vertentes em escala horária e sazonal. Foi evidente o gradiente terrestre médio transversal ao vale, com um padrão de aquecimento/umidecimento diurno e resfriamento/secamento noturno, em relação ás vertentes. A temperatura as 12h mostrou grande variabilidade, que diminuiu com a altitude na taxa média -0.7 $^\circ C$ ($100m^{-1}$). A temperatura do ar noturna aumentou com a elevação até o máximo de 200m (cinturão térmico), em taxa sazonal maior (menor) na estação seca (chuvosa) de +1.1 $^\circ C$ ($100m^{-1}$) / +0.2 $^\circ C$ ($100m^{-1}$) em toda a vertente. A pressão de vapor diminuiu do vale para cima geralmente abaixo de -0.5 hPa ($100m^{-1}$), e o vento horizontal aumentou na taxa de 0.9 $m.s^{-1}$ ($100m^{-1}$). Notamos um aquecimento diferencial expressivo ao longo do vale e das vertentes. O médio vale esteve circunstancialmente mais frio á noite, e mais quente de dia, em relação ao alto vale, em magnitude média abaixo de 1.0 $^\circ C$. Os gradientes transversais ao vale mostraram-se bem associados á circulação local, com gradiente terrestre de temperatura positivo e vento catabático á noite, assim como o gradiente terrestre de temperatura

negativo e vento anabático, que coexistiram estritamente de dia. Os gradientes terrestres e as circulações secundárias foram de forma geral amortecidas por episódios de grande nebulosidade e/ou turbulência mecânica. Utilizamos as medidas de campo para construir um modelo de regionalização estatística baseado em ACP (PCA) e indíces topográficos, tendo por dependência as saídas de MCGs (GCMs), para prever o clima de superfície em alta resolução (30 m). Os modos das CP mostraram a variabilidade atmosférica diária e sazonal, os padrões diferenciais de aquecimento e umidecimento nas direções transversal e axial do vale, e a variabilidade do vento associada á topografia e ás circulações secundárias. Os escores das PCs e a saídas do GFS foram correlacionadas para se estimar a evolução temporal dos padrões espaciais, que mostraram razoáveis campos atmosféricos (MAE 1.1 $^{\circ}C$, 0.7 $g.kg^{-1}$ and 0.7 $m.s^{-1}$), que foram por sua vez superiores aos métodos simples de interpolação vertical do GFS. A ACP na escala regional mostrou que a variabilidade do vento na superfície foi controlada pela brisa marítima e pelo escoamento de grande escala, e de forma secundária pelas circulações de montanha. Durante o dia houve um efeito de advecção fria/úmida da brisa marítima para definir um gradiente climático com áreas quentes/secas no interior em relação á costa, em especial á tarde, ao passo que a umidade do ar aumentou nas áreas de montanha em relação ás planícies adjacentes. No início da noite o gradiente de temperatura litoral-interior inverteu-se progressivamente, ao passo que a brisa marítima inercial continuou progando-se para o interior. No litoral notou-se escoamento catabático em algumas estações. á noite, notou-se uma umidade maior no interior e nas planícies, comparado com o litoral e áreas de montanha. Com o disparo da brisa marítima, observou-se regionalmente os efeitos de mesoscala-γ em áreas de vales, com aquecimento (resfriamento) preferencial diurno (noturno), associado aos ventos anabático (catabático). As planícies e áreas no interior mostraram maior amplitude de temperatura e umidade (diurna e sazonal) que as áreas nas montanhas e no litoral.

Abstract

Accurate and high spatial resolution climate information is critical for several areas as climatology, hydrology, ecology, agriculture, urban studies, especially in mountainous region where large variability is promoted by topographical features, for example the southeast Brazil climate that is shaped by the influence of either the Atlantic ocean and mountain ranges. We investigated the surface atmospheric variability and the formation of thermally driven circulations in this region at the meso-β scale using ground station network measurements and Principal Component Analysis. We built a statistical downscaling methodology to estimate high resolution surface climate information in complex terrain at the meso-γ scale. We run a field experiment in a small basin with valley within slopes in the Serra da Mantiqueira to address the hourly, seasonal and hillslope atmospheric variability. The mean terrestrial gradients were evident in the cross-valley direction, where the valley tended to warm/wet up at day and cool/dry down at night, relatively to the slopes. The temperature at noon showed high variability and decreased at a mean rate of -0.7 $°C$ $(100m^{-1})$. The nocturnal air temperature increased with height up to a maximum at about 200m (the thermal belt), with seasonal rates higher/less in dry/wet season of +1.1 $°C$ $(100m^{-1})$ / +0.2 $°C$ $(100m^{-1})$ over the full altitude. The vapor pressure decreased from the valley upwards in general below -0.5 hPa $(100m^{-1})$, whereas the wind speed increased at a rate of 0.9 $m.s^{-1}$ $(100m^{-1})$. We noted a substantial differential warming along the valley and mountain sides. The middle valley was circumstantially colder at night and warmer at daytime, relatively to the upper catchment, under mean magnitudes below 1.0 $°C$. The cross-valley gradients appeared to be well associated with local circulation, where downwind and positive temperature gradients, as well as upwind and negative temperature gradients strictly coexisted during the morning. The terrestrial gradient and the secon-

dary circulation were in general dampened by cloudiness and/or mechanical turbulence. We used the field measurements to build a PCA based downscaling model and topographical indexes with the dependence on GCM outputs (GFS), to predict high resolution (30 m) surface climate in the basin. The PC modes appeared to show the daily and seasonal atmospheric variability, the differential patterns of warming and wetting on the cross-valley and along-valley directions, and the wind variability associated to the topography and the secondary circulations. The PC scores and GFS outputs were correlated to estimate the temporal evolution of the spatial patterns, that provided satisfactory atmospheric fields (MAE 1.1 °C, 0.7 $g.kg^{-1}$ and 0.7 $m.s^{-1}$), that improved over simple methods as vertically interpolation GFS. Our PCA analysis at the regional scale showed that the wind variability was either controlled by the sea-land breeze and large scale flows, and secondly by the mountain winds. At daytime the cool/moist sea breeze advected air engendered climatic gradient with warmer/dryer areas inland relatively to the coast, emphatically in the afternoon, whereas the humidity increased in mountain areas relatively to the adjacent plains. In the evening the coast-inland temperature gradient progressively reversed while the sea breeze continued to propagate inland in the overall domain. At the shore line downslope flows occurred at some stations. At night, higher humidity was observed inland and in the plains compared to the shore and mountains respectively. Along with the triggering of sea breeze, regionally we noted mesoscale-γ effects in places of valleys, with preferential morning (evening) warming (cooling), associated with upslope (downslope) flows. The plains and inland areas showed greater temperature and humidity amplitude (daily and seasonal) than areas in the mountains and near the coast.

List of Figures

List of Tables

List of Abbreviations

AGL	–	Above Ground Level
CPTEC	–	*Centro de Previsão do Tempo e Estudos Climáticos*
CSF	–	Clear Sky Factor
DEM	–	Digital Elevation Model
EOF	–	Empirical Orthogonal Function
GCM	–	Global Climate Model
GFS	–	Global Forecasting System
GRASS	–	Geographic Resources Analysis Support System
IAC	–	Instituto Agronomico de Campinas
IAG	–	Institut of Astronomy, Geophysics and Atmospheric Sciences
INMET	–	Instituto Nacional de Meteorologia
INPE	–	Instituto Nacional de Pesquisas Espaciais
LCB	–	Climate and Biosphere Laboratory
LNCC	–	Laboratório Nacional de Computação Científica
LST	–	Land Skin Temperature
MAE	–	Mean Absolute Error
meso-γ	–	2-20 km scale
meso-β	–	20-200 km scale
NCEP	–	National Centers for Environmental Prediction
REDMET-METAR	–	Rede de Meteorologia do Comando Aeronautica
RMSE	–	Root Mean Square Error
RMSP	–	Metropolitan Region of Sao Paulo city
PCA	–	Principal Component Analysis
PC	–	Principal Component
PCT	–	Principal Component of Temperature

PCQ	–	Principal Component of Specific Humidity
PCU	–	Principal Component of Zonal Wind
PCV	–	Principal Component of Meridional Wind
PCUV	–	Principal Component of Wind
PCTUV	–	Combined Principal Component of Temperature and Wind Components
PCQUV	–	Combined Principal Component of Specific Humidity and Wind
PRISM	–	Parameter elevation Regression on Independent Slopes Model
USP	–	University of São Paulo
UTC	–	Coordinated Universal Time
TLR	–	Terrestrial Lapse Rate
TOPEX	–	TOPographical Exposition Index
TWD	–	Terrestrial Wind Divergence

List of Symbols

$\mathbf{L}$ –   Principal component loadings

$\mathbf{P}$ –   Principal component scores

K –   Principal component rank number

Δ_{vs} –   Difference valley/slope

Δ_{mu} –   Difference middle/upper

Δ_{we} –   Difference West/East

Δ_x –   Meridional difference

Δ_y –   Zonal difference

LH –   Latent heat flux

H –   Sensible heat flux

Gr –   Ground heat flux

L –   Upward/downward longwave radiation

p –   Percentile

Rh –   Relative humidity

R^2 –   Correlation score

S –   Shortwave radiation

Q_{soil} –   Soil humidity

T_{soil} –   Soil temperature

T –   Temperature

$u\ (U)$ –   Zonal wind

$v\ (V)$ –   Meridional wind

$q\ (Q)$ –   Specific humidity

Contents

Chapter 1

Introduction

An accurate description of the surface climate is critical for ecological, agricultural, urban, environmental and hydrological studies, as it is a key factor of several physical processes at the earth surface. However, it is a challenging task as the heterogeneous distribution of the energy balance components caused by irregularities in the surface properties engender large climatic variations at a broad spectrum of temporal and spatial scale. Such variations are exacerbated in region of complex terrain where topographical factors (e.g. elevation, aspect, and sheltering) induce significant climatic gradients and wind systems over the sloping surfaces, both depending on net radiation and synoptic conditions (Whitemann, 1990; Dobrowski et al., 2009; Pepin et al., 1999). It is also the case for coastal regions, were the formation of sea land breeze is associated with the advection of cool moist air.

Mountains are headwaters to reservoir systems designed for hydropower and sanitation in southeast Brazil, so they are key places for water supply to the highly populated areas near Sao Paulo city where the dependence of surface water largely dominates. Despite Brazil is cited as owning about 18% of global fresh water, most of that is in Amazonia, and the southeast region dealt with two water shortages in last 15 years from unprecedent climatic records over last century (Coelho et al., 2016) that greatly affected the society (Coutinho et al., 2015; Nobre et al., 2016). It is expected that more accurate numerical weather forecast and water management in these regions can help the decision making during extreme climatic events. The ability of hydrologic models to calculate water exchanges that depend on temperature, wind speed and humidity in montane areas is critical to the spatial resolution (Dussaillant et al., 2012; Krogh et al., 2015), that should benefit from developing methods using weather station networks in complex terrain (Lookingbill and

Urban, 2003; Lundquist and Cayan, 2007).

Montane climates can be defined with near ground characterization of air temperature, humidity and wind speed, shaped by great spatial variability that depend largely on the net radiation and synoptic weather, but much also on local surface factors as topographic features of terrain, namely the elevation, areal dimension, convexity, aspect, sheltering, vegetation cover and soil moisture (Whiteman, 1990). Local terrestrial gradient (or lapse rate) of temperature, differently of environment atmospheric lapse rate, is highly distinct mostly under clear and calm weather, and has direct relationship with the surface energy balance, and the magnitude decreasing with mixing from large scale flow (Mahrt, 2006; LeMone et al., 2003). Thermally driven winds form in montane areas forced by buoyancy effects of differential heating and cooling day round in the boundary layer (Zardi and Whiteman, 2013). The formation of nocturnal cold air pools in terrain depressions, along with positive altitudinal temperature gradients, is observed even at farm scale in gentle slopes (Bodine et al., 2009; Dixit and Chen, 2011). Windy conditions tend to dampen the terrestrial gradients, and even the thermal circulations pose negative feedback to that (Mahrt, 2006). It appears that the complex organization of large scale flow and local factors for a place as a basin with valley between slopes helps to promote mountain winds which affect turbulent mixing and heat distribution and that ultimately define the local terrestrial temperature gradients. The role of local and synoptic drivers on these patterns must rely upon adequately (extensive and accurate) field measurements, that have long been discussed for places in middle latitudes of the northern hemisphere (Zardi and Whiteman, 2013; Blandford et al., 2008; Pepin et al., 1999), and adressed the issues of temporal variability and distinct spatial scales (Rolland, 2003; Minder et al., 2010; Lookingbill and Urban, 2003; Tang and Fang, 2006).

Surface climate data originate either from ground station measurements or Global circulation Models (GCM) outputs, or atmospheric reanalysis data that combine numerical and observational data, with particular advantages or limitations for each source, with respect to the climate variability and spatial scale. In situ punctual measurement potentially integrates all natural variability scales but may under-sample the spatial variability in critical circumstances as in complex terrain or urban places (Di Luzio et al., 2008), and

also because continous and accurate measurements are operationally and financially costly, especially in large networks. Long term continuous climatic datasets with global coverage are obtained from GCMs, that despite their skill to represent the macro-scale features, does not permit to represent the fine scale spatial variability. The combined advantages of these data sources can be tackled with statistical downscaling methods (Murphy, 1999), fitted with relationships between GCM outputs and surface observations. Spatially distributed predictions can be achieved using the variability among stations and spatial predictors (e.g. topographical indexes). Such methods are computationally efficient, easy to implement, that may however suffer to represent highly chaotic and complex systems, along with the assumption that the statistical relationships remain valid with time (Murphy, 1999). Statistical and empirical based methods were reported to downscale air temperature, humidity and wind speed (Murphy, 1999). For example De Rooy and Kees (2004) used the surface roughness to explain the heterogeneity of near surface wind speed. Gridded climatic outputs using statistical model have been produced for specific regions, for example long term high resolution (>1km) mean daily temperature for the countiguous U.S. are made available by PRISM (Daly et al., 1997), Daymet (Thornton et al., 1997), Wtopox (Oyler et al., 2014), that interpolate surface observations taking into account the vertical relative position to the nocturnal inversion. We believe that this methodology requires a relative dense network that currently does not exist in Brazil. Likewise, the statistical downscaling in complex terrain lack sufficient observations to capture the overall spatial variability, as weather stations are preferentially installed in areas near the valleys than on higher elevations, partly to help the operationality. Another challenge for these methods is to find site-specific appropriate topographic predictors that help to explain the spatial climatic variability. These predictors are generally extracted from Digital Elevation Model (DEM), where the most common one is the altitude, that works well for local scale with gentle slope variability. For larger area in mountain ranges, more complex predictors are required to represent the complex climatic pattern observed. Recently, Principal Component Analysis (PCA) was used to investigate the spatial distribution of nighttime temperature on complex terrain (Lundquist and Cayan, 2007; Holden et al., 2011; (Holden et al., 2011)) and develop a downscaling methodology with long term weather station data and complex topographic features (Holden et al., 2011). Model complexity is also time-dependent, for example the temperature terrestrial lapse rate shows linear dependence of altitude in uns-

table conditions, but non-linear at night due to the formation of cold air pools. Most of previous application using statistical modelling concerned either on a single atmospheric variable (e.g. temperature), or at a single point (station position) or at specific time of the day (e.g. nighttime) or average.

Previous studies in the southeast region showed the evidence of three main factors: the sea-breeze, the mountain-valley circulations and urban effects (roughness and heat-island), which were prominently observed during calm background conditions (Silva Dias and Machado, 1997; Oliveira et al., 2002; Perez and Dias, 2017). Sea breeze is associated with decreasing temperature and increasing dew point temperature (Oliveira and Dias, 1978), and to help the development of deep convection in the wet season and the dispersion of pollutant in the dry season (Freitas et al., 2007; Freitas et al., 2009; Vemado and Pereira, 2016). The daily wind cycle usually shows a counter clockwise rotation associated with a veering of the wind from NE in the morning to SE in the afternoon, when reinforced with the sea-breeze. The sea breeze front was noted over the city of Sao Paulo by around 13 and 14 LT in 60% of the case (Oliveira and Dias, 1978), that reaches further inland sectors usually at nighttime up to about 300 km. Silva Dias and Machado (1997) showed the modelled regional circulation point that indicated the formation of slope flow over the Serra Da Mantiqueira and Serra Do Mar, and the plain to mountain circulation between the Valley do Paraiba and Serra Da Mantiqueira, that initiated between 10 to 14UTC and reversed between 16 and 20UTC (Campos et al., 2016).

1.1   Objectives

This works aimed to report the surface atmospheric variability in complex terrain areas both at the meso-γ and meso-β scales near the coastal and mountainous region of southeast Brazil, and to build regionalization models using PCA tools to predict high resolution fields of temperature, humidity and wind speed.

Specifically the main tasks were to:

- analyse weather station measurements at a dense network in a complex terrain meso-γ scale basin at the Serra da Mantiqueira mountain range.

- describe the temporal and hillslope surface climate variability, with emphasys in the differential heating and the formation of secondary circulation.

- intepret the PCA modes of variability at the meso-γ and β scales within the coastal/mountainous areas of southeast Brazil

- build regionalization models using PCA based tools and topographic indexes, to downscale GCM outputs and predict high resolution atmospheric surface variables

Chapter 2

Materials and Methods

2.1 Spatial domain
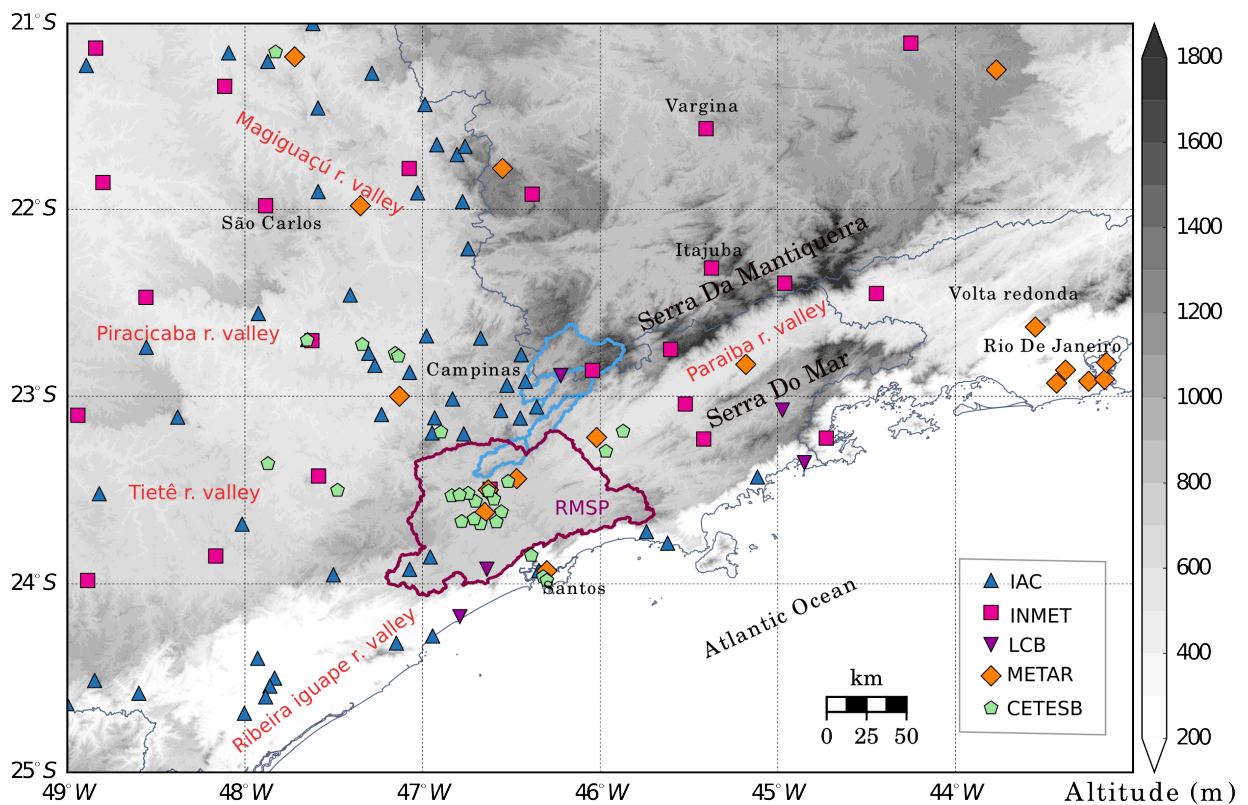
Figure 2.1: Altitudinal map of the studied domain with the position of the stations from the different institutions used in this analysis, with the states (light grey), Metropolitan Region of São Paulo (RMSP) (Purple) and Cantareira water system (ligh blue) limits as well as the name of important cities (small black letters), topographical features (large black letters) and river valleys (in red).

The area of investigation is the Southeast region of Brazil (21S to 25S, 49W to 43W) (Figs. 2.1 and 2.2.a.b), centered at the Metropolitan Region of Sao Paulo city (RMSP) at east of the Tietê river, with two major mountain ranges, the Serra da Mantiqueira and Serra do Mar, that are parallel to the coast line and separated by the Paraiba river valley,

with a northern sector characterized by a moderated hilly plateau, and the far western sector extending to the valleys of Piracicaba river and the Mogi river that both show gentle topography downstream their upper course. The relief of the mountain ranges is mostly composed by hills with convex ridges and drainage valleys (Ross, 1985), that in general shows gentle topography when compared to large mountains such as the Andes, Alpes or the Rocky mountains. This region is characterized by a subtropical climate of wet/warm summer and dry/mild winter.

A field experiment was settled at the Ribeirão das Posses watershed (22°52'37.2"S 46°14'47.3"W), Extrema/MG city (2.2), about 100 km distant from São Paulo/SP city, a 12 km2 area in the southwestern Serra da Mantiqueira. It is covered mostly by pasture (Brachiaria brizantha) (71,2%) and forest (24,8%) with eucaliptus and fragments of restored native and remnant native Atlantic forest trees (Saad, 2016), which is a typical landscape of the surrounding region. The basin is defined by an approximately 7km North-South oriented valley, with the altitude ranging between 950m in the valley to 1400 m at ridges in the upper catchment (Fig.2.2.c). The ridges are about 1.5 km wide at the middle basin to about 3km at the upper basin. In the upper basin the west side had a mean slope of 17% over an elevation gain of 300 m, and the east side of 23 % over a 350 m gain (Fig. 2.2.d); in the middle basin the west side slope was of 25% over a 75 m gain, and the east side of 14 % in 125 m gain.

2.2   Stations networks

2.2.1   Institutions

The sources of the ground observational data were the Instituto Nacional de Meteorologia (INMET), Companhia Ambiental do Estado de Sao Paulo (CETESB), Instituto Agronomico de Campinas (IAC), Rede de Meteorologia do Comando Aeronautica (REDMET-METAR), experimental network of IAG/University of Sao Paulo (IAG/USP). We used automatic weather stations hourly (local time, UTC-3h) data measured at 2m (or 10m) of air temperature, humidity and wind speed, see station map at figure 2.1 and Table 2.1.

Network institution	Period (MM/YY)	Number of stations			
		full period	PCA dataset (2015)		
		U and V	T	Q	U and V
IAC	01/13 - 04/16	42	49	5	19
INMET	01/13 - 01/16	23	23	23	19
LCB	04/08 - 09/16	10	6	6	6
METAR	02/12 - 02/16	14	14	.	14
CETESB	01/10 - 12/15	25	13	6	.
	Total	114	106	48	58

Table 2.1 - Periods of observations and number of stations used in the different datasets for each institutions networks.

2.2.2 Field experiment

The field experiment at the Ribeirão Das Posses was composed by a network of 16 automatic weather stations placed in two transects approximately perpendicular to the valley on the eastern and western flanks. The first transect was about 2,5 km long with 12 stations in the upper basin, and the second one about 1 km long with 4 stations in the middle catchment, where the stations were displaced at about 250m apart (Fig. 2.2.c and Tab.2.2). The design prioritized the higher altitudinal extent of the slopes in the upper catchment, where the effects of slope on the differential warming were supposed to be greater. During November 01/2014 to January 01/2016, we measured 2 min punctual records of atmospheric pressure, air temperature and humidity, precipitation, horizontal wind speed (WXT520 Vaisalla Weather Transmitter, Vantaa, Finland), with natural ventilation shelter at 2m AGL over short (below 30 cm height) grassland cover. Each station was connected to a data-logger and wifi transmitter hardware assembled at the Climate and Biosphere Laboratory of the University of São Paulo (LCB/USP), supplied with two 3600 mAh (3.5V) lipo batteries and 2W (5V) solar panel, and SSD memory card for data backup. The stations were connected using a wifi system with ZigBee protocol. A "coordinator" station received and checked the communication status of the "end-device" stations on a daily basis. When necessary, a router-like functionality was used to relay the information from a "end device"station to the "coordinator"station (see router stations in Tab.2.2). The communication system proved to be reasonably adequate there where the deployment design prevented the obstruction of sparse elements and signal attenuation

Stations	Position	Altitude (m)	Latitude (°S)	Longitude (°W)
$S1$	West, upper, ridge	1356	22.87019	46.258833
$S2$	West, upper, slope	1225	22.87411	46.256667
$S3$	West, upper, slope	1186	22.87686	46.254528
$S4$	West, upper, slope	1140	22.87792	46.252861
$S5$	West, upper, valley	1075	22.88117	46.251667
$S6$	West, upper, valley	1061	22.88097	46.249083
$S7$	East, upper, valley	1031	22.88331	46.246944
$S7"$	East, upper, valley	1077	22.88444	46.24586
$S8$	East, upper, slope	1127	22.88628	46.243694
$S09$	East, upper, slope	1206	22.88839	46.241278
$S10$	East, upper, slope	1279	22.88914	46.238472
$S11$	East, upper, ridge	1342	22.88964	46.237139
$S12$	West, middle, slope	1078	22.86303	46.24731
$S13$	East, middle, valley	1005	22.86478	46.24394
$S14$	East, middle, slope	1069	22.86414	46.23861
$S15$	East, middle, slope	1113	22.86439	46.23614

Table 2.2 - Attributes of the stations with: ID (col. 1), relative catchment position (col. 2) (Fig. 2.2) and geographic position (col. 5,6, and 7). Stations S1 to S12 measured from 01/11/2014 to 01/01/2016, and stations S13 to S16 measured from 01/03/2015 to 01/01/2016. Communication function of stations: S5 (coordinator), S3 and S15 (router), others (end device).

(e.g. patches with big trees and subtle variation of terrain). Finally global incoming solar irradiance was measured at the station S5 using a pyranometer CM22 Kipp & Zonen.

2.3 Data

2.3.1 Climatic datasets

In this study, the observations were organized in four distinct groups of datasets which differed in the specification of the stations and temporal ranges used. They were used separately for the analyse (I) and downscaling (II) of the surface climate at the meso-γ scale, in the Ribeirão das Posses (Tab. 2.2), as well as to investigate the climatic PCA modes (III) and daily wind cycle (IV) at the meso-β scale in the domain (Tab. 2.1). Each group (except IV) was composed by datasets of temperature (°C), specific humidity ($g.kg^{-1}$) (calculated using other available data of humidity and atmospheric pressure) and zonal

and meridional wind ($m.s^{-1}$). We refeed the months from October to April as the wet season, and May to September as the dry season, respectively.

For the field experiment in the Ribeirâo Das Posses, we calculated hourly mean of measurements with the averaged 2 min data from h to h+1 time from Nov-2015 to Jan-16 (I) and from 03/2015 to 01/2016 (II) . For the datasets used in the downscaling models (II), we neglected stations potentially influenced by peculiar micro scale landscape variability (e.g. the proximity to the top ridge, small bushes and trees) namely stations $S7$" and $S8$ for temperature, $S09$ and $S12$ for specific humidity, $S09$ and $S1$ for the wind, with the aim to keep the variability engendered by the mesoscale topography.

At the regional meso-β scale, we made two analysis, the first with the available data between Jan 2015 to Jan-2016 (III), and the second with every station observations between Jan 2008 to Jan 2016 (IV) regardless of the temporal range. In the former we used 6 stations of the 15 available from the field experiment to attempt assimilating the mesoscale variability across complex terrain in those mountainous region while avoiding problems in the PCA due to stations density. Additionally, for the PCA, we omitted stations with missing data above 30% during 2015. In the latter, we used all available stations to estimate the best spatial coverage for the analysis of the mean wind daily cycle.

2.3.2 Quality control and infilling procedure

We made quality control on the datasets to flag and remove spurious values (spikes, repetition, outliers), with the use of automatic thresholds and visual inspection, based on Durre et al. (2010), and eventually using the PCA components to identify suspicious measurement based on the calculated spatial patterns. During the field experiment, the principal source of gap in the dataset were due to persistent cloudy days and heavy rainfall events which occasionally caused malfunctioning of the power supply. The QC resulted in significant reduction of the stations initially selected, especially for the calculation of specific humidity, that needed simultaneous measurement of several other variables.

In the Ribeirão Das Posses, missing data were filled using an iterative spatial multi-linear regression using hourly averages of the two closest stations as independent variables.

In the regional domain, this methodology was slightly different as it used the best correlation obtained out of all nearby stations. Gap free data both help in the climate analysis and permitted to provide continuity of time series as requested in PCA.

2.3.3 Data analysis in the Ribeirão Das Posses

The subsequent analyses were used to describe the climatic variability in the Ribeirão das posses basin.

Clear Sky Fraction factor

The Clear Sky Fraction factor (CSF) was estimated to help assessing the conditions of cloud cover on an hourly basis, and was calculated as the ratio of the measured hourly surface incoming global solar irradiance (I) upon the global surface clear sky irradiance (I_o). The term Io was calculated with the R.sun model (Geographic Resources Analysis Support System GRASS GIS/Open Source Geospatial Foundation) described in Scharmer et al. (2000) and Rigollier et al. (2000), using the 30m horizontal resolution ASTER Global Digital Elevation Model (ASTER GDEM). The GDEM was modified to assure a horizontal surface plan specially at the coordinates of the measured irradiance. We prescribed the linke turbidity coefficient equal to 2, based on the comparisons between measured and calculated irradiance under clear sky conditions (not shown). The ground solar albedo was found not to be significantly sensitive to the calculations and was prescribed as 0.2. We used CSF in the range 0 to 0.3 and simply referred that as cloudy sky, and above 0.7 as clear sky respectively.

Terrestrial Lapse rate and catchment gradients

We classified three pairs of sectors in the catchment, based on key spatial locations, namely the valley (strictly at the bottom of the slope) and the middle slopes, the middle and the upper watershed, the eastern and western sides (Fig. 2.2.c), and associated proper stations to each class of position (described in Table 2.2), to calculate the mean difference (measurement X) of a/b pair element each class (a minus b) as

$$\Delta X_{ab} = \langle X_a \rangle - \langle X_b \rangle \tag{2.1}$$

where a and b represent the pair of classes valley/slopes (ΔX_{vs}), middle/upper (ΔX_{mu}) and West/East (ΔX_{we}) respectively and $\langle X \rangle$ is the spatial average. To infer how a surface variable X changed with altitudinal variation ΔZ, the terrestrial lapse rate (TLR) was calculated as the slope coefficient of the linear regression of ΔX against ΔZ.

Terrestrial Wind Divergence

We calculated the mean spatial terrestrial Wind Divergence index (hereafter referred as TWD) at the zonal direction using the measurements along the upper catchment transect as:

$$\frac{\delta u}{\delta x} \equiv \frac{\Delta u}{\Delta x} = \frac{1}{n} \sum_{i=1}^{n} \frac{u_{i+1} - u_i}{x_{i+1} - x_i} \tag{2.2}$$

where u is the zonal wind speed and x the zonal position at the upper transect over the n stations.

Land Skin Temperature

The mean areal land skin temperature (LST) was estimated on the spatial domain of Posses basin (Fig. 2.2), based on Allen et al. (2007) and using the Thermal Infrared Sensor (TIRS) of Landsat-8 (temporal resolution of 16 days at 10 AM, spatial resolution 30 m), with available data between 12 May 2013 to 09 Aug 2016, that totaled 23 images with 13385 pixels each.

2.4 Description of PCA procedure

Principal Component Analysis (PCA), also refereed as Empirical Orthogonal Function (EOF) is a statistical tool that uses algebraic linear transformation to obtain a new subset of orthogonal variables (PCs) while keeping most of the original dataset variance (Wilks, 1995; Von Storch and Zwiers, 1999).It reduces the dimension of a system and removes the collinearity between the features. This procedure is commonly used in atmospheric sciences to identify the most important patterns of temporal and spatial climate variance. The covariance or correlation matrix of n measurements $\times$ m stations is decomposed into $n \times k$ and $k \times m$ matrices, where k is the number of retained PCs ($k < m$). The former

are the k Principal Components (or PC scores) and the later their eigenvectors (or PC loadings). The decomposition of dataset by PCA can be expressed in the following form:

$$\boldsymbol{P}_{i,j} = \boldsymbol{L}_{i1}.X_{1,j} + \boldsymbol{L}_{i2}.X_{2,j} + ... + \boldsymbol{L}_{im}.X_{m,j} \qquad , (i = 1, m) \qquad (2.3)$$

where X, P, L are respectively the original dataset ($n \times m$), PC scores ($n \times k$) and PC loadings ($k \times m$).

The climatic variation captured by a PC is reconstructed as follow:

$$X_k = \boldsymbol{L}_k.\boldsymbol{P}_k \qquad (2.4)$$

Where X is a $M \times N$ matrix, alike the original dataset, $\boldsymbol{L}$ is a vector of N loadings and $\boldsymbol{P}$ is the vector of M scores; K is the rank number of the PC selected.

Here the scores represent the temporal evolution of climatic patterns shown by the time independent spatial distribution of the loadings (Preisendorfer and Mobley, 1988). A PC is not an exact representation of a full physical phenomena, so its interpretation must be cautious.

2.5   Application of PCA at meso-β scale

At the regional scale, the original data set were standardized prior to PCA, that prevented biased influences of stations with large variance and less influenced by extreme events. The PCA was applied separately for data of air temperature (PCT), specific humidity (PCQ) and horizontal wind components (PCUV) (the latter used the real components, as in Kaihatu et al. (1998) and in Ludwig et al. (2004)). In addition we applied PCA by forming combined variables of temperature and wind (PCTUV), and specific humidity and wind (PCQUV), called combined PCA, to help the interpretation of grouped variables.

We retained the PCs based on both the explained variance and the physical interpretation we could attribute, based on the spatial loadings distribution and the daily and seasonal variability of scores. The modes can often mix different temporal and spatial scales, which makes it not a trivial task to interpret separately. Only the PCs with significant variance are about to be retained in the downscaling model.

2.6 Downscaling model at meso-γ scale

2.6.1 Methodology overview

The downscaling methodology followed the three steps suggested by Holden et al. (2011). Firstly a PCA is applied for each atmospheric variable dataset as 2.3, the spatial loadings are modelled with topographic predictors , and the temporal evolution of the PC scores are estimated with predictors of atmospheric model outputs. Finally the climatic fields are reconstructed as 2.5 using the calculated loadings and scores for the K PCs retained, where the value of a variable x measured at a station i at time j is calculated as

$$x_{i,j} \approx \boldsymbol{L}_{i1}.\boldsymbol{P}_{1,j} + \boldsymbol{L}_{i2}.\boldsymbol{P}_{2,j} + ... + \boldsymbol{L}_{ik}.\boldsymbol{P}_{k,j} \qquad , (i = 1, m) \qquad (2.5)$$

The data were not standardized prior to PCA, as they were individual variable measurements with the same unit, and because the restitution of the mean estimated climatic field may add significant model errors (Holden et al., 2011.b). In general the quasi-totality of the variance is explained by the few first PCs, in a model supposed to represent the dominant climatic variability.

2.6.2 Predictors to model PCs loadings spatial distribution

The spatial distribution of the PC loadings were modelled with topographic features, shown in the Tab.2.3, that were calculated with the 30m resolution altitude raster of the Advanced Spaceborne Thermal Emission and Reflection Radiometer (ASTER) Global Digital Model Version 2 (GDEM V2). We calculated the distance to the watershed outlet for each pixel (called *dist_outlet*, see Fig. 2.3.b) to represent the along valley climatic gradients. Likewise, we calculated the sidewall distance normal to the valley center, associated with positive and negative values on the Western and Eastern side, respectively (called *dist_side*, see Fig. 2.3.f). To represent other complex patterns of the wind components, we ellaborated a new set of topographical index inspired on the TOpographical Exposition Index (TOPEX) (Chapman, 2000), that pose metrics to wind exposition of a grid cell, and is originally estimated with the steps: calculate the inflection angle between a point and every other point below 2km distant over all directions; select the highest inflection angle; and sum the highest inflection angle obtained in the N,S,E,W directions. We noted how the original TOPEX poorly performed for the zonal and meridional wind component associated

PC	Temperature	Specific Humidity	Zonal wind	Meridional wind
1	*Altitude - dist_outlet*	*Altitude*	*TopexNorth − East*	*dist_side*
2	*Altitude - dist_outlet*	*Altitude*	*dist_side*	*TopexWest*
3	*Altitude*		*Altitude*	
4	*dist_side*			

Table 2.3 - Spatial predictors used to model the PCs loadings of temperature, specific humidity, zonal wind and meridional wind.

to a specific direction. Our ellaboration skipped the third step and built a specific TOPEX like index for the N, S, W, E, NE, NW, SE, and NW directions separately. Also we found that summing the inflection angles instead of taking the maximum (in step2) leaded to consider the multi scale wind sheltering characteristics of the landscape, that improved on fitting the loadings. We used first and third order polynomial equations to fit the loadings, with the predictors extracted at the station position (Fig. 2.4). For the temperature PC1 and PC2 loadings we fitted as $a * altitude + b * altitude^2 + c * altitude^3 + d * dist\_outlet$.

2.6.3   Predictors to model PCs scores temporal evolution

Predictors for PC scores were extracted from the gridded 6-hourly 0.25° resolution NCEP Global Forecast System Analysis (GFS) data. The method selected the hourly measurements coincident with the GFS time, to form 6-hourly spaced datasets. The GFS times were 00, 06, 12 and 18 UTC (local time hereafter used in h = UTC -3). Furthermore we applied PCA in the hourly resolution datasets to compare with PCA obtained with the 6-hourly dataset, and found that the spatial and temporal patterns were well approximated. We prioritized the candidate variables based on similar studies, their availability on other large scale model outputs, and finally selected upon the correlation with the scores. The selection included the temperature (T), relative humidity (Rh), specific humidity (q), zonal wind (u) and meridional wind (v), extracted at the 900mb, 850mb and 500mb pressure levels, as well as at 2m (10m for wind) and 80m above the surface, at the nearest grid cell of our domain of investigation. The 850mb and 900mb pressure levels corresponded roughly to the highest and lowest points of our domain, respectively. For each variable we calculated the simple vertical difference between two different levels, and so on horizontally taking two adjacent grid cells (Δ_x and Δ_y for the meridional and zonal difference, respectively). The variables included components of the surface energy balance, namely net radiation (Rn),

latent (LH), sensible (H) and ground (Gr) heat flux, and upward/downward longwave (L) and shortwave (S) irradiance. Additionally, we used the soil temperature (T_{soil}) and humidity (Q_{soil}) of the first layer as predictors. A forward stepwise linear regression was used to fit the scores and the GFS outputs. A new predictor was selected based on the adjusted correlation score of the new model created. At each iteration, the predictor that showed the highest correlation score was selected. No other predictors were added when the new model correlation score did not increase significantly.

2.6.4 Model assessment

We aim to make the PCA based model assessment against ground measurement, and also assess the estimates of vertically extrapolated GFS data, for the simple sake of comparison. We will use cross validation to fit and validate the models, where 80% of the original 6-hourly datasets were randomly chosen for fitting, and the remaining 20% used for validation. The vertically interpolated temperature, zonal and meridional wind of the GFS data (based on Holden et al. (2016)) followed three steps: firstly, the time period average geopotential height at different GFS pressure levels was calculated at all levels and the climatic variables were linearly interpolated on these geopotential heights. Next, for each time and for altitude below 3km, a linear regression model was fitted between the variables and their correspondent altitudes. We finally used these models and the DEM altitude to obtain time series of free air temperature, zonal and meridional wind speed at the surface.
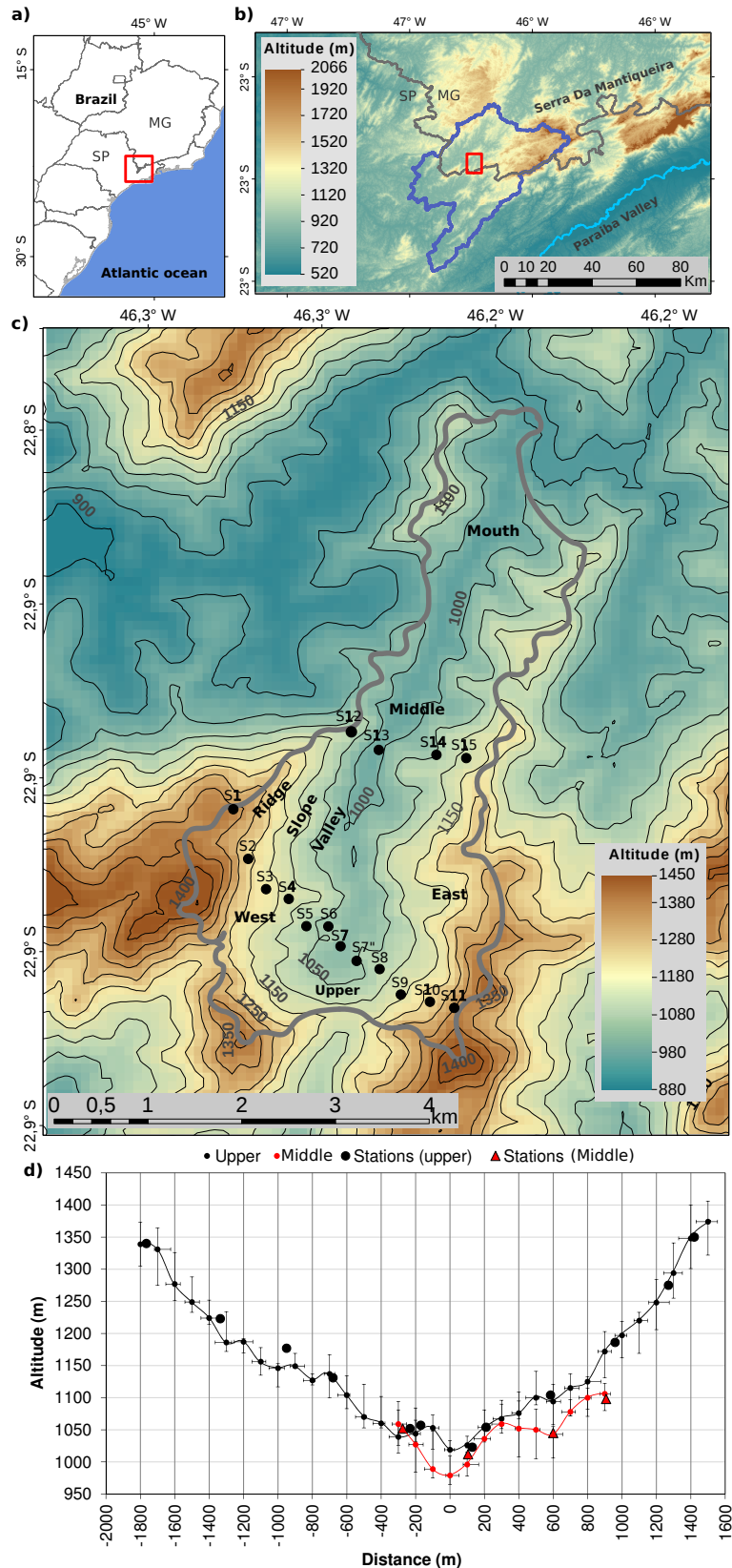
Figure 2.2: (a) and (b) Regional and altitudinal map of the Serra da Mantiqueira mountain range (drainage area of the Cantareira reservoirs in dark blue line; Paraiba river in light blue line); (c) Altitudinal map of the experimental area (Ribeirão das Posses watershed with the locations of 16 weather stations (circles) and labelled locations; (d) Altitudinal variation (m) along the horizontal transect of weather stations at the upper catchment (black circles) and middle catchment (red circles), origin is the valley center, bars are E/W and N/S altitudinal deviation over a 100 m range centred each station.
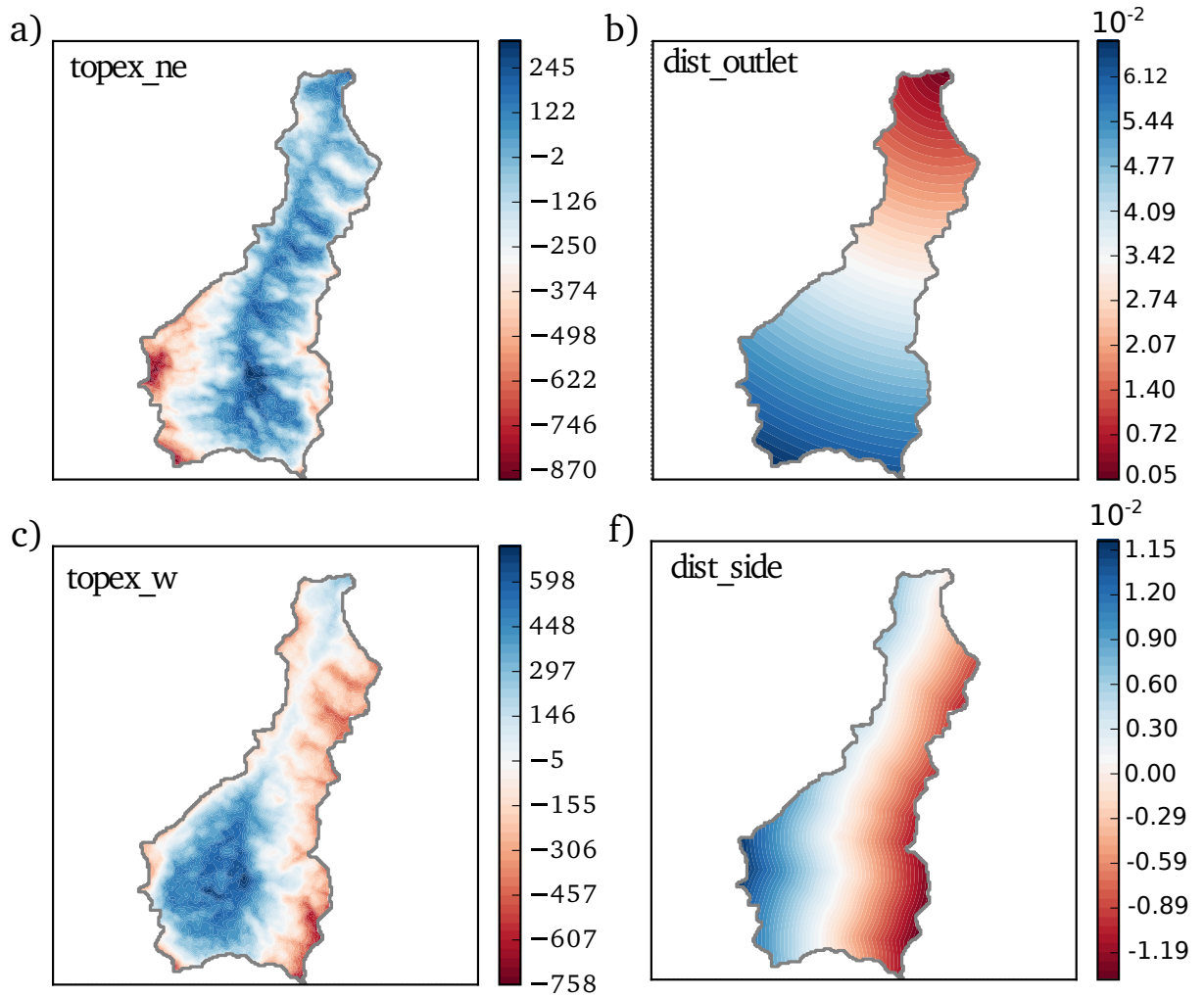
Figure 2.3: Spatial representation of the topographical indexes used for the PCs loadings modeling (see Tab.2.3).
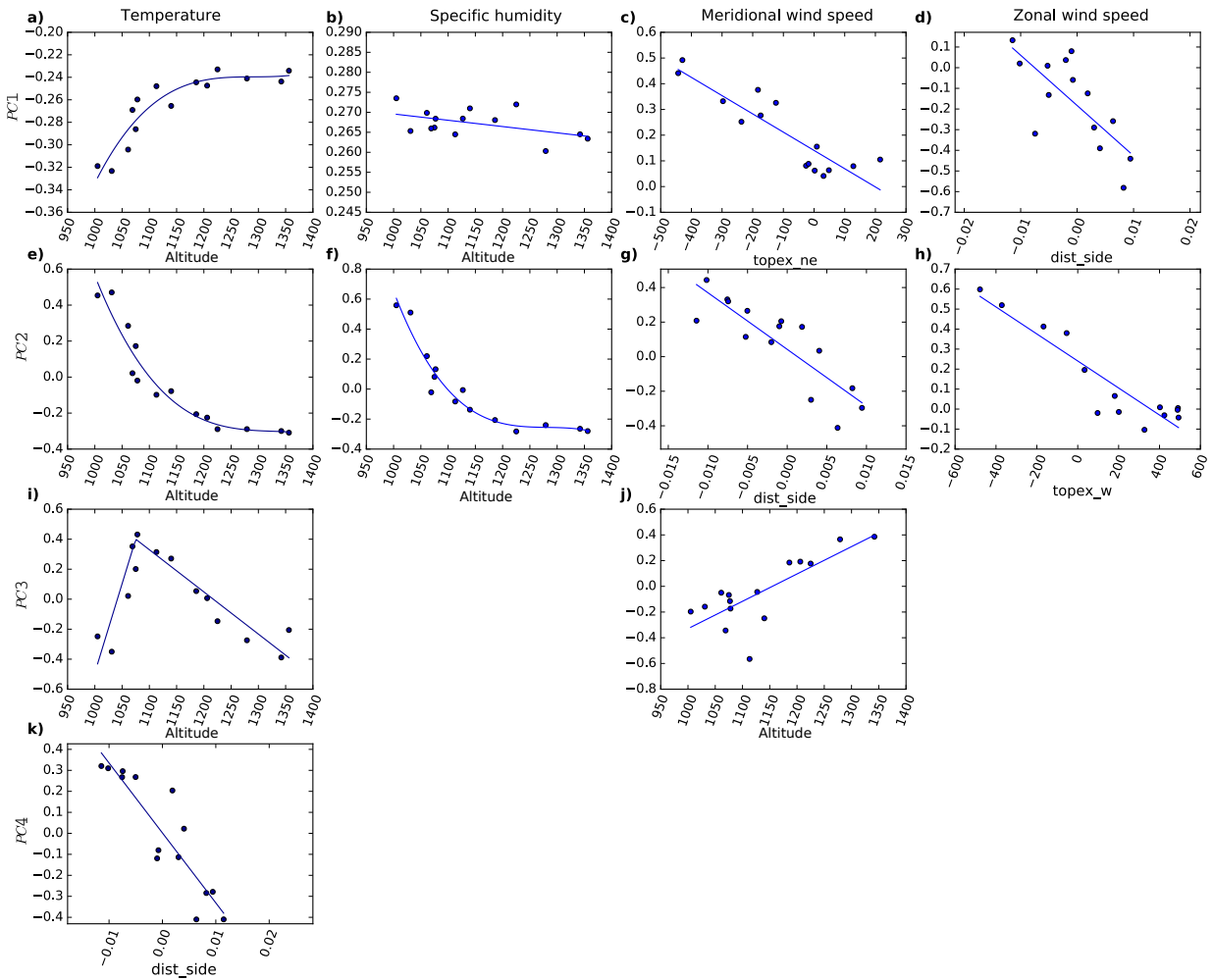
Figure 2.4: PCs loadings at the stations for the temperature (col.1), specific humidity (col.2) and meridional (col.3) and zonal (col.4) wind in function of topoindexes (see Tab.2.3). Blue lines represent the fit used in the models.

Chapter 3

Results

3.1 Surface climate in the Ribeirão Das Posses basin

3.1.1 Daily cycle and spatial variability

The wet season showed a marked regime with convective storms in the afternoon, with the accumulated hourly rainfall peaking at about 14h (Fig. 3.1.a). The mean observed incoming solar radiation was only slightly higher in the wet season, especially in the morning time (solid lines in Fig. 3.1.b), that is partly explained by the higher CSF in the dry season compared to the wet season (Fig. 3.1.c).

The mean hourly air temperature peaked approximately at 12h in the wet season and at 13h in the dry season, in a lag likely associated to the solar radiation (as shown in Fig. 3.1.c), with the min/max temperatures of $\approx 17°C/24\ °C$ in the wet season and $14°C/21°C$ in dry season, so the daily amplitude was approximately $7°C$ in both seasons (Fig. 3.1.d). The range of p10% and p90% hourly temperature was however a little higher in the dry season ($\approx 15\ °C$) compared to the wet season ($\approx 13\ °C$), as expected. The mean hourly vapour pressure (Fig.3.1.e) appeared to peak by 10h, possibly as a consequence of dew evaporation and less turbulence in the middle morning, and that in general fluctuated with a amplitude of about 2hPa day round in all seasons. The seasonal variation of mean vapour pressure was about 4hPa, but the range p10% (p90%) year round was quite higher of about 11 hPa. The mean daily relative humidity was higher in the wet season, with emphasis on the minimum daytime p10% that appeared to be quite higher ($\approx 48\%$) compared to the dry season ($\approx 35\ \%$) (Fig. 3.1.f).
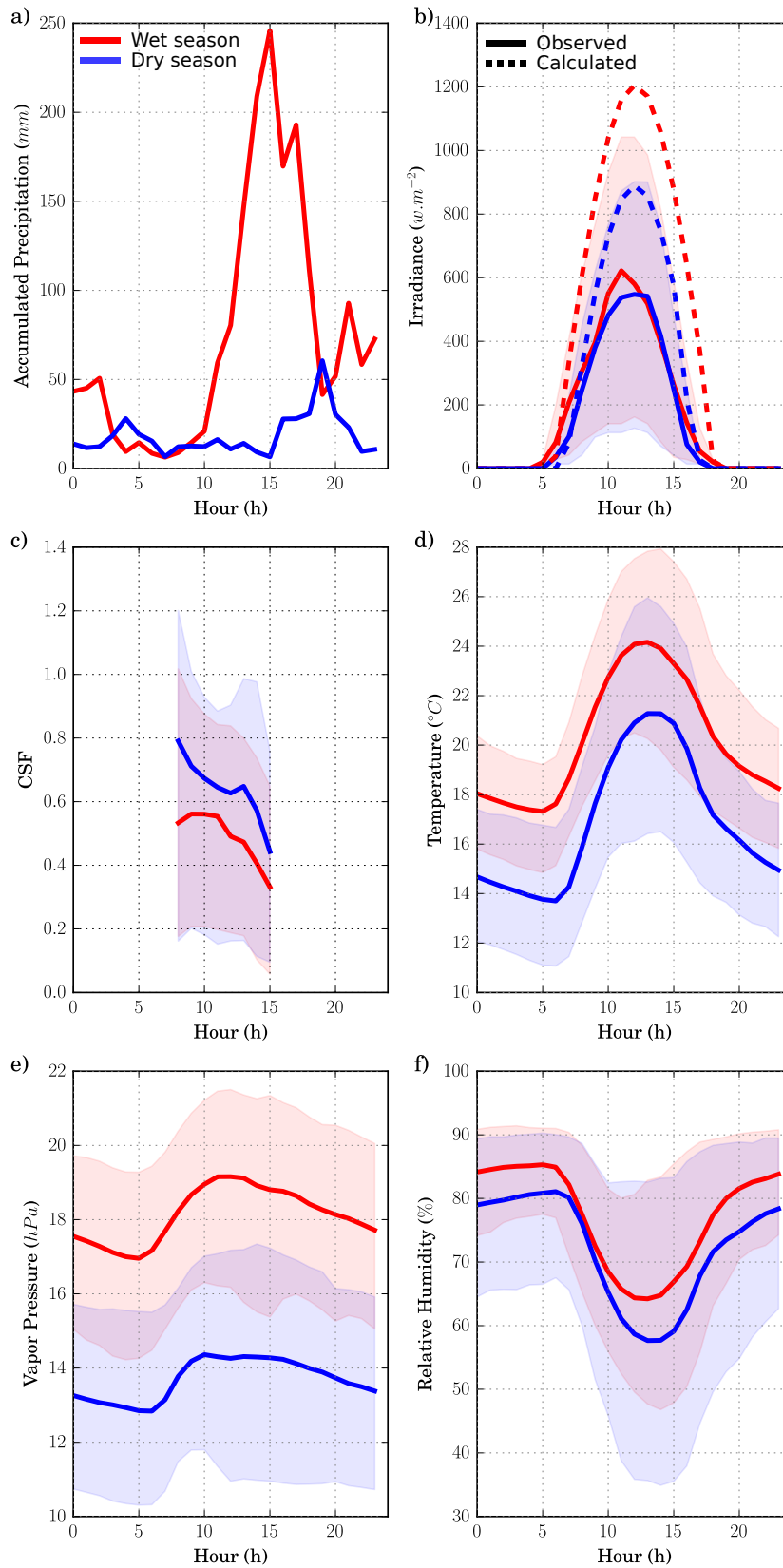
Figure 3.1: Spatially averaged daily cycle of (a) accumulated precipitation (mm), (b) solar irradiance ($W.m^{-2}$), (c) Clear Sky Fraction factor, (d) temperature ($°C$), (e) vapor pressure (hPa) and (f) relative humidity (%). The hourly average (solid line), ninetieth (shade upper limit) and tenth (shade lower limit) percentiles are shown for the wet (red) and dry (blue) period. The dashed line in (b) shows the calculated clear sky solar radiation ($W.m^{-2}$).

We interpreted the measured wind speed at station S1 (that was positioned at the highest altitude and on the western ridge of the basin) as the best approximation of the wind aloft the catchment and so the synoptic flow. The wind speed at station S11 near the eastern ridge was weaker than in the wind at S1 (comparison not shown), as the former was located below the ridge and so occasionally sheltered. Two modes of wind speed prevailed at S1 (Fig. 3.2): the northeasterly (NE) winds were relatively weaker (average $\approx 4 \ ms^{-1}$) and persistent from about midnight through the middle afternoon; and the southeasterly (SE) winds were stronger (average $\approx 8 \ ms^{-1}$) and noticed mostly in the afternoon through the nighttime. We interpreted the observed NE circulation as the large scale flow modulated by the south Atlantic high pressure center and often observed regionally, and the SE circulation associated mostly to inertial sea breeze propagating inland (Silva Dias and Machado, 1997; Oliveira et al., 2002), and partly to cold advected air in extratropical cyclones that occurs mostly in wintertime. Interestingly, the SE winds were more frequent in the wet season compared to the dry season (as suggested in Fig. 3.2.a), what suggests how the sea breeze may act as a strong driver.

The mean air temperature was 18.8 °C for all stations and over the full temporal range. We ranked average temperature of each station with altitude (circles in Fig. 3.3.a) and noted no general trend, exceptionally close to the altitudes at upper 100m and lower 50 m, respectively. The daily maximum and minimum temperature appeared to decrease both with altitude more emphatically in the upper half range, whereas the daily minima differently increased with altitude only in the lowest 100 m. This pattern consequently showed a higher mean temperature amplitude near the valleys (of $\approx$ 9 °C) and less near the ridges (of $\approx$ 6 °C). The average vapour pressure (circles in Fig. 3.3.b) showed a small tendency to decrease with the altitude, especially in the stations on the upper 200m, with a reduction of about 1 hPa, thus wetter in the valleys compared to the ridges.

We understood as relevant to identify the climate variability by comparing key sectors in the catchment, for example the valley and the slopes, the middle and the upper catchment. In the upper catchment, the nighttime temperature at the valley was colder compared to the temperature at middle slopes, that extended to dawn and dusk (solid line as ΔTvs in Fig. 3.4.a), with a mean difference that varied between $\approx$ -2.0 °C in the dry season and $\approx$
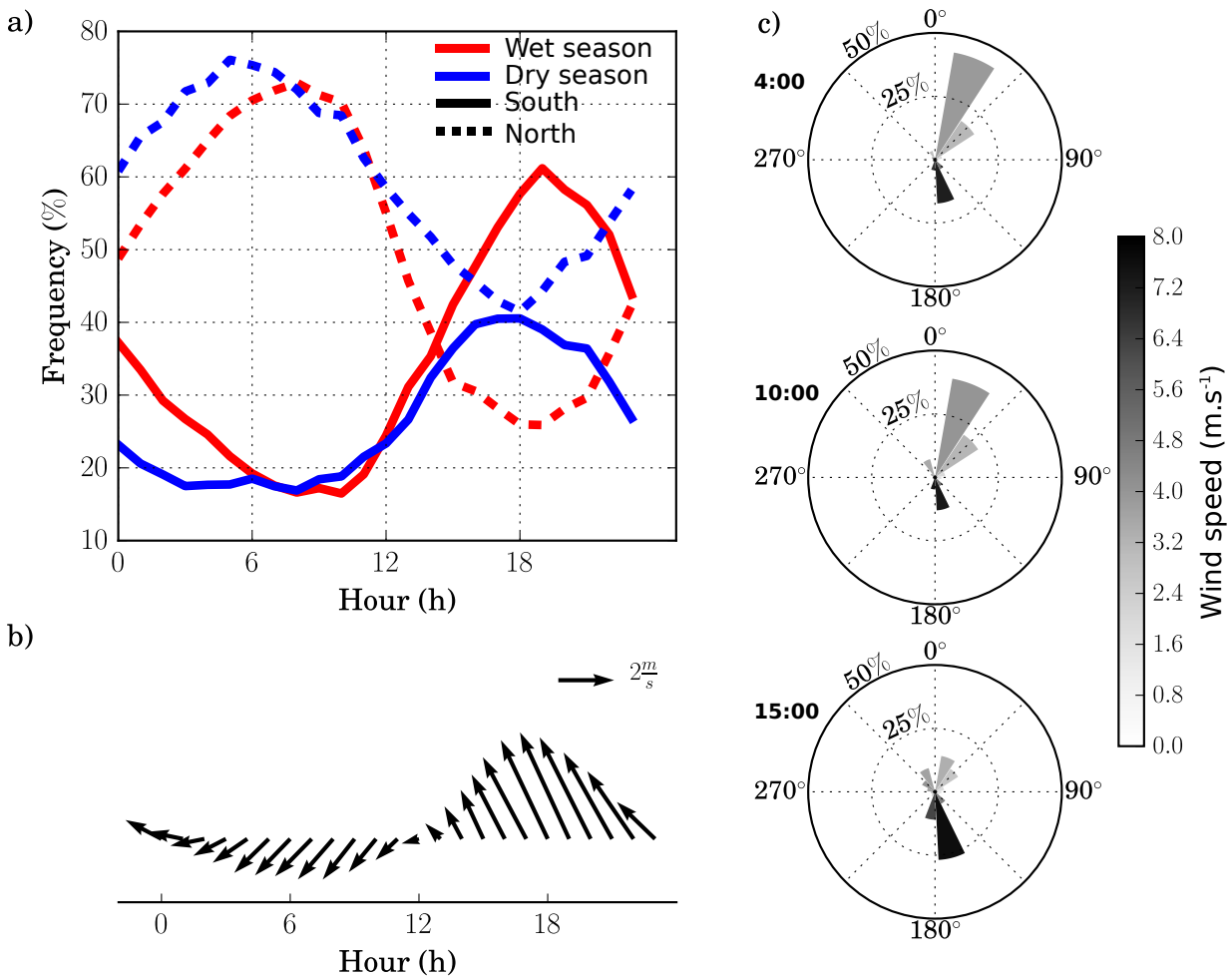
Figure 3.2: Mean daily cycle of the North (315° to 45°) (dashed lines) and South (135° to 225°) (solid lines) wind frequency (%) during wet (red) and dry (blue) season (a), wind speed in vector format (b) and wind rose at 4h, 10h and 15h (c) at station $S1$ located on the ridge.
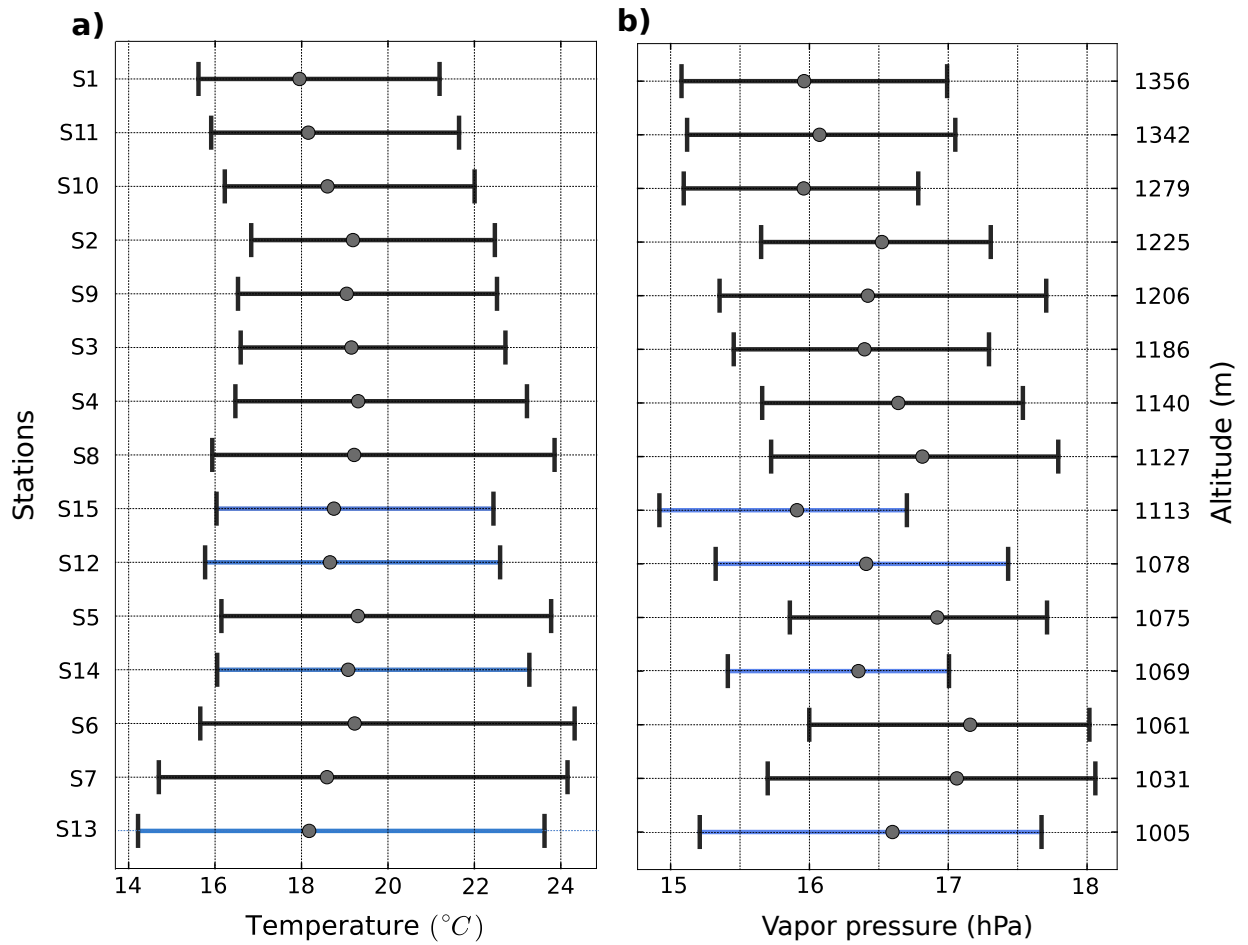
Figure 3.3: Average daily maximum (right cap), minimum (left cap) and mean (grey circle) temperature (°C) (a) and id. for vapor pressure (hPa) (b) against stations ranked by altitude (m). Middle catchment stations are shown as blue bar, upper catchment stations as black bar.

-0.5 °C in the wet season. Interestingly, the differential cooling was built during the first half of the night in the dry season, while it kept augmenting along the night in the wet season. Contrarily, during daytime the valley was warmer by $\approx$ +1.5 °C or a little less, that was more pronounced in the dry season and especially in the afternoon (blue solid line in Fig. 3.4.a). Looking at axial direction thru the valley, we also noted substantial differences. In general the middle valley tended to be cooler at night as opposed to daytime (line filled w/ circles as ΔTmu in Fig. 3.4.a), with differences more emphatic in the dry season of $\approx$ -0.5 °C, whereas it appeared to be warmer at daytime mostly in the wet season and also by $\approx$ +0.5 °C. In another direction of the upper catchment, we noted differential temperatures between the west and east sides (dashed line as ΔTwe in Fig. 3.4.a): during nighttime the western slope was warmer by $\approx$ +0.5 °C, what generally tended to dampen along the daytime, but that ended in the eastern slope warmer by $\approx$ +0.5°C only in the wet season. A simple cause is higher solar radiation absorption at daytime (afternoon) on the east side, constrained by the aspect of the slopes and small hills in the basin. The valley lies on a prevailing N-S direction (Fig. 3.5.a), where the west side hills face mostly from SE to N (red circles in Figs. 3.5.c), that advantages it for incoming solar radiation in the morning and helps to explain its higher mean areal morning LST compared to the east side by $\approx$ 1°C (Tab. 3.1). The east side hills mostly face from SW to N (Fig. 3.5.c), that advantages its preferential warming in the afternoon. For a fine areal analysis near the bounds of the stations we accounted the pixels narrowed 200m along the measurements (Fig. 3.5.b) and noted how morning LST was also higher on the west side (Fig. 3.5.b,c). It also showed how the east side generally faced the NW quadrant, as opposed to the west side that faced the SE quadrant in large proportion (Fig. 3.5.c), what reinforces the daytime warming at east constrained by the shifted north solar azimuthal angle during most of the year. Secondly, the warmer west side at night is supposed to be affected by stronger nocturnal winds (Fig. 3.6.c), that would help mixing from above in the inversion layer and thus partly respond the cooling mitigation. Finally, we also accounted the LST associated to the land cover for the entire basin and noted that the mean LST over pasture was higher compared to the mean over forest, by 1.3°C on the west side and 0.8°C on the east side (Tab. 3.1), what seems reasonable as tropical forests prioritize transpiration as opposed to sensible heat in the daytime energy partitioning and may potentially show an above canopy temperature colder than the pastureland cover. However we do not have

Slope side	Land use (%)		Land Skin Temperature (°C)		
	Forest	Pasture	Forest	Pasture	**Total**
West	31.2	58.9	22.4 ± 1.4	23.7 ± 1.4	23.3 ± 1.4
East	25.8	63.6	21.7 ± 1.4	22.5 ± 1.4	22.4 ± 1.4

Table 3.1 - Proportion of land use (%) and estimated Land Skin Temperature (°C) for the West and East valley side.

arguments to attribute the measured air temperature variability to the vegetation. The fractional area of pasture-land in the two sides was different by only 4.7% (Table 3.1). The stations were all placed over grassland and relatively distant from forest fragments, so we expect the effects of land cover were not substantial in the comparison.

From the perspective of all measurements in the upper catchment we noted well defined cross-valley gradients of the mean air temperature and vapor pressure (Fig. 3.6.a,c), that showed the differential warming and wetting between the valley and slopes organized day round. The daily amplitude in markedly higher in the valley, that warmed/wetted up at day and cooled/dried down at night differentially to the slopes. The mean spatial temperatures ranged between the maxima of about $24°C$ to $21°C$ around 13h, and the minima from $16°C$ to $18°C$ around 5h (Fig. 3.6.a). With respect to the vapor pressure, the spatial extremes ranged between $\approx$ 18.5 hPa to 17 hPa around 18h, and at night between $\approx$ 16.5 hPa to 15.5 hPa around 4h (Fig. 3.6.b). The mean zonal wind in the upper catchment showed clearly an upslope circulation in the west side, since the middle morning thru the middle afternoon (Fig. 3.6.a). Likewise, downslope circulation in the upper catchment was evident as zonal wind in both sides, since dusk and thru the nighttime (Fig. 3.6.a).

In the middle catchment we also noticed cross-valley gradients of air temperature and humidity (Figs. 3.6.b and 3.6.d). As well, the mean zonal wind indicated downslope circulation at night (Fig. 3.6b), that was however relatively weaker compared to the downwinds in the upper catchment. We did not find convicing patterns of zonal upslope wind in the middle catchment (Fig. 3.6b). There we noted evidence of axial meridional flows too, specially in the morning, that suggested an upvalley circulation to exist (Fig. 3.6.d), however difficult to attribute firmly, as it could be just the effect of the synoptic northerly wind or, optimistically, the synoptic flow combined to an upvalley circulation.
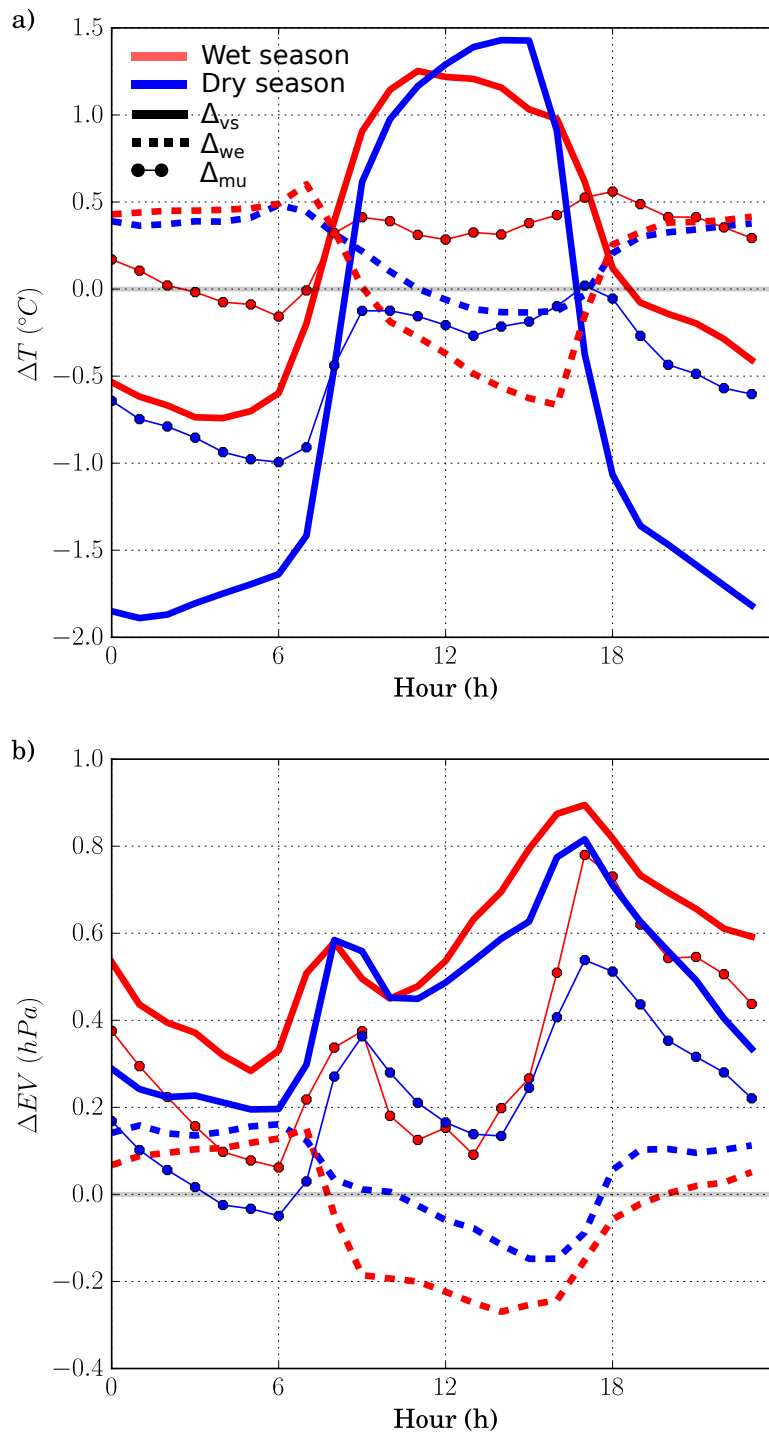
Figure 3.4: Difference of (a) temperature (°C) and (b) vapor pressure (hPa) between valley/slope (Δ_{vs}) (solid line), middle/upper (Δ_{mu}) (dotted line) and West/East (Δ_{we}) (dashed line), for the dry (blue) and wet (red) season.
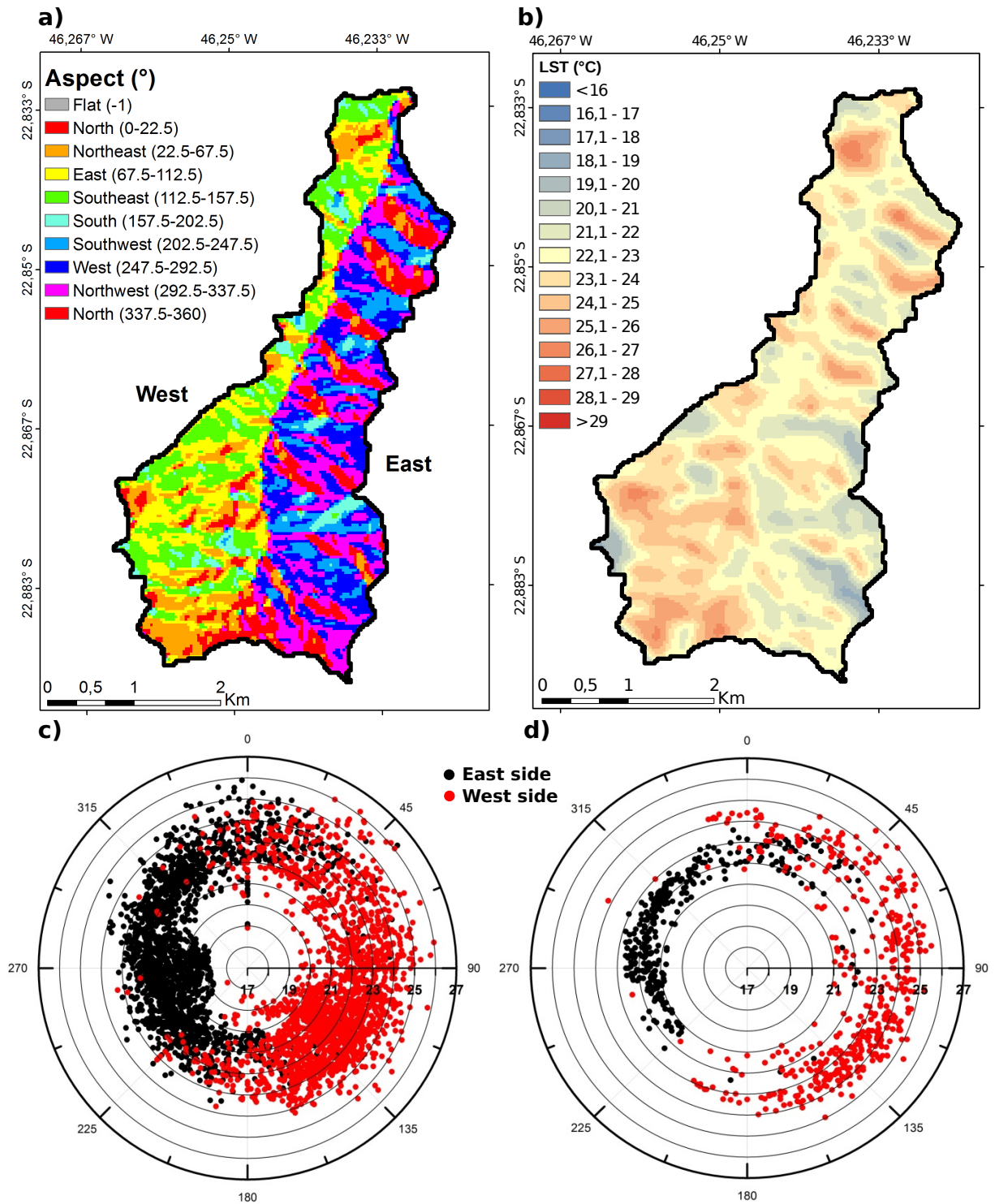
Figure 3.5: Map of (a) aspect (°) and (b) LST (°C) with upper catchment transect stations location (black circles) and area used in (d) (in between the thin black lines). LST (°C) in function of aspect for the entier catchment (c) and upper catchment transect (d) with measurements taken on the Western side in red and Eastern side in black.
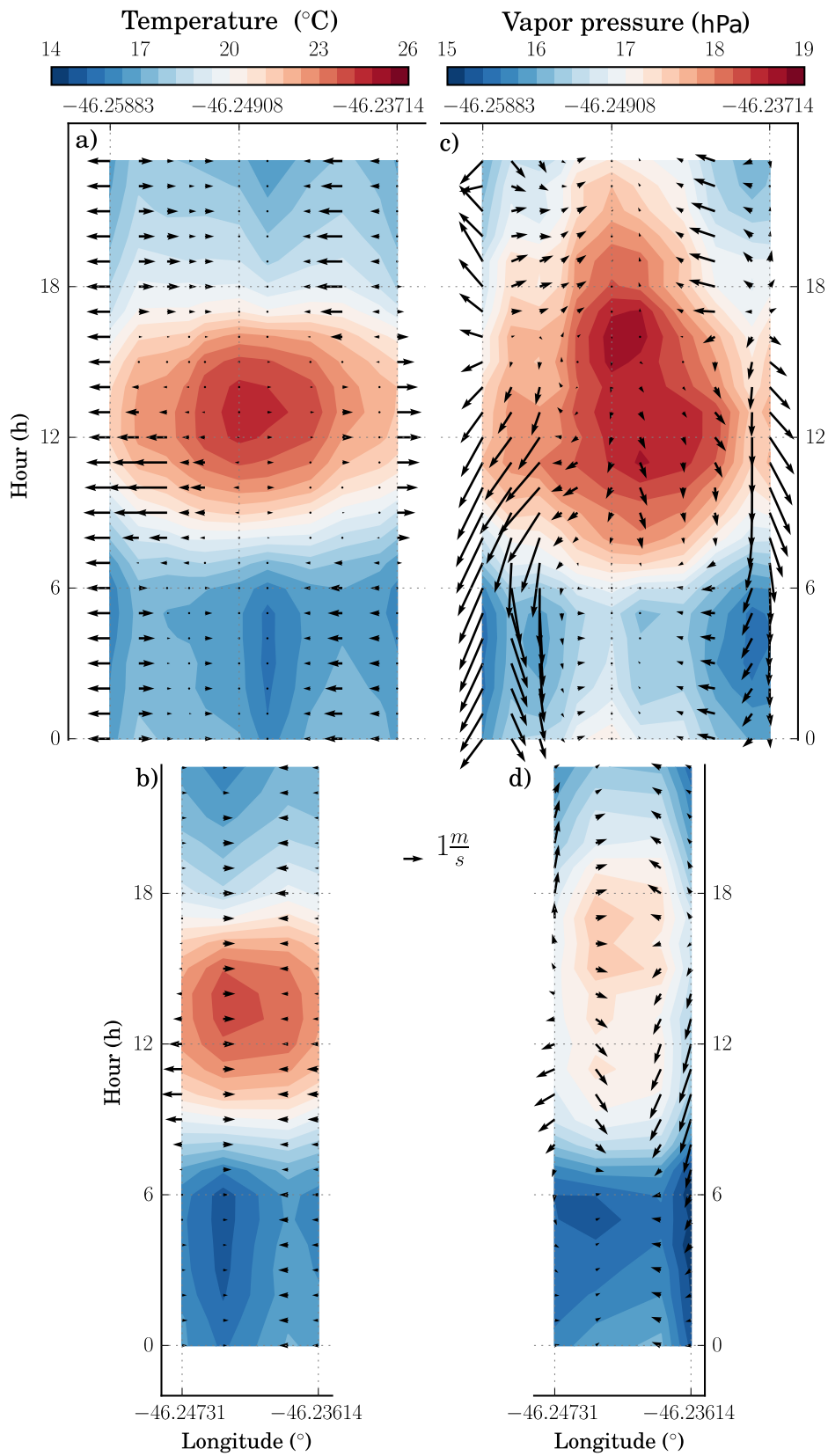
Figure 3.6: Temperature (°C) and zonal wind ($m.s^{-1}$) at (a) upper and (b) middle catchment. Vapor pressure (hPa) and wind ($m.s^{-1}$) at (c) upper and (d) middle catchment.

Average period	Season	Temperature ($°C.100m^{-1}$)	TLR Vapor pressure ($hPa^{-1}.100m^{-1}$)	wind speed ($m.s^{-1}.100m^{-1}$)
Night	Dry	1.0	-0.3	0.9
	Wet	0.2	-0.4	0.7
Day	Dry	-0.7	-0.5	0.8
	Wet	-0.7	-0.4	0.7

Table 3.2 - Average diurnal and nocturnal terrestrial lapse rate of temperature, water vapor pressure and wind speed for the wet and dry seasons. The calcul of the temperature TLR did not include observations of the stations near the ridges (S1 and S11). Nightiime average included variation up to 200m above the valley and range from 19h to 5h (included) and the daytime average range from 7h to 17h.

Period	Season	Temperature ($°C$)	Potential Temperature ($°C$)	Vapor Pressure (hPa)	Wind speed ($m.s^{-1}$)
4h	Dry	$2.87x10^{-2}z - 7.14x10^{-5}z^2$	$4.97x10^{-2}z - 1x10^{-4}z^2$	$-0.29x10^{-2}z$	$0.90x10^{-2}z$
	Wet	$1.74x10^{-2}z - 5.00x10^{-5}z^2$	$3.58x10^{-2}z - 7.21x10^{-4}z^2$	$-0.36x10^{-2}z$	$0.83x10^{-2}z$
12h	Dry	$-0.94x10^{-2}z$	$-0.17x10^{-2}z$	$-0.28x10^{-2}z$	$0.75x10^{-2}z$
	Wet	$-0.79x10^{-2}z$	$0.27x10^{-2}z$	$-0.35x10^{-2}z$	$0.66x10^{-2}z$

Table 3.3 - Polynomial equations of the fits presented in Fig. 3.7. $z(m)$ represent the altitude above the station reference $S7$ located in the valley center.

3.1.2 Terrestrial lapse rate and wind divergence

The mean air ground nighttime temperature (at 4h) increased with height from the bottom valley to about 200m and reversed sign upwards (Fig. 3.7.a). Above 200m the potential air temperature was nearly constant (Fig. 3.7.c), a height that seems to correspond to the thermal belt with maximum nocturnal temperature. Otherwise, the mean daytime temperature (at noon) clearly decreased with elevation (Fig. 3.7.b), and when the potential temperature was approximately constant (Fig. 3.7.d).

We estimated the mean terrestrial lapse rate (hereafter referred to as TLR) as the altitudinal variation of ground measurements in the upper catchment transect. For air temperature the mean daytime TLR was of -0.7 $°C$ ($100m^{-1}$) and at nighttime it varied between $\approx +1.1$ to $+0.2$ $°C$ ($100m^{-1}$) in the dry and wet season respectively (see mean TLR summarized in Table 3.2; in Table 3.3 see the fitted polynomials for the altitudinal variation of the variables described in Fig. 3.7).

The mean hourly temperature TLR showed a clear diurnal cycle nearly synchronized with the mean air temperature (Fig. 3.8.a). It was remarkable how the transition from (negative) nocturnal TLR to the (positive) diurnal TLR spanned less than 2 hours, and so the transition from the diurnal to the nocturnal patterns in a like manner. The daily
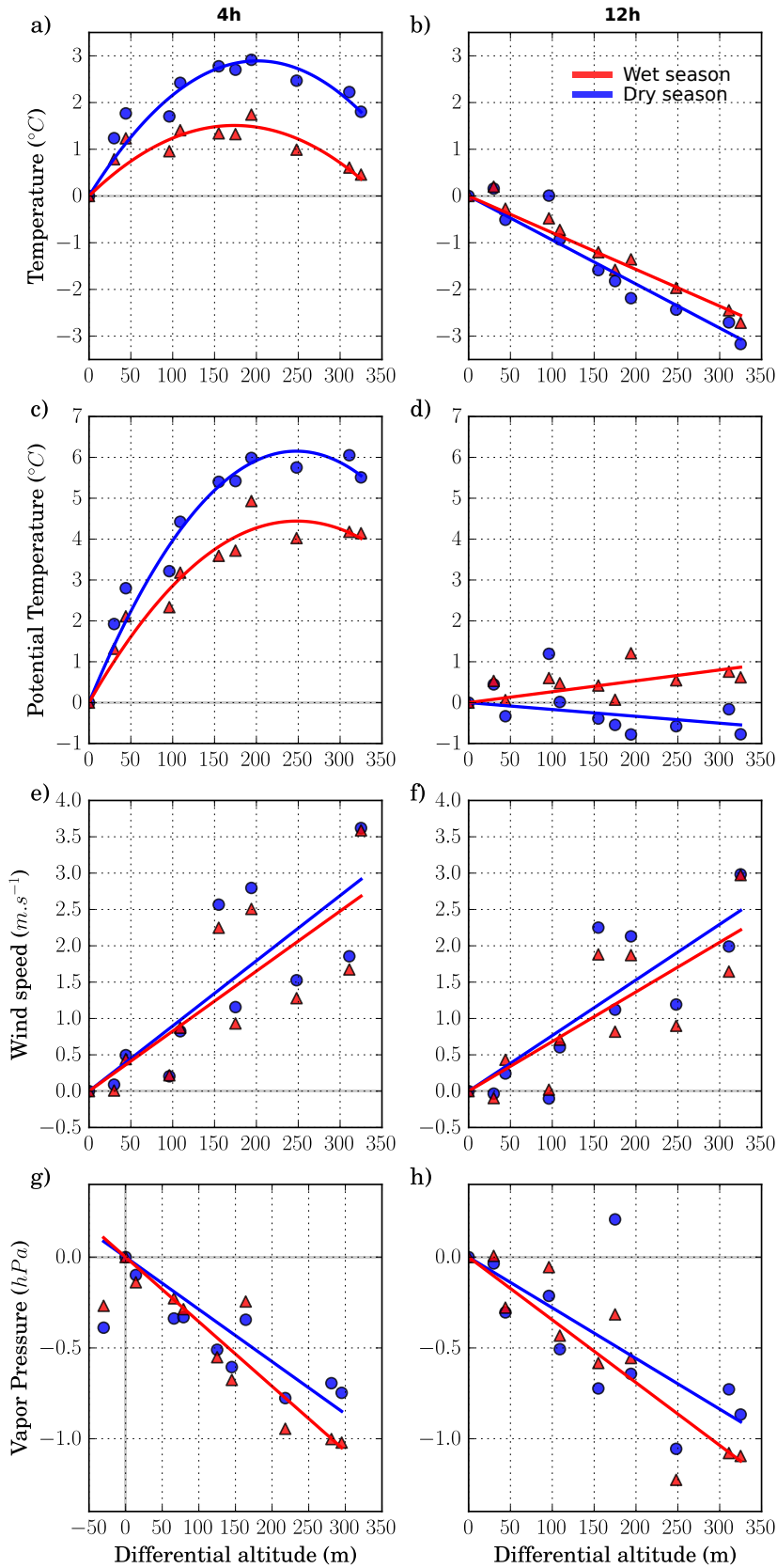
Figure 3.7: Altitudinal variation at the upper catchment of (a,b) air temperature (°C), (c,d) potential temperature (°C), (e,f) wind speed ($m.s^{-1}$) and (g,h) water vapour pressure (hPa), calculated as the mean deviation of a station minus the station S7 (in the valler center) and varying with the differential altitude of the stations (abscissa).Averages were calculated at 4h (left pannels) and 12h (righ pannels), during the dry season (blue circles) and wet season (red triangles). For the vapor pressure (f), the stations S4 was used as reference. Polynomial equations were fitted for each case (coloured solid lines) and shown in Tab.3.3).

amplitude was higher in the dry season compared to the wet season (solid lines in Fig. 3.8.a). The daytime temperature TLR was in general higher than the standard atmospheric lapse rate, and also above the dry adiabatic lapse rate, specially in the dry season (see comparisons in Fig. 3.8.a).

We associated the seasonal differences of temperature TLR with a number of processes. At daytime, higher energy surplus in wet season (relatively to the dry season) is about to help atmospheric mixing within the slopes and so reduces diurnal TLR. Higher nocturnal radiative deficit in dry season can help increasing the overall cooling in the basis, but with possible emphasys at the bottom valley where air was drier than above the slopes at night. Meanwhile, other thermodynamical forcings should partly explain the seasonality. Nocturnal downwinds are supposed to drain cold air from above and thus cool the valley. Another forcing is the effect of mechanical turbulence and cloudiness at night. We noted exceptionally a range of nocturnal negative TLR, that was often associated with the lowest CSF range and wind speed below 5 $m.s^{-1}$, that is, cloudy and relatively calm nights (see blue circles in Fig. 3.9.a; nocturnal CSF was approximated to the previous daytime hours); also for wind speed above a threshold of $\approx$ 5 $m.s^{-1}$ (dashed line in Fig. 3.9.a) the TLR was always negative, what seems associated to strong vertical mixing in the valley´s atmosphere that apparently did not depend on cloudiness.

The temperature TLR on the west side was in general more intense than in the east side (solid and dashed lines in Fig. 3.8.a), that is, the west slope showed a slightly higher nocturnal warming with altitude, and similarly a higher diurnal cooling with altitude, respectively. The mean differences were small and varied up to 0.2 $°C$ ($100m^{-1}$), though significant relatively and likely associated to the aspect of small hills each side and the nocturnal turbulence, similarly to drivers of the west-east air temperature deviation (Fig. 3.4.a). The mean vapor pressure decreased smoothly from the valley upwards (Figs. 3.7.g,h), which interestingly looked similar to the water vapor vertical profile often observed in tropical mixing layer. Its mean TLR varied in the range of about -0.3 to -0.5 hPa ($100m^{-1}$) (Table 3.2), and showed marked diel cycle usually small at night, that intensified along daytime and peaked just after dawn and before dusk (Fig. 3.8.b). The mean ground horizontal wind speed increased with altitude (Figs. 3.7.e,f) and showed an average TLR varying
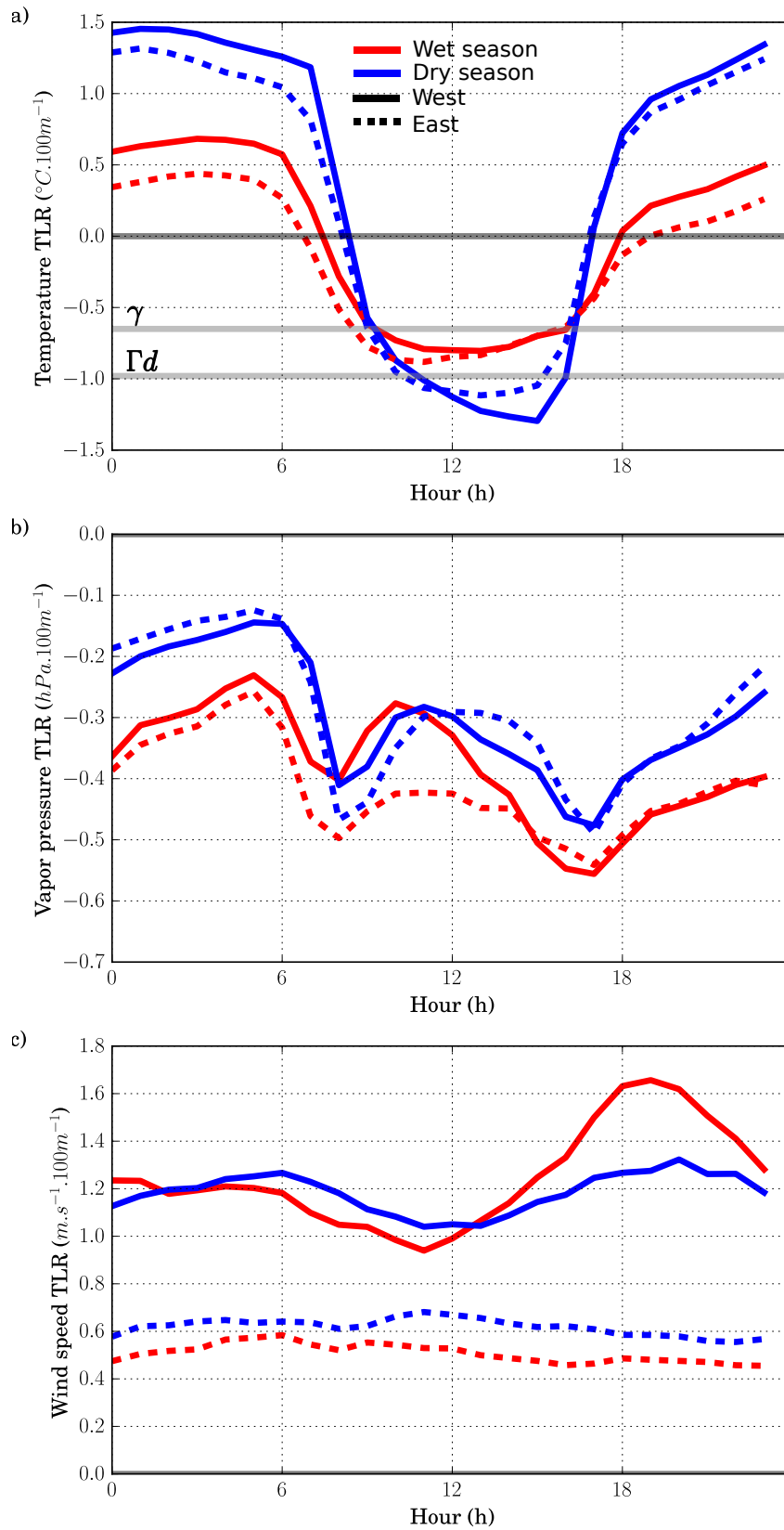
Figure 3.8: Diel cycle of the terrestrial lapse rate of (a) temperature ($°C.100m^{-1}$), (b) vapor pressure ($hPa.100m^{-1}$) and wind speed ($m.s^{-1}.100m^{-1}$) on the East (dashed line) and West (solid line) side of the upper catchment, for the dry (blue) and wet (red) season. The thick grey lines in (a) are the dry adiabatic ($\Gamma d = -0.98°C.100m^{-1}$) and the standard atmospheric lapse rates ($\gamma = -0.65°C.100m^{-1}$). The calculation of the temperature TLR did not include measurements of stations near the ridges (S1 and S11).
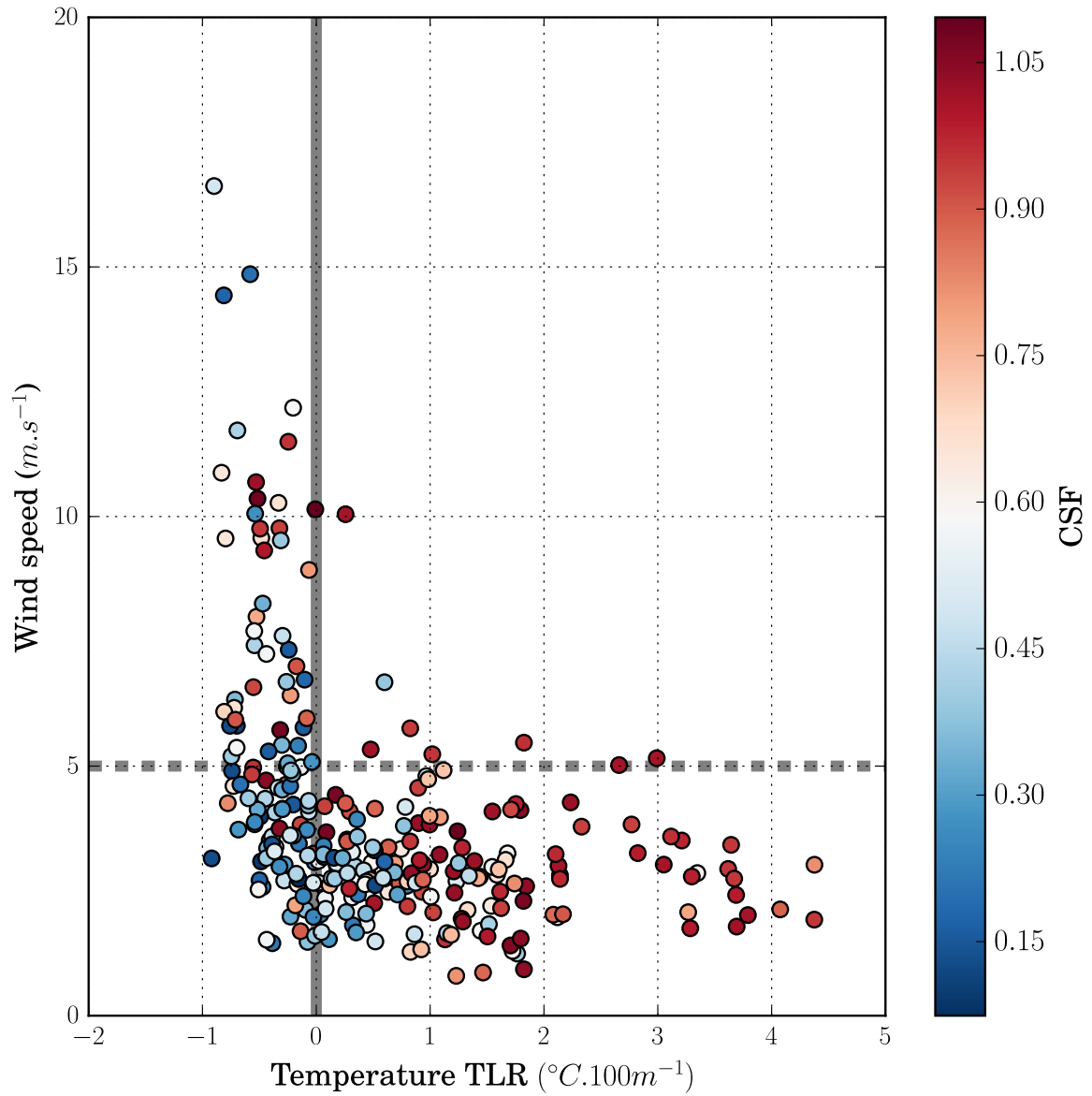
Figure 3.9: Nocturnal terrestrial lapse rate of temperature ($^{\circ}C.100m^{-1}$) measured at 4h in the upper catchment dependent of the wind speed (station S1) and the mean Clear Sky Factor calculated between 8h to 10h (color scale). The calculation of the temperature TLR did not include measurements of stations S1 and S11.

between $\approx +0.7$ to 0.9 ms^{-1} ($100m^{-1}$) (Tab. 3.2). The mean hourly TLR was however quite greater than the total average, and ranged between $\approx +0.5$ and 1.6 ms^{-1} ($100m^{-1}$) (Fig. 3.8.c). Interestingly, the east side showed wind TLR nearly half the west side (dashed and solid lines in Fig. 3.8.c), partly due to less differential exposure to the flow aloft.

We found noteworthy to point out the full range variability of hourly averages, that shows the effects of the natural weather variability on the gradients, that is not obviously detected in statistical averages as shown previously. For example, the range of air temperature deviation of the bottom valley relative to the ridge (thin solid lines in Fig. 3.10.a) was about 15°C. At night the measurements were as low as 10 °C colder at the bottom, and about 5°C warmer at daytime, that overall indicated much stronger gradients than the mean TLR (grey dashed and solid curves in Fig. 3.10.a). For hourly deviations of vapor pressure the bottom valey was up to about 4 hPa wetter at day than the ridge, and down to about 2 hPa drier at night, that both shifted much beyond the mean TLR (Fig. 3.10.b). For the wind speed, the hourly averages at the bottom valey were up to 6 ms^{-1} higher than in the ridge, that were in generally well above the mean TLR (grey curve in Fig. 3.10.b). Notwithstanding, we noted substantial occurrence of small deviations below the mean TLR, that were likely associated to weak synoptic flow. The inspection of upwind/downwind circulation with the current measurements (in Fig. 3.6) suggested the organization of cell like branches to exist along the cross-valley transect at the upper catchment, that would lead to surface mass divergence/convergence centred at at the valley likely to be investigated. We calculated a mean hourly spatial terrestrial wind divergence index (TWD) to provide starting point to the investigation, and noted how it showed a smooth mean diel pattern (Fig. 3.11.a) even embedded with some spread year round. The term was in general positive at daytime (divergence from the valley) and negative at nighttime (convergence to the valley). The onset of divergent TWD appeared slightly after dawn, and so the convergent after about 15 h. Interestingly, the divergent TWD grew synchronously to solar radiation and was less sensitive to seasonality, whereas the convergent TWD was apparently steady thru the night and stronger in the dry season. The index seemed helpful to show the prevailing flow direction integrated over both the slopes in the valley, to figure simple quantification of upslope/downslope circulation day round. It is however simple and does not clear specific spatial solution dependent on the

positioning at the transect, so does not quantify mass divergence strictly.

The previous patterns of TWD and temperature TLR raised the question of how these variables could be evaluated together using the current approach. The dispersion between mean hourly TWD and mean hourly temperature TLR showed two ways of dependence, which we identified in distinct graphical parts or loops (Fig. 3.11.b). Firstly we noted an increasing divergence (sequential red hours in Fig. 3.11.b) revealed soon after dawn that peaked at about 11h. In this part the divergence increased from an initial negative TLR thru an evolving positive TLR, in a roughly linear relationship. This part suggested a pattern where strictly downwind/positive TLR coexisted, as well as upwind/negative TLR.
Secondly we separated a loop of increasing convergence right after noon (sequential blue hours in Fig. 3.11.b). From about 16h thru dusk we noted the onset and increasing convergence (or downwind) with weakening TLR (though still negative), when it seems uncertain if such downwind evolves partly from the synoptic flow peaking at this time (see Fig. 3.2.d). At night the downwind was steadily strong though rather insensitive to the increasingly positive TLR. In general this loop suggested a nocturnal regime when strong/steady downwind depends on the increasingly positive TLR, although they do not seem to be clearly proportional.

We attempted to detail the likely effects of cloudiness in the differential warming and wind, using specially the measurements at daytime hours when CSF was properly calculated. With conditions of cloudy sky the valley was kept warmer than the adjacent slopes by $\approx$ +0.7 °C, thus less if compared to clear sky conditions that was above +1.5 °C in the afternoon (ΔTvs in Fig. 3.12.a). As well, the east side was warmer than the west side under cloudy sky by only $\approx$ +0.1 °C, thus much less if compared to clear sky conditions that showed differences up to +0.8 °C in the afternoon (ΔTwe in Fig. 3.12.b). The effect on the TWD appeared to be explained after the impacts on the differential warming, that is, under cloudy sky the TWD was positive at daytime although much less than with clear sky, by roughly 3 to 6 times (Fig. 3.12.d). On the perspective of the axial valley´s direction, the middle catchment was warmer than the upper catchment with cloudy sky by $\approx$ +0.3 °C, whereas under clear sky the pattern was the opposite or colder, by $\approx$ -0.3 °C in
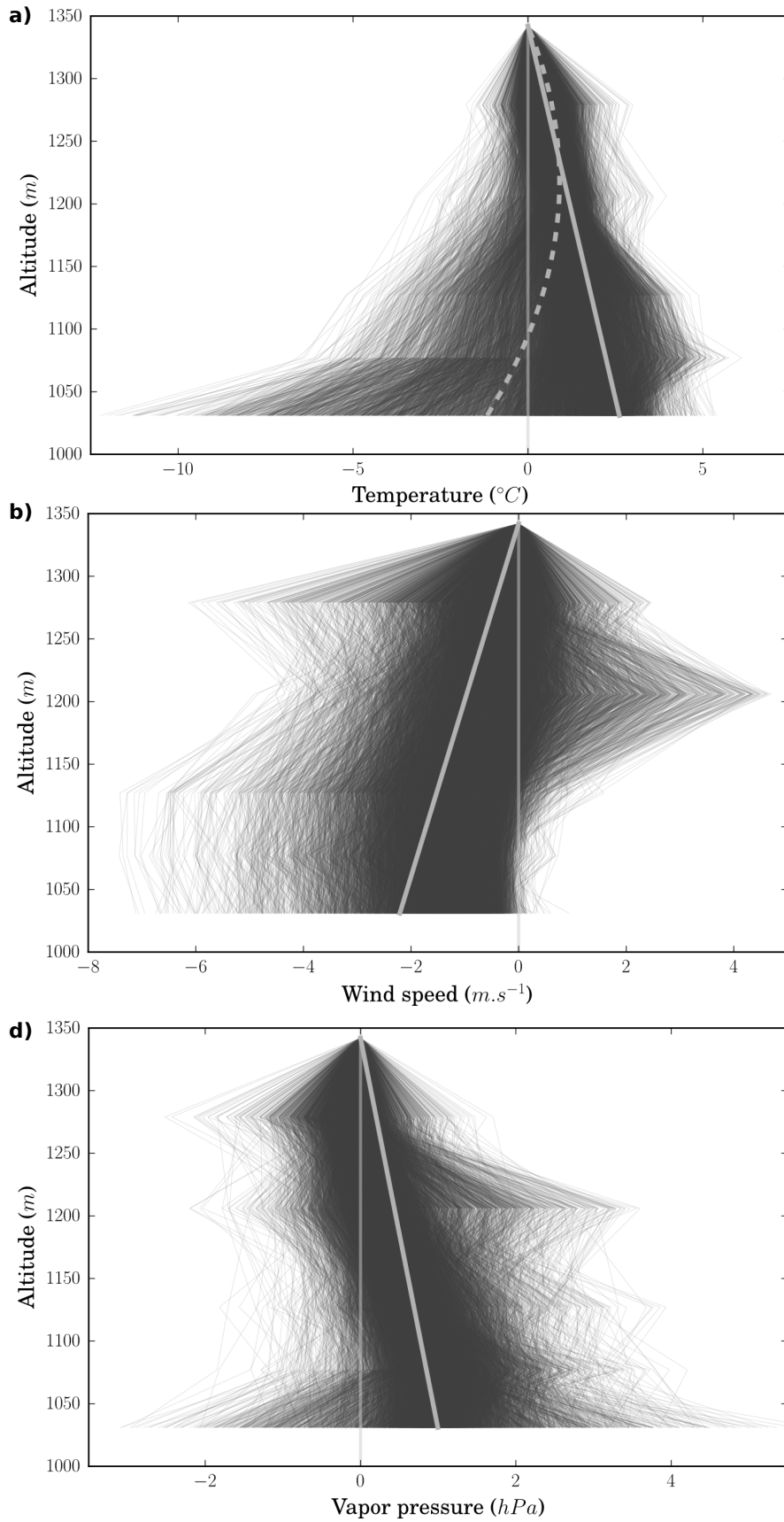
Figure 3.10: Altitudinal variation of (a) air temperature (°C), (b) vapor Pressure (hPa) and wind speed ($m.s^{-1}$) with period average profile (see Fig. 3.7) at 12h (solid) and 4h (dashed) at the Eastern side of the upper catchment.
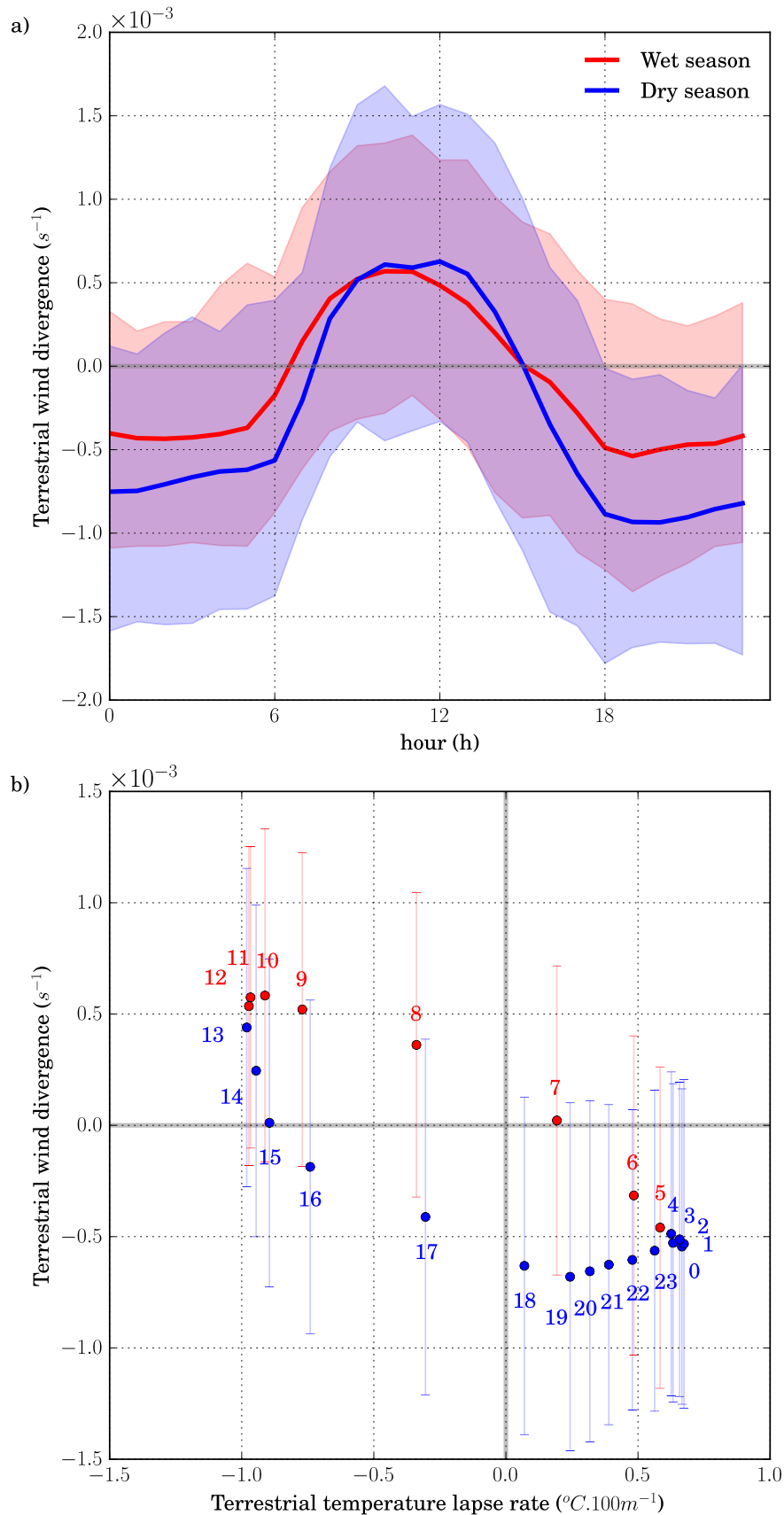
Figure 3.11: (a) Mean terrestrial wind divergence (s^{-1}) calculated on the upper catchment during the wet (red line) and dry (blue line) seasons. (b) Terrestrial wind divergence (s^{-1}) and temperature lapse rate ($^{o}C.100m^{-1}$). Numbers indicate the local hour and vertical bars are the standard deviation of the terrestrial wind divergence. The calculation of the temperature TLR and TWD did not include measurements of stations S1 and S11.
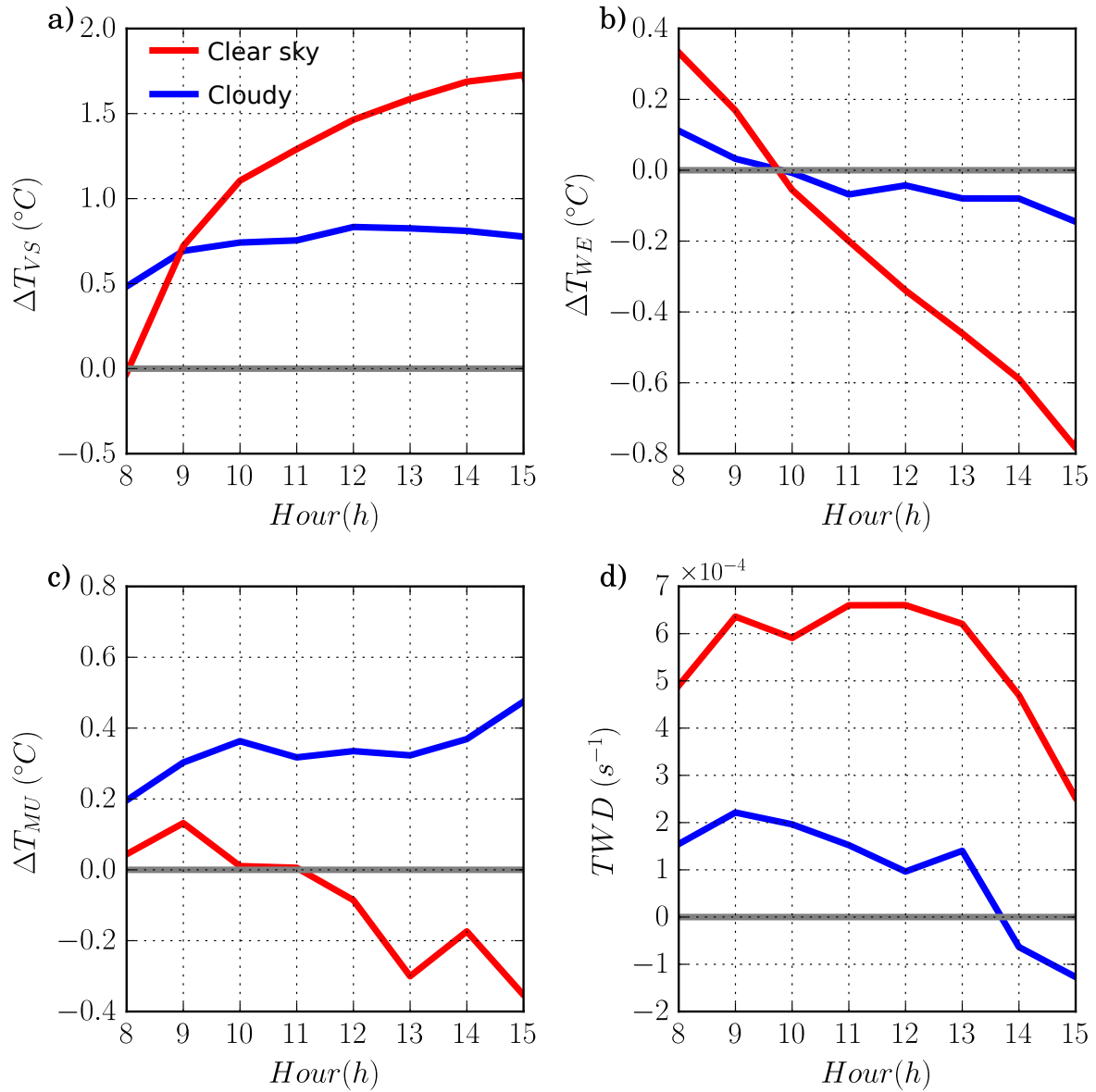
Figure 3.12: Difference of temperature (ΔT) between the valley/slope (a), West/East (b) and middle/upper catchment (c), terrestrial wind divergence (d), all under cloudy sky (blue line) and clear sky (red line) condition.

the afternoon (ΔTmu in Fig. 3.11.c). This pattern is in good agreement with the previous discussion about the middle catchment being relatively warmer at daytime, specially for the wet season or when more cloudiness is available. In general cloudiness has weakened the mean differential warming and the secondary circulation between valley and slopes.

3.2   Climate downscaling at meso-γ scale

We show the spatial and temporal representation of the PC modes associated to the ground atmospheric hourly measurements, hereafter referred to as T (air temperature), q (specific humidity), u and v (zonal and meridional wind speed) . We also discuss how GCM and topographic predictors were useful to help modelling the main PC modes in order to produce statistically-based extrapolations over the basin.

3.2.1   Modes of temperature and humidity

The T and q PCA showed 4 and 2 main modes that explained >99% of the variance, respectively, although they were largely dominated by PC1 with 93% for T and 98% for q (Tab.3.4). The PC1 for both variables showed loadings with the same sign for all stations and so the altitude (Figs. 2.4.a,b). We noted how the absolute T loadings decreased with height up to about 1100m, which corresponded approximately to the nocturnal thermal belt level (see section 3.1). The q loadings showed only a slight variation with altitude. For the remaining PCs, the loadings were alternatively negative and positive (Figs. 2.4), where the PC2 incidentally reversed sign approximately at the thermal belt level, for both temperature and humidity.

The T and q PC1 scores were of the same sign for both variables, that combined with their respective loadings gave a single positive time series. The T and q PC1 scores showed clearly the control of the diel variability with the maximum in early afternoon (grey lines in Figs. 3.13.a,b) and the seasonal variability with minimum in winter (Figs. 3.14.a,b), corroborated by field descriptions (see section 3.1). Likewise the T PC2 scores were negative, so the reconstructed temperature was colder in the valley, especially at night (Figs. 3.14.e; 3.13.e), with recurrent greater magnitudes in winter (Fig. 3.14.e), that seems to be associated with the nocturnal cold pools near the bottom valley (see section 3.1). We noted that T PC2 scores is nearly zero at some events (Fig. 3.14.e), possibly associated to the valley warmer than the slope, or superadiabatic terrestrial lapse rate.

The positive q PC1 scores (Fig. 3.13.b) combined to the positive loadings, that in all indicates that it decreases with height (Fig. 2.4.b). The q PC2 combined scores positive

Variables	Explained Variance (%)				
	PC1	PC2	PC3	PC4	**Total**
Temperature	93	6	< 1	< 1	99
Specific Humidity	98	< 1			99
Zonal wind	44	35			79
Meridional wind	84	7.5	3		95

Table 3.4 - Variance explained by the different PCs retained for the temperature, specific humidity, zonal wind and meridional wind datasets.
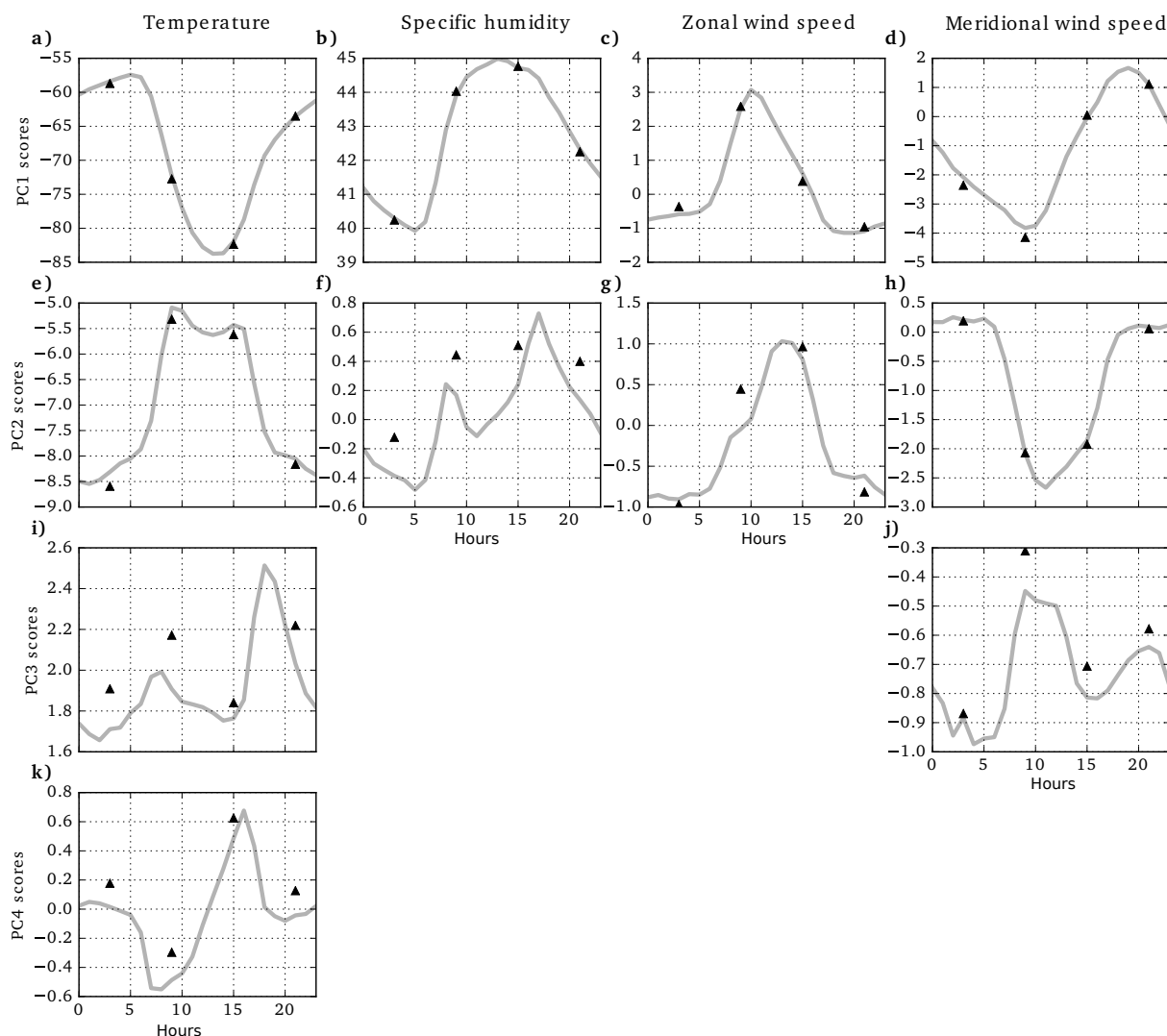
Figure 3.13: Daily cycle of temperature (a,e,i,k), specific humidity (b,f) and zonal wind (c,g) and meridional wind (d,h,j) PCs scores for the 6-hourly test period datasets used in this modelling methodology (black triangle) and for the hourly datasets (grey lines).
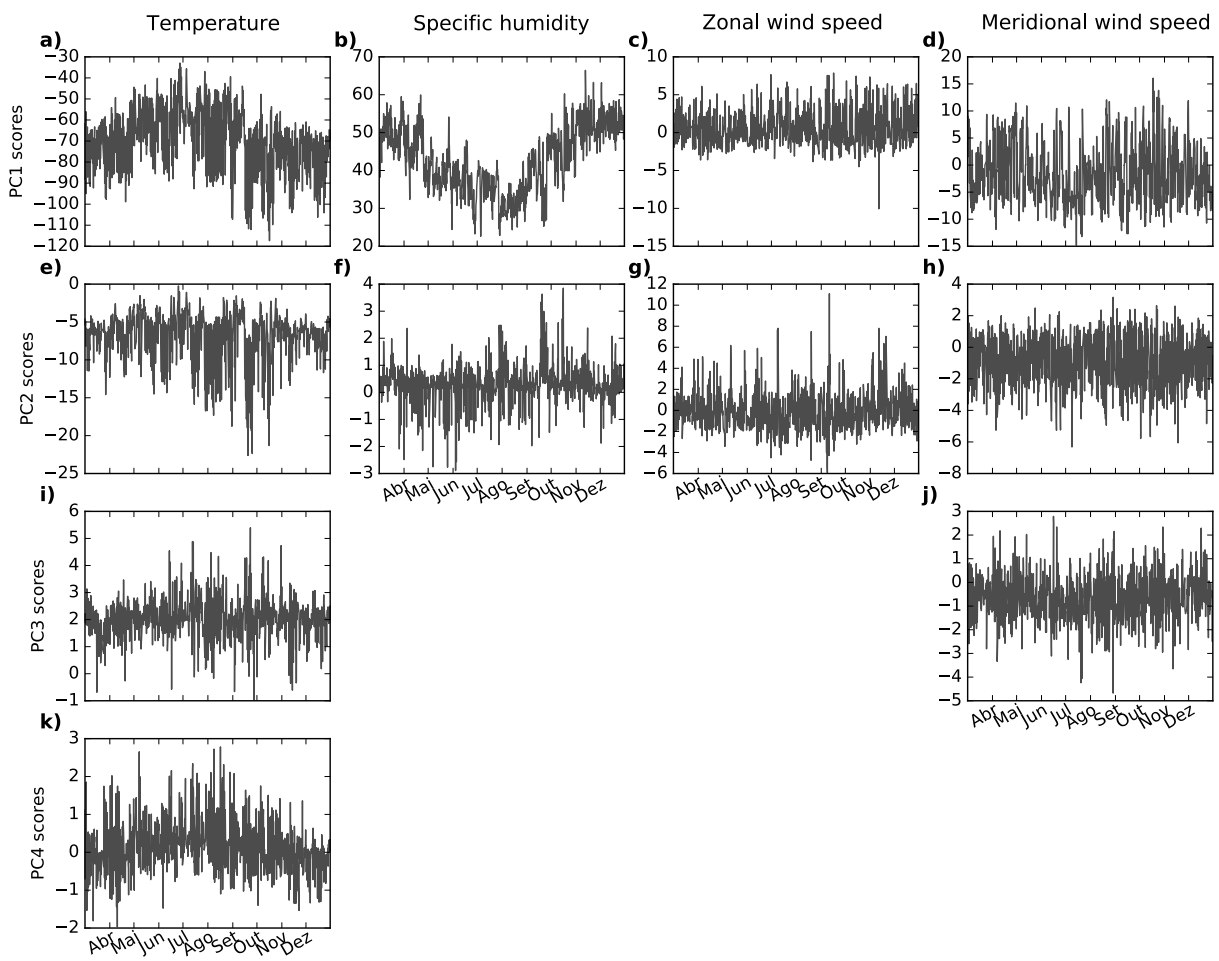
Figure 3.14: PCs scores for temperature (a,e,i,k), specific humidity (b,f) and zonal (c,g) and meridional wind (d,h,j).

at day and negative at night (Fig. 3.13.f) with loadings positive at higher elevation and negative at lower elevations (Figs. 2.4.f), so its contribution is on increasing wetting with height at daytime, and drying at night, with no obvious seasonality (Fig. 3.14.f).

The T PC3 and PC4 captured respectively a transitional altitudinal pattern and the cross-valley gradient. The T PC3 scores were mostly positive (Fig. 3.14.i) and showed higher magnitude after after dusk (Fig. 3.13.i). The T PC3 loadings were positive near the valley center and near the ridge, and negative at the mid-slope (Fig. 2.4.i), as represented by two varying modes with altitude, one from valley to mid-slope and another from mid-slope to the top. This mode captured the day to nighttime transition, with stable layer start forming at the botton valley. The T PC4 loadings showed roughly a linear relationship with the cross-valley position (Fig. 3.13.k) and appeared especially at dawn and before dusk (Fig. 3.13.k).

The Table 2.3 shows which topographic predictors were used to fit the PCs loading models, respectively, for each separate atmospheric climatic variable. We used these models to extrapolate the calculated loadings to the whole area of the basin. The Table 3.5 shows the GCM predictors used to fit the PCs score models, respectively, for each separate atmospheric climatic variable. We used these models to estimate the scores at specific hours for the 2015 period from the GCM outputs.

The T PC1 scores showed high correlation with temperature at 900 mb, a significant correlation with upward longwave radiation, and a small though significant correlation with the vertical gradient of relative humidty. The T PC2 scores showed significant correlation with the vertical temperature gradients and less with the meridional gradient of temperature. Both T and q PC1 scores were strongly correlated with the GFS temperature at 900mb and specific humidity at 2m respectively, that alone have explained the larger fractions of the final model correlation score. The T PC4 scores showed only a small correlation with the sensible heat flux, and other predictors as horizontal gradients of temperature, that are expected to be maximum at the same time. The T PC3 scores had weak correlation, but we decided to use the selected predictors possibly associated with the vertical wind speed shear, concurrent with the surface atmospheric decoupling

PCs	Stepwise position	Temperature R^2	Temperature predictors	Specific humidity R^2	Specific humidity predictors	Zonal wind R^2	Zonal wind predictors	Meridional wind R^2	Meridional wind predictors
	1	0.85	T_{900mb}	0.82	Q_{2m}	0.36	V_{900mb}	0.69	V_{900mb}
	2	0.69	$L_{emitted}$	0.28	$L_{emitted}$	0.31	Rn	0.54	$\Delta_y T_{850mb}$
PC1	3	0.13	$\Delta_{500-900mb}Rh$	0.57	Q_{soil}	0.14	$\Delta_{850-900mb}T$		
	Total	**0.88**		**0.85**		**0.60**		**0.73**	
	1	0.41	$\Delta_{900mb-80m}T$	0.12	Rh_{900mb}	0.25	U_{900mb}	0.44	$\Delta_{850-900mb}T$
	2	.	T_{2m}	.	$L_{incident}$	0.21	$\Delta_{850-900mb}T$	0.29	$\Delta_x T_{900mb}$
PC2	3	.	$\Delta_y T_{850mb}$	.	Q_{2m}	.	$\Delta_x T_{900mb}$	.	$\Delta_{850-900mb}U$
	4	.	$L_{emitted}$					.	$\Delta_y V_{850mb}$
	Total	**0.67**		**0.20**		**0.35**		**0.52**	
	1	.	$\Delta_{2-80m}V$					.	H
	2	.	$\Delta_{2-80m}U$					.	$\Delta_{2-80m}V$
PC3	3	.	$\Delta_y V_{80m}$					.	V_{900mb}
	Total	**0.15**						**0.15**	
	1	0.14	H						
	2	.	$\Delta_x T_{900mb}$						
PC4	3	.	Q_{2m}						
	4	.	$\Delta_y T_{850mb}$						
	Total	**0.38**							

Table 3.5 - Final set of GFS predictors selected by the stepwise regression with there associated rank (col. stepwise position) and individual correlation score (R^2) for each PCs and climatic variables. The adjusted correlation score of the full model is shown in bold. The "."represent the correlation score < 0.1.

after sunset. Despite the least importance of the T PC3 and PC4, we added them in the overall model as they helped to reduce the overall MAE by $0.1°C$ or about 10%, which is likely associated to relevant physical process.

The calculated T and q PC1 loadings spatial variations distinguished clearly both the variability of cross-valley and along-valley directions (Figs. 3.15.a,b). In combination with the diel variation of the scores, they showed how they shaped the sectors as the bottom valley as warmer and wetter (Fig. 3.16 columns of T and q), especially during the day and in the wet season. The T and q PC2 captured the altitudinal variation apparently opposed to that of PC1 (Figs. 3.15e,f). At night the reconstructed T PC2 loading was higher than PC1, that emphasized the colder valley at night (Figs. 3.16.a,m) and the warmer valley at day (Figs. 3.16.e,i).
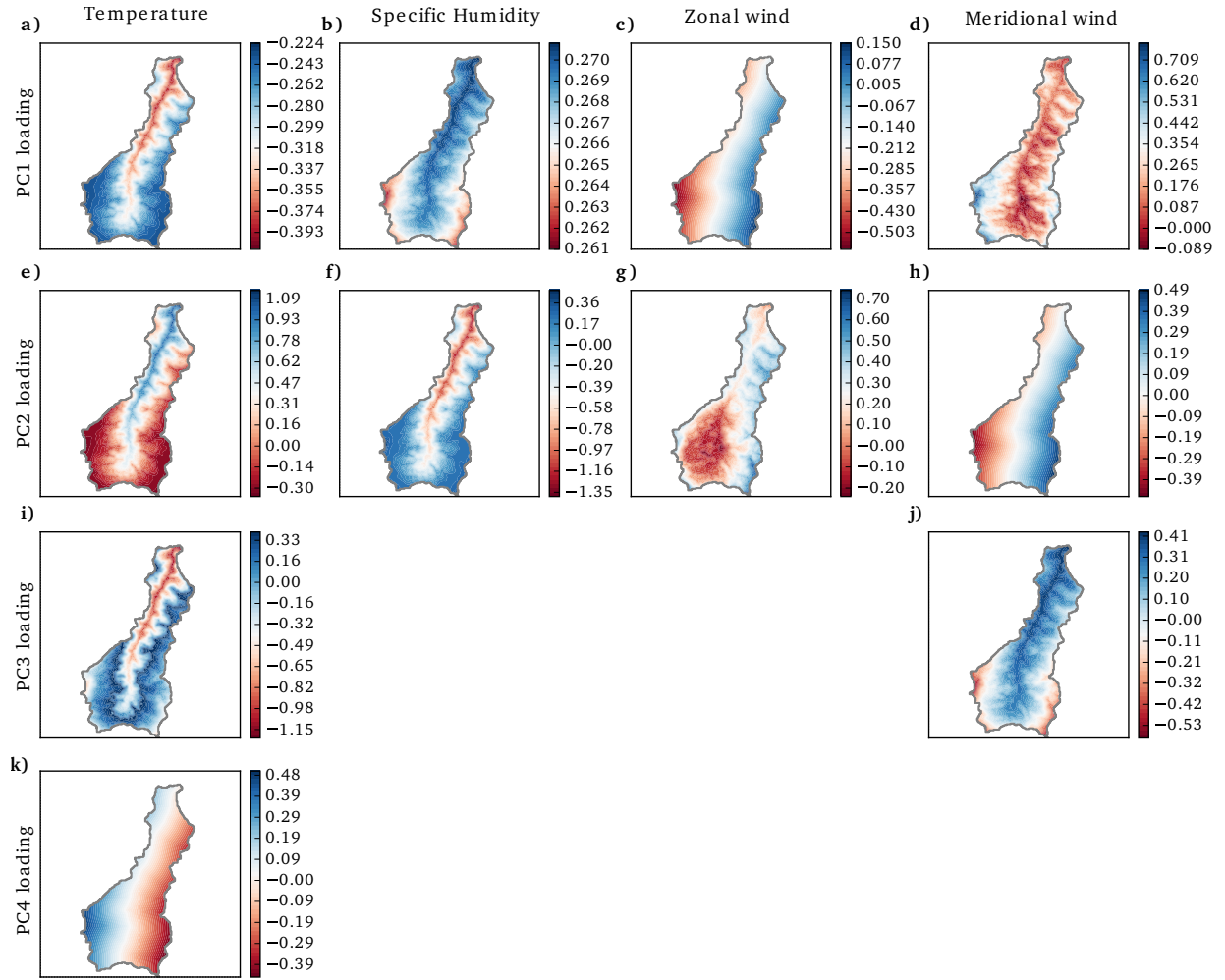
Figure 3.15: Estimated PCs loadings fields for the temperature (a,e,i,k), specific humidity (b,f) and zonal wind (c,g) and meridional wind (d,h,j).

The T PC2 and PC3 modes in general captured the controls of the topography (Figs 3.15.e,i), and so with q PC2 (Fig. 3.15.f). They have overall showed higher magnitudes under clear sky conditions and calm wind conditions, e.g.during the dry season and in post-cold front events. The T PC4 showed clearly the differential temperature between the West and East sides (Fig. 3.15.m), that is associated both to the effects of solar zenith angle in the morning and afternoon, and the differential sheltering effects (see section 3.1). We expect that under conditions of strong synoptic flow, the contributions of temperature PC2, PC3 and PC4 tend to neutralize, and PC1 becomes dominant.
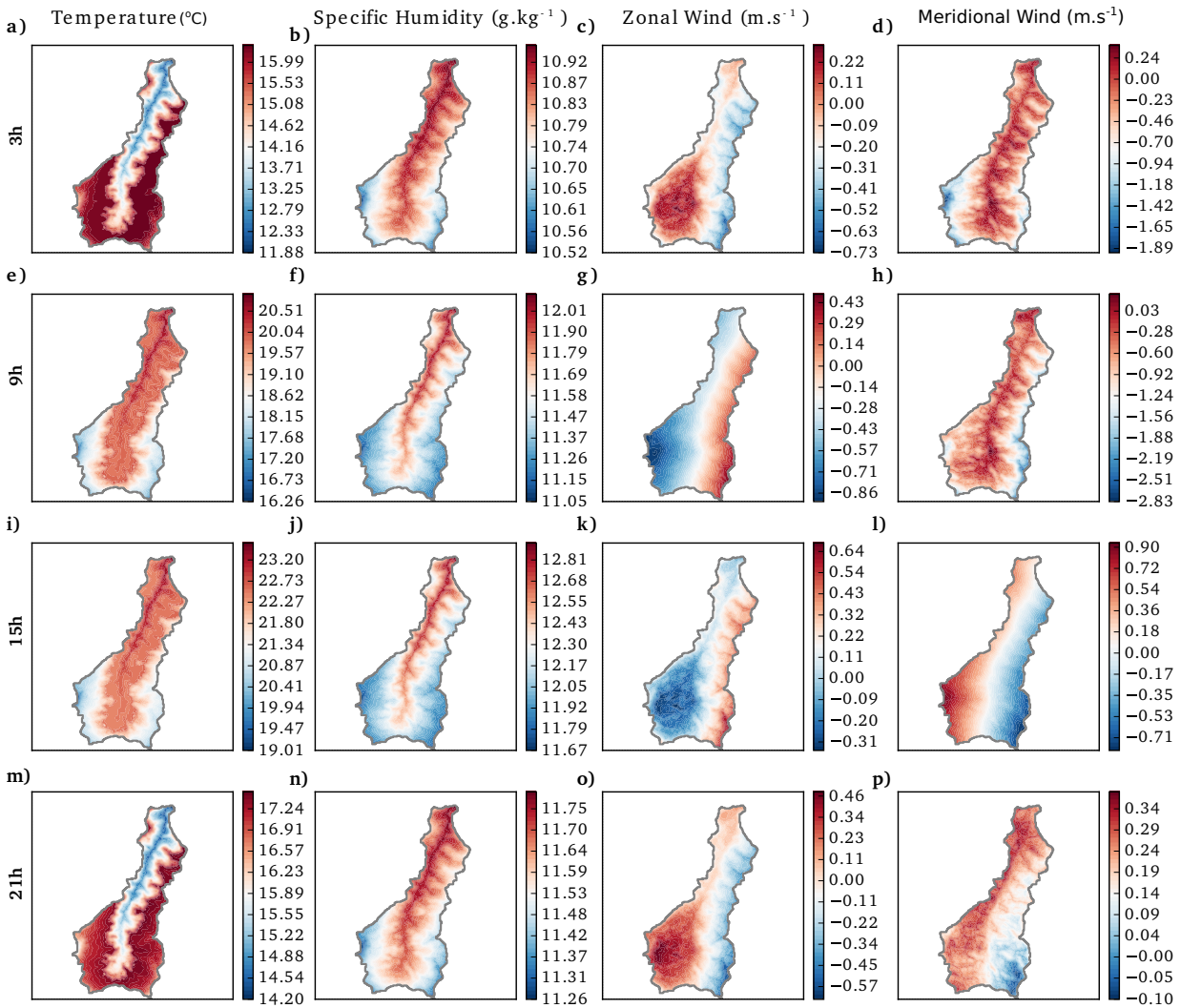
Figure 3.16: Period averaged reconstructed fields of temperature (a,e,i,m), specific humidity (b,f,j,n) and zonal wind (c,g,k,o) and meridional wind (d,h,l,p) at 3h, 9h, 15h and 21h.

3.2.2 Modes of wind speed

The wind components u and v were separated in order to anticipate their different contribution on the existing secondary circulations as described by field observations (see section 3.1), that showed distinct patterns of cross-valley and along-valley flows. For the PC1 and PC2 together, the u mode showed 79% of the explained variance and v showed 95%, respectively (Tab. 3.4).

Meridional wind

The v PC1 explained the higher variance (84%). The v loadings all showed the same sign (Fig. 2.4.d) so the meridional flow had spatially the same direction in the whole area. The v PC1 loadings were well correlated with the Topex in the North-East direction (Fig. 2.4.d), with higher values in the West side and on the upper parts of the basin, that were more exposed to the synoptic flow (Fig. 2.3.a). The v PC1 scores showed sign reversed day around, with pronounced negative values (northerly) at late night and in the morning, and weaker positive value (southerly) in the afternoon until the evening. This mode captured the control of the prevailing northesterly weak synoptic flow, and the higher southeasterly regional sea-breeze flow and eventually the post-cold front flow. The v PC1 scores showed substantial correlation (R^2=0.69) with the GFS v at 900mb, and with the meridional gradient of temperature (R^2=0.54) (Tab.2.3) that is likely associated to the sea-breeze and the cold fronts.

The v PC2 (7.5 % of the variance) captured the difference between the West and East side slopes, as showed by correlation of loadings with cross-valley distance (Fig. 2.4.g) and the well distingued spatial difference between the slopes (Fig. 3.15.h). Its diel cycle were mostly negative (Fig. 3.13.h), that peaked in the middle morning when the reconstructed v was southerly in the west side and over the basin, except in the east side where it was northerly (Fig. 3.16h). These differences explain the reversed signs that depended on the topographic features (Figs. 2.4.g,j and Fig. 3.14.h). Also, when the v PC2 is added to the PC1, it help to explain the preferential exposition of the v component on one sidewall compared to the other. The v PC2 scores were correlated with vertical gradients of wind and temperature (R^2=0.44) and less with meridional gradient of temperature (R^2=0.24).

The v PC3 explained 3% of the variance (Tab.3.4) and appeared to be related to the altitudinal variation, as suggested by the relation between the PC loadings with the altitude (Fig.3 2.4.j). This pattern had higher amplitude at night and less in the morning (Fig. 3.13.j), that the decoupling/coupling of the flow aloft could explain. Despite the v PC3 score did not show significant correlation with predictors (Tab.3.5) we kept some that could potentially be associated with the vertical gradient in the watershed.

Zonal wind

Differently of v, the u PC variance was fairly shared among the two first modes, that together explained 79% of the variance (Tab. 3.4). The spatial distribution of the u PC1 loadings were better fitted with the cross-valley distance (Fig. 2.4.d), with the predicted loadings higher in the West side (Fig. 3.14.d). Inversely, the u PC2 loadings were well correlated with the Topex in the West direction (Fig. 2.4.h) and were higher in the East side (Fig. 3.15.g). Both two modes presented a spatial divergent pattern, that appeared to represent mostly the formation of slope flows (Figs. 3.15.c,g), and partly the exposure to large scale flow at each side. Both modes varied negative and positive scores during the night and day respectively (Fig. 3.13.c,g), which agrees with the observations of downslope and upslope flows at each time. Interestingly, the u PC1 (associated to upwinds on the West side) and the u PC2 (associated to upwinds on East side) peaked at 9h and 15h, respectively (Figs. 3.13.c,g), that coincide with the maximum exposure to solar radiation each side.

The u PC1 loadings were correlated with the 900mb v wind and with the surface net radiation (Tab.3.5), the latter kept as the control to augment the thermally driven circulation, and the former associated with the more exposure to the large scale flow on the west side. The u PC2 scores showed small correlation with the u wind at 900mb (Tab.3.5). In the view of the slope flow process, both two u modes were correlated with the vertical temperature gradient. It is possible that the sligthly lower R^2 obtained for u scores when compared to v scores is caused by the secondary circulations that are not directly simulated in the atmospheric models.

3.2.3   Model assessment

The model predictions were quite reasonable to represent the main surface climatic pattern in the basin, based on the scores of temperature, specific humidity and horizontal wind speed (Fig. 3.16). We did note the detailed aspects of the main differential spatial and temporal patterns, related to the warming, wetting and the thermal driven circulations, on either the cross-valley and along-valley directions.

Metrics	Temperature	Specific Humidity	Zonal wind	Meridional wind
MAE	1.1	0.7	0.6	0.7
RMSE	1.4	0.9	0.7	0.92

Table 3.6 - Averaged MAE and RMSE of the estimated temperature, specific humidity, zonal and meridional wind.

For temperature the calculated mean absolute error (MAE) was 1.1 $°C$ and the root mean square error (RMSE) of 1.4 $°C$ (Tab.3.6), that in general showed the best performance at the sectors of the mid-slopes, when compared to the centre-valley and near the ridges, especially at night (Fig. 3.17.a). The least performance for temperature and humidity was at 15h (maximum for station S13 in Fig. 3.17), that we suggest to be attributed to the poor performance of the atmospheric models to represent clouds in mountainous region and consequently the calculated surface radiation and energy balance. For the specific humidity we assessed the MAE of 0.8 $g.kg^{-1}$ and RMSE of 0.9 $g.kg^{-1}$ (Tab.3.6), and the performance was least in the same time (at 15h) and spatial sectors atributted to the temperature (Fig. 3.17.b).

The averaged MAEs for the wind (u,v) were 0.6 and 0.7 $m.s^{-1}$ respectively (Tab.3.5). The averaged RMSEs for those were substantially different (0.7 $m.s^{-1}$ and 0.9 $m.s^{-1}$), so with a relative best performance for the zonal wind model. We noted that in general the larger errors for the wind were found on the sectors under higher exposure to the flow aloft, namely the upper slopes and the Western sidewall (see stations S2 and S3 in Figs. 3.17.c,d), compared to the relatively better performances near the centre-valley and the eastern side. In a similar fashion, lower errors for the wind were noted at night, when the mean wind flow is weaker. At some stations, especially those near the ridge (e.g. S11 and
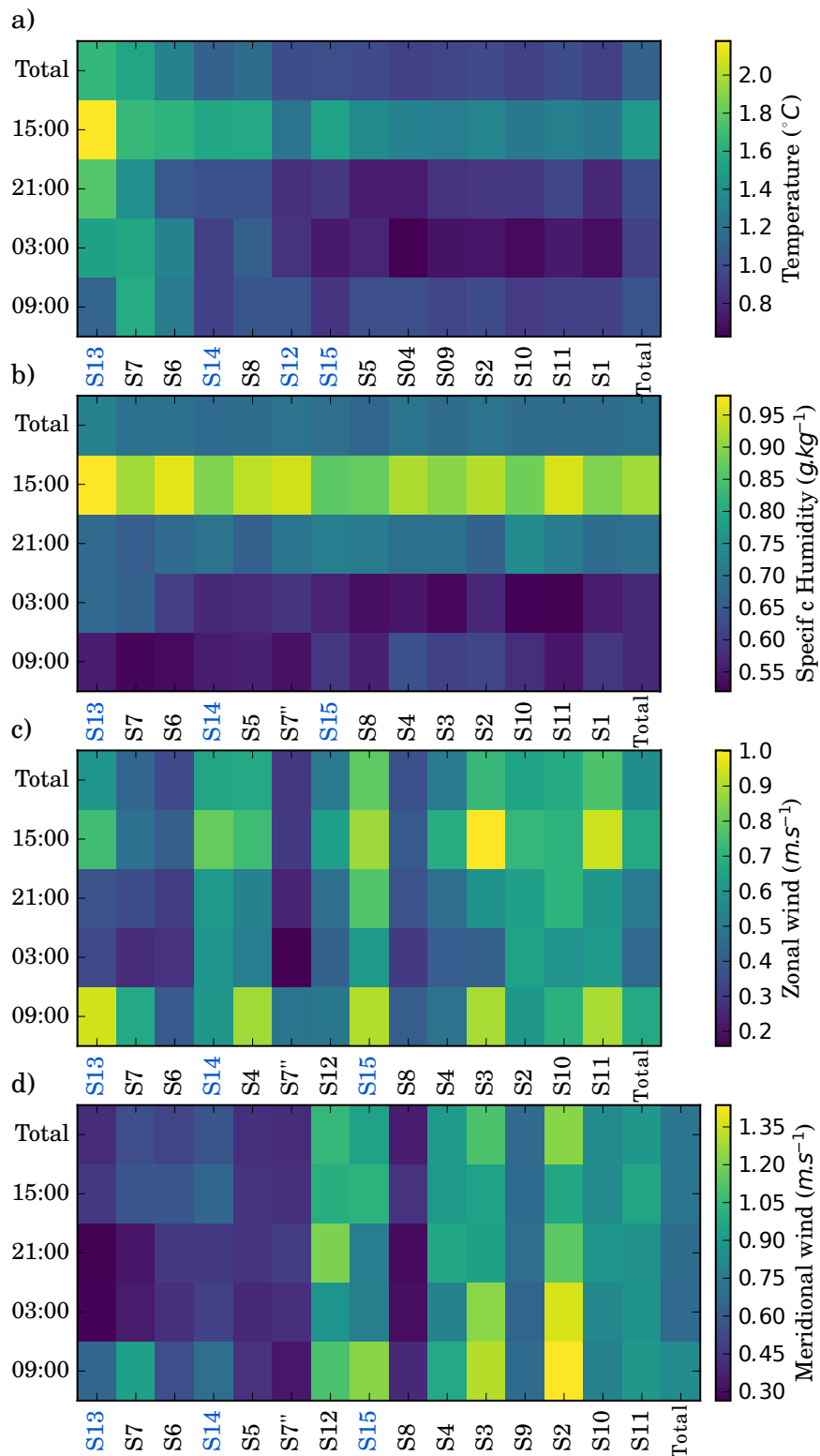
Figure 3.17: MAE calculated at the stations sorted from lower to higher altitudes for the estimated temperature (a), specific humidity (b) and zonal (c) and meridional wind (d) at 3h, 9h, 15h and 21h for the test period. Labels of the stations in the middle and upper catchment are shown in blue and black respectively.
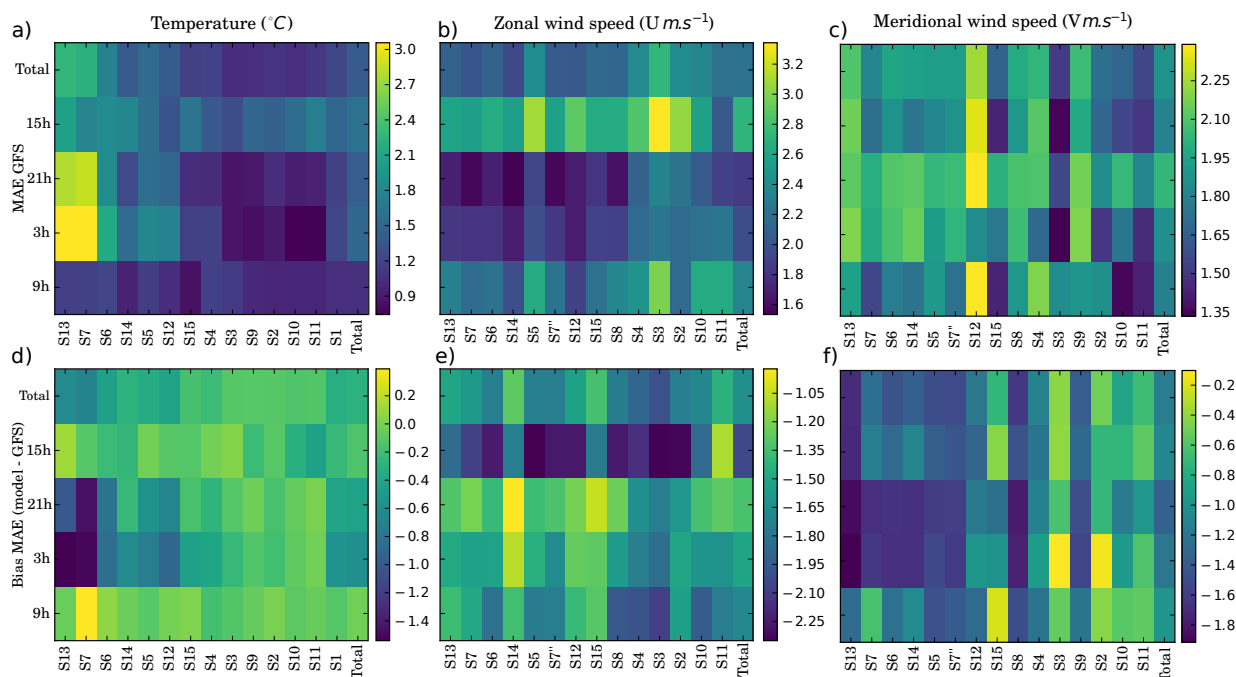
Figure 3.18: MAE of the GFS vertical interpolation, as well as its difference with the MAE of the developped models for temperature (a,d), zonal (b,e) and meridional (c,f) wind.

S12), the errors were large, that can be partly by non-linear controls of the flow near this sector.

Likewise we estimated the errors of the GFS outputs and, for the temperature, the spatial performance was less in the valley floor especially at night and, secondly in the overall temporal view the errors were larger at 15h (Fig. 3.18.a). Remarkably, our PCA-based model MAE was approximatelly 50% lower compared to the GFS. For example, the reduction in MAE was by about 1.5 $°C$ near the valley floor at the stations C10 (compare Figs. 3.17.a and 3.18.a, or direclty seen in 3.18.d). In a similar fashion, the modelled wind components MAE were roughly half (compare Figs. 3.17.b,c and 3.18.b,c, or directly in Fig. 3.18.e,f), an improvement that was particular noted at the mid-slopes in the afternoon, and in particular places, as the v wind in sheltered areas near the valley at night, and at the eastern face at daytime, for example.

3.3   Climate variability and circulation at meso-β scale based on PCA.

Three PCs were retained for temperature and humidity, that explained 79% and 83% of the variance respectively, and four PCs for the wind that summed 48% of the variance (Tab. 3.7).

	Explained Variance (%)				
Variables	PC1	PC2	PC3	PC4	**Total**
T	63	9	6		79
Q	72	6	5		83
UV	25	13	6	4	48
TUV	25	15	8	4	52
QUV	25	15	9	4	53

Table 3.7 - Variance explained by the different PCs retained for the temperature, specific humidity and wind components, as well as for the combined PCA applied at the meso-β scale.

3.3.1   Temperature modes

The first temperature mode (63% of the variance) showed the expected mass effect of the common variation among all stations, where the loadings were all positive and varied in a relatively low range (Fig. 3.19.a). The pattern was marked by the amplitude of the diel cycle (Fig. 3.19.d), with cold temperature in the middle morning (negative scores) and warm temperature up to early evening (positive scores). The area at Piracicaba and Mogi valleys generally showed higher loadings (so the daily amplitude) compared to the mountain ridges and overall in sectors parallel to the coast (Fig. 3.19.a).

The second temperature mode (9% of the variance) boldly captured a gradient perpendicular to the coast line, with positive loading close to the coast and negative at areas inland (Fig. 3.19.b). This mode showed a diel cycle variability on the scores (red line in Fig. 3.19.d), so that the reconstructed patterns with positive scores showed warmed areas inland at daytime (and cold areas at the coast) and inversely at nighttime (negative scores). It also showed a pronounced seasonality with warmer temperature at the inland regions (positive scores), especially in winter and spring season, and oppositely in the wet season (Fig. 3.19.f).
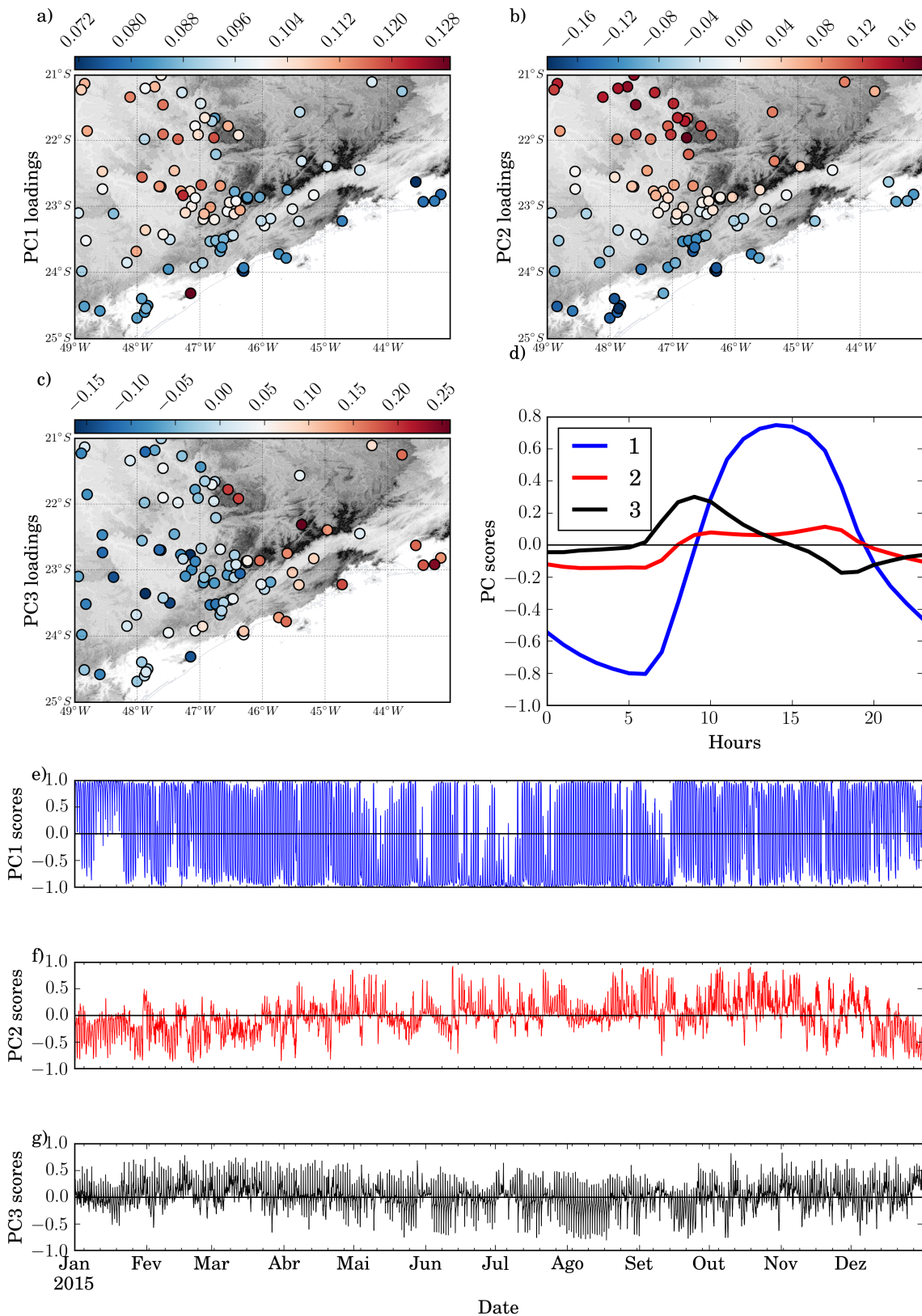
Figure 3.19: Temperature PCs loadings (a,b,c), daily average PCs scores (d) and PCs scores time series (e,f,g).
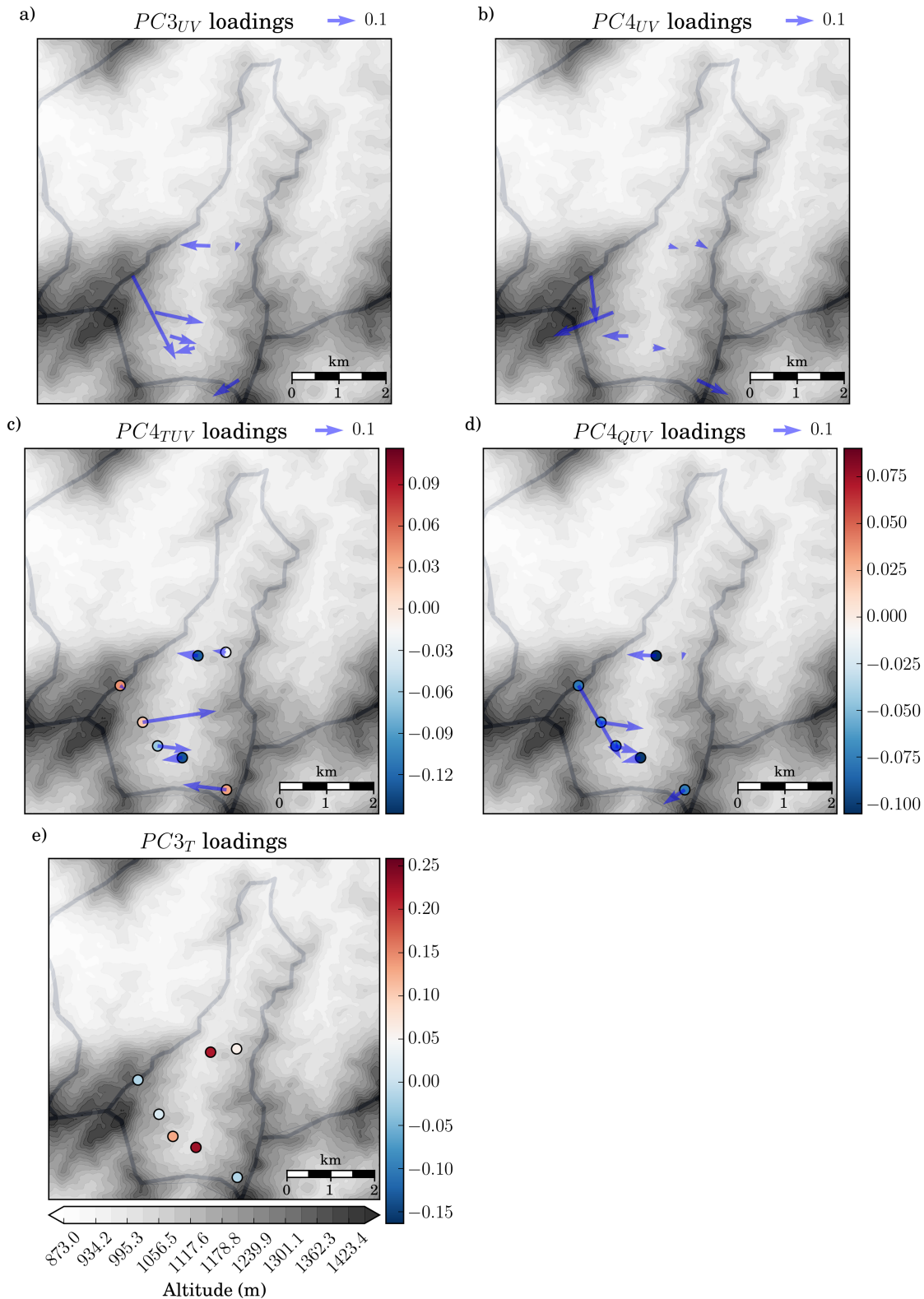
Figure 3.20: Loadings of the PC3 and PC4 wind components (a,b), PC4 combined temperature and wind component (c), PC4 combined specific humidity and wind component (d) and PC3 Temperture (e) of the 6 stations used in the Ribeirão Das Posses basin.

The third temperature mode (6% of the variance) peaked specially in the middle morning with positive scores, and at the early evening with negative scores (black line in Fig. 3.19.d). The spatial distribution of the loadings showed a pattern with a longitudinal gradient that was negative at East and positive at West (Fig. 3.19.c), as well as high positive loadings values in the valleys of the Serra Da Mantiqueira (Fig. 3.20.e). It apparently captured the longitudinal phase shifting of the temperature due to the earth rotation, along with the rapid warming (cooling) in the valleys of mountainous region in the morning (evening). It had a weak seasonality, with lower negative scores in the dry season, possibly associated to pos-frontal events (Fig. 3.19.g).

3.3.2 Specific humidity modes

The first humidity mode (72% of the variance) were quite similar to the first temperature mode, with all the loadings positive, that varied in a low range, and were slightly higher along the Mogi r. valley (Fig. 3.21.a). In addition, it showed a sharp seasonality, with positive scores almost exclusively in the wet season (Fig. 3.21.e) and mostly at daytime (blue line in Fig. 3.21.d), and inversely in the dry season and at late night. Based on the 1st mode, the areas inland presented a higher seasonality.

The second humidity mode (6% of the variance) captured a latitudinal gradient (Fig. 3.21.b), that was negative at South and positive at North respectively. It was positive day around in general but exceptionally negative around dusk (red line in Fig. 3.21 d), that was also more pronounced seasonally at the transitions between the wet and dry seasons (Fig. 3.21.f). The reconstruction of this 2nd mode suggested a moistening of lower latitudes in the afternoon, and inversely the rest of the day, particularly at night.

The third humidity mode (5% of the variance) captured a remarkably well defined loadings distribution that separated the elevated regions at the mountains (positive values) to lower regions in the plains (negative values) (Fig. 3.21.c), that also mixed longitudinal gradients that were marginally negative at west and positive at east. Their scores presented a strong daily cycle that were positive at day and inversely negative at night (black line in Fig. 3.21.d), that suggested an influence on the moistening of areas at mountain ranges, compared to the plains, along the day and inversely during the night. The fourth humidity
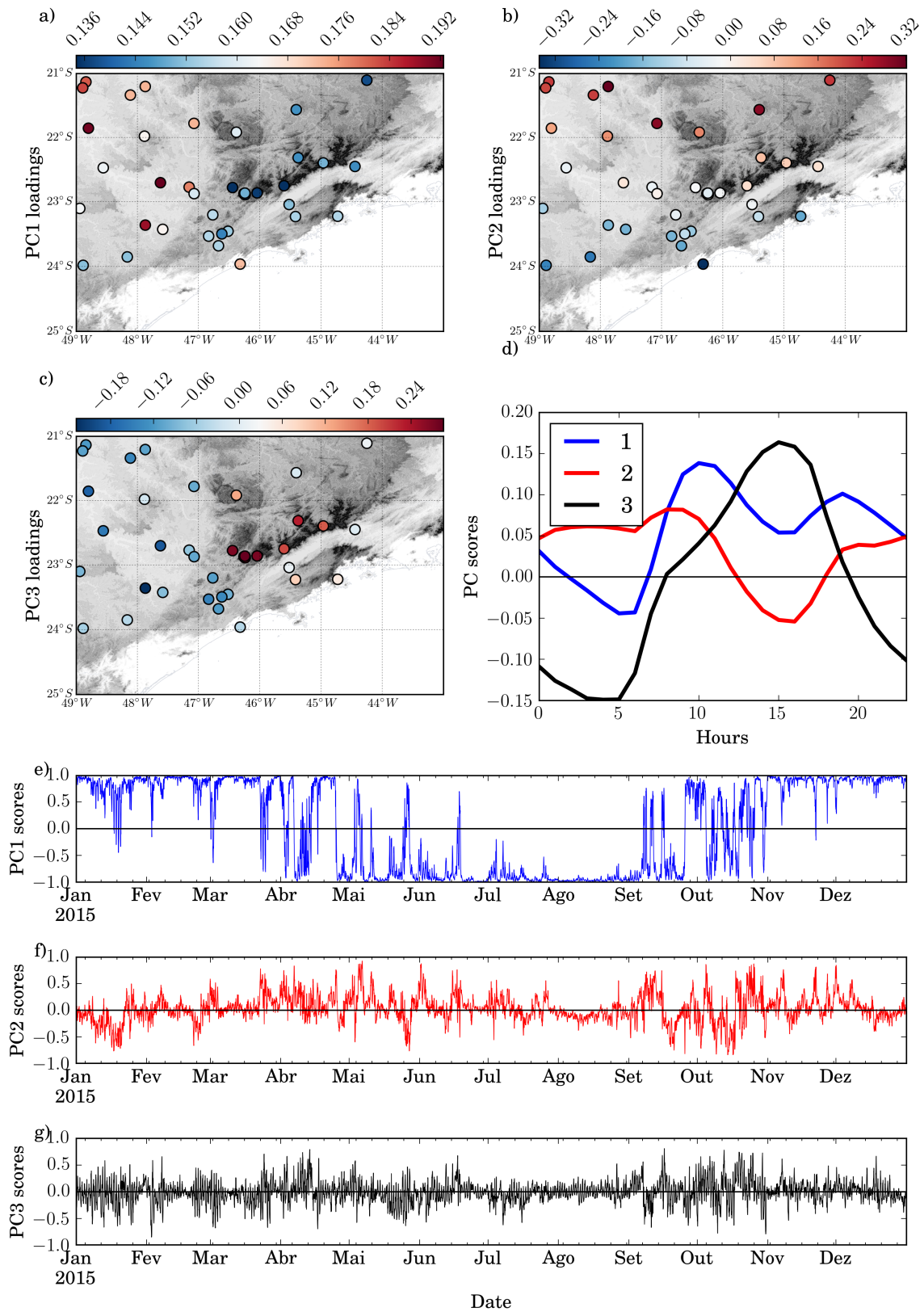
Figure 3.21: Specific humidity PCs loadings (a,b,c), daily average PCs scores (d) and PCs scores time series (e,f,g).

mode (not shown) captured somehow a similar pattern.

3.3.3   Wind modes

The daily cycle of the PC1 (25% of the variance) and PC2 (13% of the variance) scores showed both a sinusoidal-like pattern with similar amplitudes, but with a marked phase delay of roughly 6h ($\frac{1}{4}$ day), so that the PC1 score peaked when PC2 scorre was null, and v.v. (blue and red lines in Fig. 3.22.e), in a typical oscillatory pattern. Generally the PC1 scores were negative mostly in the morning, and negative at evening, with the PC2 lagged behind in time by 6h (Fig. 3.22.e). Most of the PC1 loading vectors were oriented perpendicularly the coast line towards inland (Fig. 3.22.a), and the PC2 loadings were more parallel to the coast (Fig. 3.22.b). The daily reconstructed pattern of PC1 and PC2 showed the turning wind day round (Fig. 3.23), that was Northeasterly at 12h, Westerly at 15h, Southeasterly at 21h and Easterly at 3h. The PC1 loadings were higher on the flatter areas at east (valleys of Mogi r., Piracicaba r. and Tiête r.) compared to the mountainous regions at west (Fig. 3.22.a). There are a few PC1 loadings with small magnitude, that were noted within Serra da Mantiqueira, which included Itajuba city, and at Serra do Mar, what suggests that these places most probably underestimate the wind speed.

The PC3 wind scores were generally negative at daytime with a peak at noon, and positive and nearly constant at nighttime (Fig. 3.22.e). The PC3 loadings near the coast were generally towards the sea, and differently the vectors at north were towards inland (Fig. 3.22.d). At Posses valley, the loading vectors crossed perpendicularly the level (elevation) curves, with opposite directions at the west and east slopes respectively (Fig. 3.20.a), what highlithed the upslope flow phenomena in an area of mesoscale-γ. It is likely that such processes prevail at Serra da Mantiqueira and Serra do Mar, and are embedded on the flow with the triggering sea breeze at daytime. At nighttime we suppose that there is formation of downslope flow at these spatial scales, although regionally we noted the presence of the inertial sea breeze that propagated inland (Figs. 3.23.d,e). It is more plausible that nighttime land breeze is more evidence at places near the coast, for example as the locations noted at the far eastern coast stations in the state of Rio de Janeiro (Figs 3.23.d,e), that incidentally showed a very strong inland flow at daytime that was likely associated to sea breeze (Figs. 3.23.b,c).
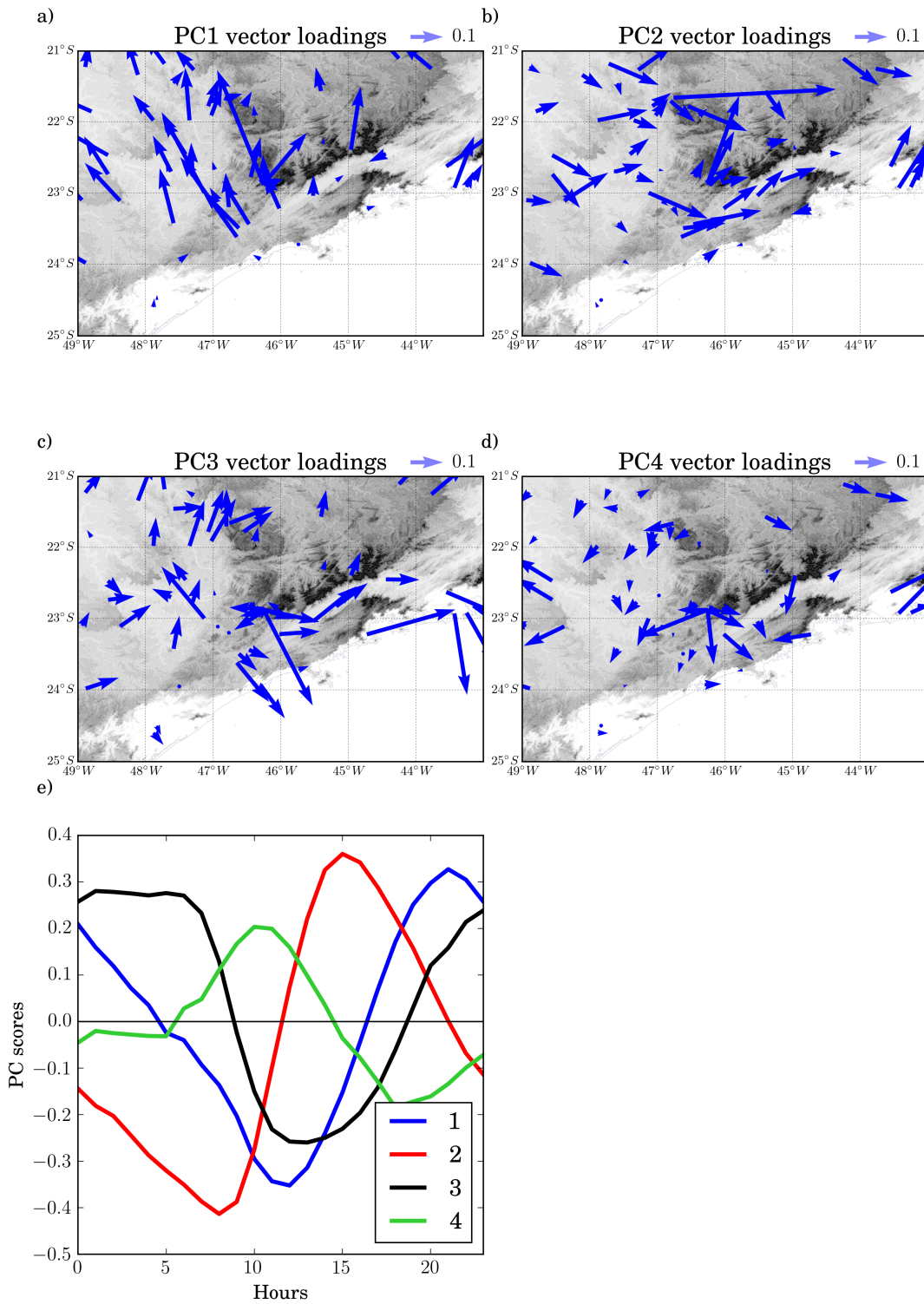
Figure 3.22: Wind components PCs loadings (a,b,c,d) and daily average PCs scores (e).

We noted how the 2nd and 3rd wind modes showed how the westerlies tended to be chanel-led thru the Paraiba r. valley and so in between the large two sierras (Fig. 3.22.b), what
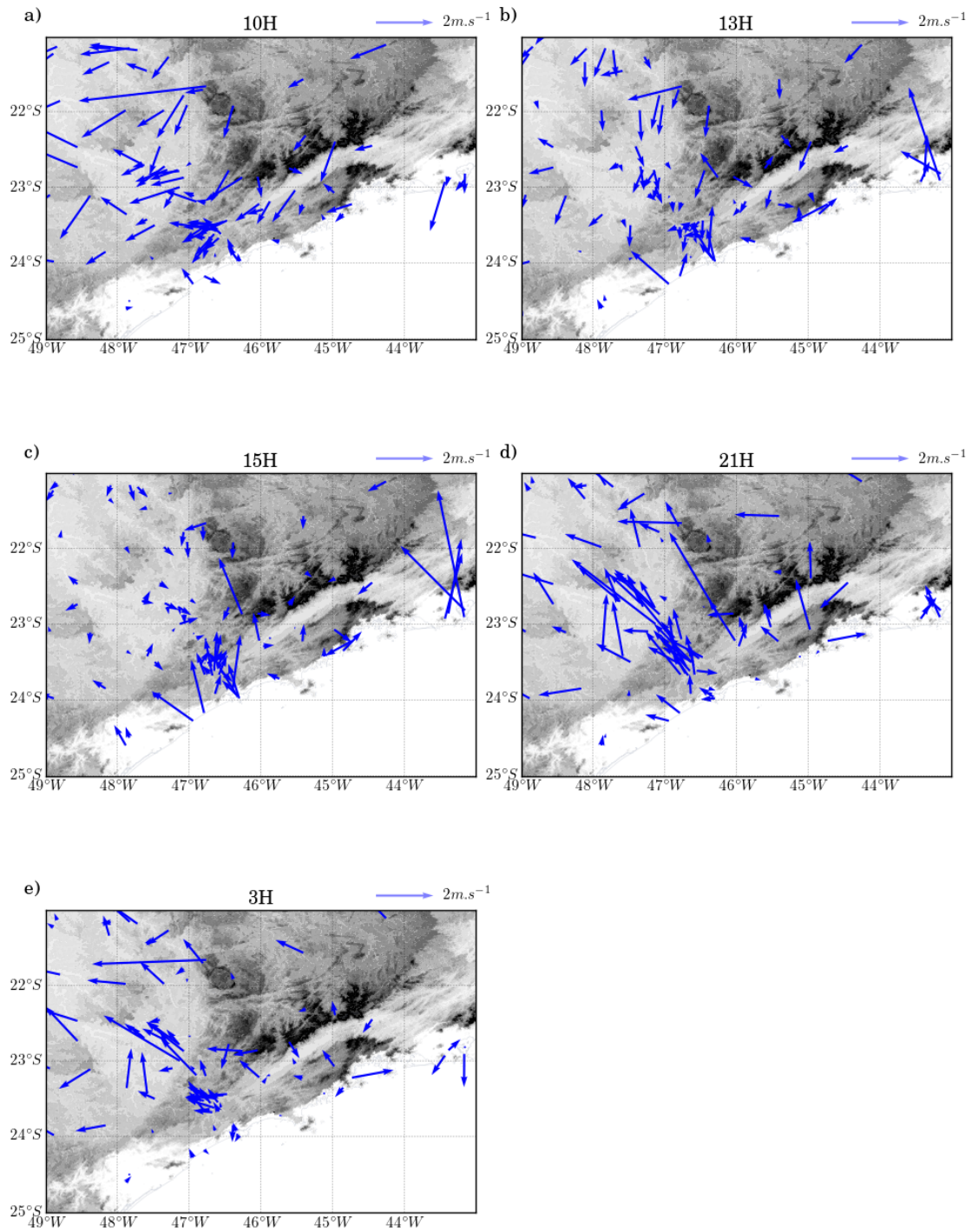
Figure 3.23: Period averaged wind at 10h (a), 13h (b), 15h (c), 21h (d) and 3h (e) for all available stations (see Tab.2.1, col.2).

remarked the influence of the topography on the regional flow propagation.

The 4th wind scores peaked just before sunrise and after sunset respectively (green in Fig. 3.22.d), with loadings that highlighted the prevailing northerly meridional flow. These loadings also showed opposite zonal components comparing the east and west sectors (Fig. 3.22.d), in addition to the slope flow in mountainous valley similarly to the 3rd mode (Fig. 3.20.b). This mode captured the lag shift of the daily cycle, with westerlies at east during the morning, and inversely before sunset. Interestingly, it showed a plain to mountain circulation between Paraiba r. valley and Serra do Mar, associated with a convergence over Serra do Mar in the morning.

3.3.4 Combined modes

Both the 4th modes of combined PCTUV and PCQUV showed loadings with similar amplitude, that suggested the intrinsic relationships among the three variables (Fig. 3.24.c,d). In both cases, the pattern of the wind loadings were roughly similar to the 3rd and 4th modes PC3UV and PC4UV (Fig. 3.22.c,d), that were likely associated with the slope flow in mountainous region (highlighted in Figs. 3.20.a,b). The 4th mode scores of PCTUV (5% of the variance) were mostly negative in the morning and positive in the evening Fig. 3.24.e), that was associated to the higher loadings (negative values) in the valley of the Serra Da Mantiqueira (Fig. 3.20.c), as well as in the eastern part (negative) of the entire domain (Fig. 3.22.a). The 4th mode scores of PCQUV were also similar to PCTUV, and were mostly negative during the day and positive at night respectively (Fig. 3.24.f), associated with the difference between the mountain ranges (negative loadings) and the surrounding plains (positive loadings) (Fig. 3.24.d), similarly to the third mode of the specific humidity (Fig. 3.21.c). The combined PCS suggested modes that indicated plausible relations between altitudinal surface temperature gradients, thermally driven mountain-valley flows and humidity convergence, all in complex terrain mountainous regions. Specifically it suggested the correlation between upslope flow and the increasing temperature in the valley at morning time, and inversely in the evening, as well as the humidity convergence of humidity over the Serra Da Mantiqueira during the day and inversely during the night.
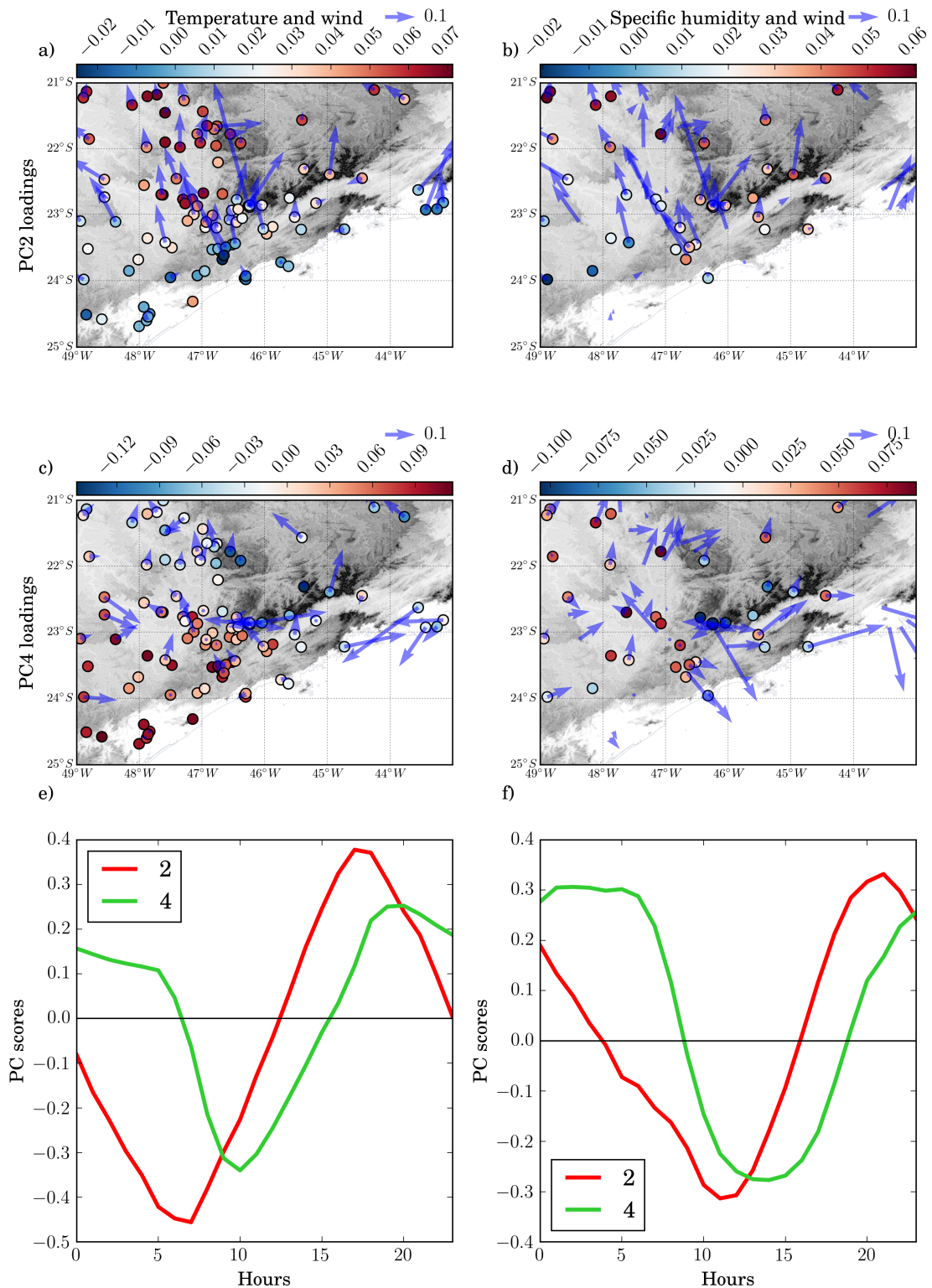
Figure 3.24: Temperature and wind components combined PC2 and PC4 loadings (a,c) and daily averaged scores (e). Specific humidity and wind components combined PC2 and PC4 loadings (b,d) and daily averaged scores (f).

The 2nd mode of both the combined PCTUV and PCQUV showed how the temperature and humidity loadings had similar magnitudes compared to the wind loadings (Fig. 3.24.a and Fig. 3.24.b), with patterns similar to the individual 2nd mode PCT and PCQ (Fig. 3.19.b and Fig. 3.21.b) and the 1st wind mode (Fig. 3.22.a), respectively. The combined PC4TUV scores peaked just before sunrise (negative) and after sunset (positive) (Fig. 3.24.e). The PC4QUV scores showed roughly the same pattern, but lagged forward by about 4h (Fig. 3.24.f), that together helped to indicate the relationship between the gradients of temperature and humidity with the cross flow on the shore line.

The motor of the sea breeze is the differential warming in the boundary layer between the land and water surface, where higher difference occurs most probably when CBL temperature is maximum day round (or about 14h), that can be suggested by the the temperature PC1. The 4th mode of PCTUV likely showed relationships of these processes and the horizontal transports of heat. It showed that increasing temperature inland and decreasing temperature near the coast were correlated with southeasterlies in the late afternoon, and inversely at sunrise. The vector loadings were higher in the central domain (Figs. 3.24.a), compared to northern part and near the coast, corresponding to the transition between the end of the early stage and the beginning of the inertial sea-land breeze propagation. Contrastingly, the loadings of the 2nd PCQUV mode were higher in the overall domain, except at the coast, that suggests how it showed a mature stage of the sea land breeze circulation (Fig. 3.24.b). This mode shows how the inertial propagation of sea breeze was associated with increasing humidity inland during the evening, and inversely during the morning.

3.3.5   Summary and conceptual model

The PC modes in general showed how the combined sea-land breeze circulation and the large scale flow dominated the wind variability, with particular control in the small mesoscale basins. The principal modes captured different phase of the sea breeze, with the 1st mode capturing the mature stage (inertial propagation) and the 3rd mode the early stage. The presence of weaker mountain valley circulation was evident but their influence was distorted by the dominant sea-breeze. We noted at higher PCs (not shown) the suggestion of convergent patterns over the mountain ranges, but with weak signal
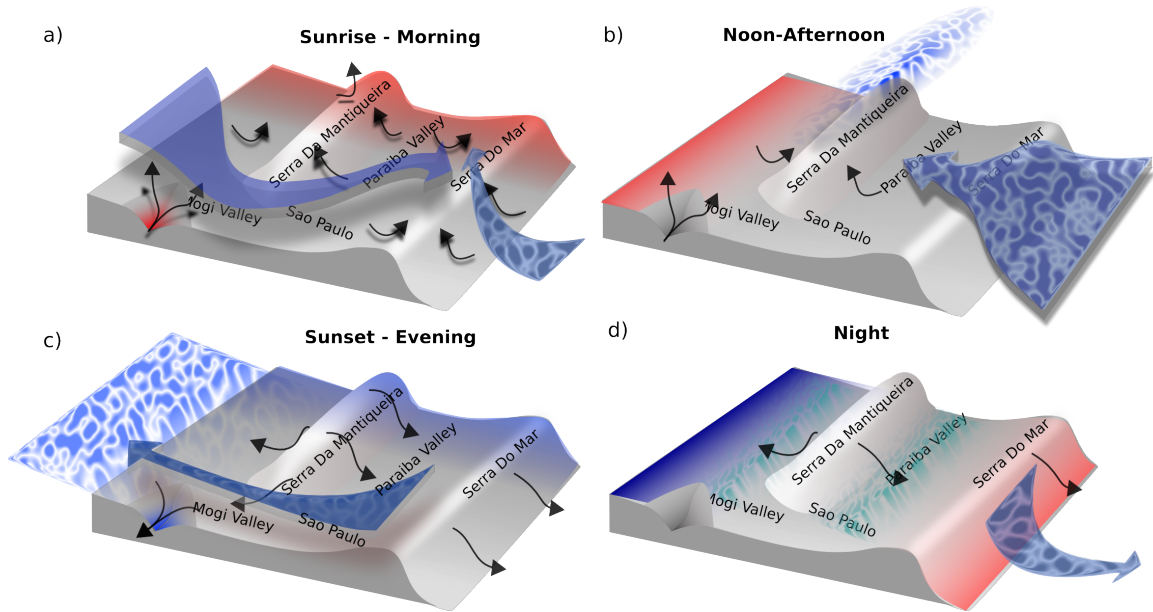
Figure 3.25: Conceptual model of the principal climatic pattern during sunrise to morning (a), noon to afternoon (b), sunset to evening (c) and night (d).

and difficult to defend. Important diel cycle pattern of the observed circulations at local and regional scales are summarized in figure 3.25. At sunrise the increasing temperature preferentially at the eastern domain was associated with local warming in the valleys of the Serra Da Mantiqueira (Fig. 3.25.a), and concurrent with synoptic north-easterlies in the overall domain (Fig. 3.23.a). Local up-slope flows were triggered at both Serra da Mantiqueira and Serra Do Mar, embedded in the growing sea breeze through the morning. At noon the wind was mostly northerly, except at the coast where the sea breeze triggered inland, that helped forming convergence areas on the plateau of the Serra Do Mar (Fig. 3.23.b). In the afternoon the southeasterlies prevailed, concurrent with dominant sea-breeze compared to the synoptic flow, that established cool and moist air transported inland, that reached the RMSP around 14h (Fig. 3.23.c). Meanwhile, the humidity at mountains ranges increased when compared to the surrounding plains (Fig. 3.25.b). In the late afternoon and near dusk, the west and north sectors were much warmer than east and south. After sunset the valleys in mountainous terrain cool quite fastly and associated with downslope flows through the night. In the evening, the coast-inland temperature gradient decreased that eventually reversed around 20h. The sea-breeze continued to propagate inland with strong southerlies noted in the overall domain at 21h, except at places quite near the shore line where downslope flows occur at some stations (Fig. 3.23.d and Fig.

3.25.c). At night, colder temperature and higher humidity are noted inland, and decreasing humidity in the mountains compared to the plains (Fig. 3.23.e, and Fig. 3.25.d).

Chapter 4

Conclusion

This study aimed to describe the surface climatic variability and the formation of thermally driven circulation in a mountainous and coastal region at southeast Brazil, both at the meso-γ and meso-β scale. Observations were obtained from ground weather stations networks installed in the region, as well as from a field experiment deployed in the complex terrain Ribeirão Das Posses basin. The principal modes of climatic variations were investigated through Principal Component Analysis at both scale. Additionally, they were modelled with GCM outputs and topographical indexes to obtain high resolution climatic fields predictions at the meso-γ scale. The main conclusions of the results presented in section 3.1, 3.2 and 3.3 are presented hereafter in the same order.

Surface climate in the Ribeirão Das Posses basin

We found evidence of substantial terrestrial climatic gradients in the cross-valley direction of the basin, where the bottom valley tended to warm/wet up at day and cool/dry down at night, compared to the surrounding slopes. The accounting of all stations over about 350m of varying altitude showed no systematic trend of the mean temperature with height, but a pronounced variability and change in the daily amplitude that decreased about 3 $°C$ with height, associated to trends in minima and maxima daily temperatures. The ground air temperature at noon decreased at a mean rate of about -0.7 $°C$ $(100m^{-1})$, so close to the standard environmental atmospheric lapse rate. It also showed high variability, with the bottom valley up to 5 $°C$ warmer relatively to the ridge at noon, what roughly extrapolates at about twice the mean terrestrial gradient. The ground nocturnal air temperature increased with height up to a maximum at about 200m, where we identified the so called thermal belt. Mean nocturnal temperature rates over the full alti-

tudinal range were very seasonal, higher in dry season of $+1.1$ $(100m^{-1})$ and less in wet season of $+0.2$ $^\circ C$ $(100m^{-1})$. Likewise, variability of nocturnal temperature gradients was strong, with the bottom valley up to $10^\circ C$ colder than the ridge at highest records. The vapor pressure decreased significantly from the valley upwards, in general below -0.5 hPa $(100m^{-1})$. The wind speed increased systematically with altitude at mean rates usually below 0.9 $m.s^{-1}$ $(100m^{-1})$, that was exceptionally higher on the west side in the early evening as above 1.6 $m.s^{-1}$ $(100m^{-1})$. The diel cycle of ground temperature with altitude showed a structure analogous to the convective mixing layer at day and the inversion layer at night with the residual layer above it. Despite the similitude it is misleading to take the terrestrial gradients for the boundary layer this way. It is expected for example, that the vertical temperature gradients away from the slope and nearly above the canopy layer, respectively, are usually stronger than the terrestrial gradients, or more stable/unstable at nocturnal/daytime conditions (Whiteman, 2000; Mahrt, 2006). We also noted significant though not too great differential warming along the valley and comparing the slope sides. The middle valley was circumstantially colder at night (mostly in dry season) and warmer at daytime (mostly in wet season), relatively to the upper catchment, under mean magnitudes below 1.0 $^\circ C$. The west slope at upper catchment was slightly warmer at night, and colder in the afternoon, at magnitudes below 0.5 $^\circ C$, where the temperature gradients were also a little stronger. In comparing the slopes we identified the control of hill's aspect at daytime, and the sheltering to flow aloft in east side. The regimes of temperature gradients transitioned remarkably fast from very negative to very positive (and v.v.) in less than 2 h, close to dawn and dusk respectively. The differential warming appeared to be well associated with upslope/downslope circulation day round. Upwinds were highlighted in the west slope, since the middle morning thru the middle afternoon, that appeared to be forced by advantaged heating in the morning, and partly to the differential warming from previous night (as opposed to the east side). In the morning until noon we found patterns suggesting how strictly downwind and positive temperature gradients coexisted, as well as upwind and negative temperature gradients. Downwinds were noted emphatically in the upper catchment (and modestly in the middle) with nocturnal regimes of steady flows that depended on increasingly positive temperature gradients along the nighttime. The temperature gradients and the thermal circulation were in general dampened by cloudiness and mechanical turbulence.

Statistical downscaling with PCA

We built a downscalling statistical model to predict high resolution surface climate on the spatial and temporal dimensions, in a complex terrain meso-γ scale basin. The method explored the Principal Component Analysis using a one year data set of ground hourly measurements of air temperature, specific humidity and wind speed on a cross-valley direction. The calculated PC modes appeared to show quite reasonably the observed daily and seasonal variability of each individual ground variable, the differential patterns of warming and wetting on the cross-valley and along-valley directions, and finally the wind variability associated to the elevation, the thermal driven circulations, the sheltered sectors and the synoptic flow. The retained PCs associated to the each variable were sufficient to explain a substantial fraction of the system variance. The PC loadings and topographic indexes were linearly correlated to produce regular grid extrapolations over the basin. The PC scores and GCM outputs were correlated to produce the daily cycle variability, and ultimately bridged coarse resolution atmospheric model to fine resolution over the entire domain. The use of new topographical indexes based on the TOPographical EXposure index helped the downscalling in our complex terrain area, that led to pronounced improvement of the estimated wind in exposed areas. Theses improved indexes are supposed to take into account the multiscale variability of wind exposure to a particular direction. In combination with other spatial predictors, such as the cross and along valley distances, the model had the benefit to represent the different wind patterns observed in the basin, that aggregated the influence of large scale flow aloft and the thermally driven slope flows. The estimated climatic fields showed good agreement with observations, as assessed by a domain and time averaged mean absolute error of about 1.1 $^\circ C$, 0.7 $g.kg^{-1}$ and 0.7 $m.s^{-1}$ for the temperature, humidity and horizontal wind speed components, respectively. It specially helped to improve on represent the influence of the landscape, concordant with better skills near the valley center. The downscalling showed less skill at 15h day around, that we associate to inaccurate calculation of cloud cover and surface energy balance from the atmospheric model. Overall the fitted model showed substantial improvement compared to estimates of vertically interpolated GFS outputs, that were nearly as double in terms of the absolute error. We noted that the selection of atmospheric model outputs as predictors for the PC scores is either a sensitive and long task. In a long list of prescribed candidates, it is not

much uncertain that the selection could alternatively pick other different terms, or even a different quantity of predictors, all for each PC mode. This is possibly an issue that clearly requires more discussion, as a way to improve the next works of the downscaling process.

Climate variability and circulation at meso-β scale based on PCA

The principal variational patterns of air temperature, humidity and wind at the meso-β scale, as well as their underlying connections were investigated with combined and correlation PCA applied on weather stations network observations. The PCA has permitted to identify gradients which separated the coast to inland areas and plains from mountainous regions, highlighting the strong control of the climatic variability by the ocean proximity and presence of major mountain range in this region. These patterns were somehow mixed with latitudinal and longitudinal gradient expected to appear day around. The modes showed that the wind variability was controlled both by the sea-land breeze circulation and large scale flow, with particular control in the valleys of mountainous regions. We identified the formation of mountain valley circulation but their weaker signal was distorted by the dominant sea-breeze. They also permitted to capture the daily wind rotation from the NE in the morning to the SE in the evening and the different phase of the sea land breeze propagation. The physiology of the landscape strongly distort the propagation of the flow where higher magnitudes where observed in the plains and in major valleys compared to the lee side of mountains. In the morning (evening), the valleys of the Serra Da Mantiqueira experienced sharp increase (decrease) of the temperature correlated with the formation of upslope (downslope) flows, while the sea (land) breeze initiated at the coast. During the day, the advection of cooler and moister air by the sea breeze, engendered significant climatic gradients perpendicular to the coast where warmer and drier area were observed inland, emphatically in the afternoon. Meanwhile, the humidity in the Serra da Mantiqueira increased in comparison to the surrounding plains, process probably associated to the formation of mountains valley flows. At sunset, despite the reversal of the thermal gradient, the sea breeze continued to propagate, carrying moister air toward the area inland through the night. The plains at the West of the Serra Da Mantiqueira experienced a higher diurnal and seasonal variation of temperature and humidity compared to the mountainous and coastal areas. Finnaly, we sketch a revised conceptual model to assimilate the learnings of the exercise into previous conceptual models (Silva Dias et

al 1995).

4.1   Final statement and Future work

This study was the first attempt to describe the surface climate spatio-temporal variability in this region, along with the application of a downscaling methodology to obtain high resolution data in complex terrain. We believe that the current downscaling can be adapted to estimate both the baseline and future climate time series from global climate model projections. The knowledge gathered from the observational, statistical and modelling aspect of this research may contribute to the development of more sophisticated methodologies to create high resolution climatic databases from local to continental scale, that would help to solve issues in hydrology, ecology and social dimension problems as in urban areas. Improvements will presumably arise from the inclusion of new temporal and spatial predictors derived from satellites products and idealised regional atmospheric model simulations. Also, better performances might be obtained using more complex non-linear models such as Neural Networks, Random Forest or Gradient Boosting Models.

Bibliography

Allen R. G., Tasumi M., Trezza R., Satellite-Based Energy Balance for Mapping Evapotranspiration with Internalized Calibration, METRIC - Model, Journal of irrigation and drainage engineering, 2007, vol. 133, p. 380

Blandford T. R., Humes K. S., Harshburger B. J., Moore B. C., Walden V. P., Hengchun Y., Seasonal and Synoptic Variations in Near-Surface Air Temperature Lapse Rates in a Mountainous Basin, Journal of Applied Meteorology and Climatology, 2008, vol. 47, p. 249

Bodine D., Klein P. M., Arms S. C., Shapiro A., Variability of Surface Air Temperature over Gently Sloped Terrain, Journal of Applied Meteorology and Climatology, 2009, vol. 48, p. 1117

Campos B. D., Reboita M. S., Carvalho V. S. B., Circulações locais induzidas pela topografia no Vale do Paraíba e na Serra da Mantiqueira: um estudo de caso para o período de 16 e 22 de agosto de 2010, Revista Brasileira de Geografia Física, 2016, vol. 03, p. 753

Chapman L., Assessing topographic exposure, Meteorological Applications, 2000, vol. 340, p. 335

Coelho C. a. S., de Oliveira C. P., Ambrizzi T., Reboita M. S., Carpenedo C. B., Campos J. L. P. S., Tomaziello A. C. N., Pampuch L. A., Custódio M. D. S., Dutra L. M. M., Da Rocha R. P., Rehbein A., The 2014 southeast Brazil austral summer drought: regional scale mechanisms and teleconnections, Climate Dynamics, 2016, vol. 46, p. 3737

Coutinho R. M., Kraenkel R. A., Prado P. I., Catastrophic Regime Shift in Water Reservoirs and São Paulo Water Supply Crisis, Plos One, 2015, vol. 10, p. e0138278

Daly C., Taylor G., Gibson W., The Prism Approach to Mapping Precipitation and Temperature, 10th AMS Conference on Applied Climatology, 1997, pp 1–4

De Rooy W. C., Kees K., A Combined Physical Statistical Approach for the Downscaling of Model Wind Speed, Weather and Forecasting, 2004, vol. 19, p. 485

Di Luzio M., Johson G. L., Daly C., Eischeid J. K., Arnold J. G., Constructing Retrospective Gridded Daily Precipitation and Temperature Datasets for the Conterminous United States, Journal of Applied Meteorology and Climatology, 2008, vol. 47, p. 475

Dixit P. N., Chen D., Effect of topography on farm-scale spatial variation in extreme temperatures in the Southern Mallee of Victoria, Australia, Theor Appl Climatol, 2011, vol. 103, p. 533

Dobrowski S. Z., Abatzoglou J. T., Greenberg J. A., Schladow S. G., How much influence does landscape-scale physiography have on air temperature in a mountain environment, Agricultural and Forest Meteorology, 2009, vol. 149, p. 1751

Durre I., Menne J. M., Gleason B. E., Houston A. G., Russel V. S., Comprehensive Automated Quality Assurance of Daily Surface Observations, Journal of Applied Meteorology and Climatology, 2010, vol. 49, p. 1615

Dussaillant A. J., Buytaert W., Meier C., Espinoza F., Hydrological regime of remote catchments with extreme gradients under accelerated change: the Baker basin in Patagonia, Hydrological Sciences Journal, 2012, vol. 57, p. 1530

Freitas E., Silva Dias P., Carvalho V., CRM R., Martins L., Martins J., Andrade M., , 2009 Factors involved in the formation and development of severe weather conditions over the megacity of São Paulo

Freitas E. D., Rozoff C. M., Cotton W. R., Dias P. L. S., Interactions of an urban heat island and sea-breeze circulations during winter over the metropolitan area of São Paulo, Brazil, 2007, pp 43–65

Holden Z. A., Abatzoglou J. T., Luce C. H., Baggett L. S., Empirical downscaling of daily minimum air temperature at very fine resolutions in complex terrain, Agricultural and Forest Meteorology, 2011, vol. 151, p. 1066

Holden Z. A., Crimmins M. A., Cushman S. A., Littell J. S., Empirical modeling of spatial and temporal variation in warm season nocturnal air temperatures in two North Idaho mountain ranges, USA, Agricultural and Forest Meteorology, 2011, vol. 151, p. 261

Holden Z. A., Swanson A., Klene A. E., Abatzoglou J. T., Dobrowski S. Z., Cushman S. A., Squires J., Moisen G. G., Oyler J. W., Development of high-resolution (250 m) historical daily gridded air temperature data using reanalysis and distributed sensor networks for the US Northern Rocky Mountains, International Journal of Climatology, 2016, vol. 3632, p. 3620

Kaihatu J. M., Handler R. A., Marmorino G. O., Shay L. K., Empirical Orthogonal Function Analysis of Ocean Surface Currents Using Complex and Real-Vector Methods *, Journal of Atmospheric and Oceanic Technology, 1998, vol. 15, p. 927

Krogh S. A., Pomeroy J. W., Mcphee J., Physically Based Mountain Hydrological Modeling Using Reanalysis Data in Patagonia, Journal of Hydrometeorology, 2015, vol. 16, p. 172

LeMone M. a., Ikeda K., Grossman R. L., Rotach M. W., Horizontal Variability of 2-m Temperature at Night during CASES-97, Journal of the Atmospheric Sciences, 2003, vol. 60, p. 2431

Lookingbill T. R., Urban D. L., Spatial estimation of air temperature differences for landscape-scale studies in montane environments, Agricultural and Forest Meteorology, 2003, vol. 114, p. 141

Ludwig F. L., Horel J., Whiteman C. D., Using EOF Analysis to Identify Important Surface Wind Patterns in Mountain Valleys, Journal of Applied Meteorology, 2004, vol. 43, p. 969

Lundquist J. D., Cayan D. R., Surface temperature patterns in complex terrain: Daily variations and long-term change in the central Sierra Nevada, California, Journal of Geophysical Research, 2007, vol. 112, p. 112

Mahrt L., Variation of Surface Air Temperature in Complex Terrain, American Meteorological Society, 2006, vol. 45, p. 1481

Minder J. R., Mote P. W., Lundquist J. D., Surface temperature lapse rates over complex terrain: Lessons from the Cascade Mountains, Journal of Geophysical Research, 2010, vol. 115, p. D14122

Murphy J., An evaluation of statistical and dynamical techniques for downscaling local climate, Journal of Climate, 1999, vol. 12, p. 2256

Nobre C. A., Marengo J. A., Seluchi M. E., Cuartas L. A., Alves L. M., Some Characteristics and Impacts of the Drought and Water Crisis in Southeastern Brazil during 2014 and 2015, Journal of Water Resource and Protection, 2016, vol. 8, p. 252

Oliveira A. P., Bornstein R. D., Soares J., Annual and diurnal wind patterns in the city of são paulo, Water, Air, and Soil Pollution, 2002, vol. 3, p. 3

Oliveira A. P., Dias P. L. S., Aspectos observacionais da brisa maritima em Sao Paulo. In Ann. 2nd Brazilian Congr. Meteorol. , No. 2, 1978, p. 129

Oyler J. W., Ballantyne A., Jencso K., Sweet M., Running S. W., Creating a topoclimatic daily air temperature dataset for the conterminous United States using homogenized station data and remotely sensed land skin temperature, International Journal of Climatology, 2014, vol. 2279, p. n/a

Pepin N., Benham D., Taylor K., Modeling Lapse Rates in the Maritime Uplands of Northern England: Implications for Climate Change, Arctic, Antarctic, and Alpine Research, 1999, vol. 31, p. 151

Perez G. M. P., Dias M. A. F. S., Long-term study of the occurrence and time of passage of sea breeze in São Paulo, 1960-2009, International Journal of Climatology, 2017

Preisendorfer R., Mobley C., , 1988 Principal component analysis in meteorology and oceanography

Rigollier C., Bauer O., Wald L., On the clear sky model of the ESRA - European Solar Radiation Atlas with respect to the Heliosat method, Solar Energy, 2000, vol. 68, p. 33

Rolland C., Spatial and seasonal variations of air temperature lapse rates in alpine regions, Journal of Climate, 2003, vol. 16, p. 1032

Ross J., Relevo brasileiro: uma proposta de classificação., Revista do DG-USP, 1985, pp 25–39

Saad S., Modelagem e valoração dos serviços ambientais hidrológicos da recuperação da vegetação no Ribeirão das Posses, Extrema, MG. PhD Thesis, University of São Paulo, São Paulo., 2016, Thesis (doutorado em ciências ambientais)

Scharmer K., Page J., Wald L., Albuisson M., Czeplak G., Bourges B., Aguiar R., Lund H., Joukoff A., Terzenbach U., Beyer H. G., Borisenkov E., The European Solar Radiation Atlas Vol.2: Database and exploitation software, 2000

Silva Dias M. A. F. ., Machado A. J., The role of local circulations in summertime convective development and nocturnal fog in sao paulo, brazil, Boundary-Layer Meteorology, 1997, vol. 82, p. 135

Tang Z., Fang J., Temperature variation along the northern and southern slopes of Mt. Taibai, China, Agricultural and Forest Meteorology, 2006, vol. 139, p. 200

Thornton P. E., Running S. W., Withe M. A., Generating surfaces of daily meteorological variables over large regions of complex terrain, Journal of Hydrology, 1997, vol. 190, p. 214

Vemado F., Pereira A., Severe Weather Caused by Heat Island and Sea Breeze Effects in the Metropolitan Area of São Paulo, Brazil, Hindawi, 2016, p. 13

Von Storch H., Zwiers F., Statistical Analysis in Climate Cambridge University Press:, 1999

Whiteman D. C., Observations of thermally developed wind systems in mountainous terrain, AMS Meteorological Monographs, 1990, vol. 45, p. 5

Whiteman D. C., Mountain Meteorology: Fundamentals and Applications. Press, Oxford University, 2000, 355 p.

Wilks D., Statistical Methods in the Atmospheric Sciences. Academic Press: San Diego, 1995

Zardi D., Whiteman C. D., , 2013 in Springer ed., , Mountain Weather Research and
    Forecasting. Springer Atmospheric Sciences Chapt. 2 pp 35–119